Learning from Nature's Failures

Mimicking Hierarchy in Natural Structures to Create Damage-Tolerant Lattice Materials

Katharina Ertman

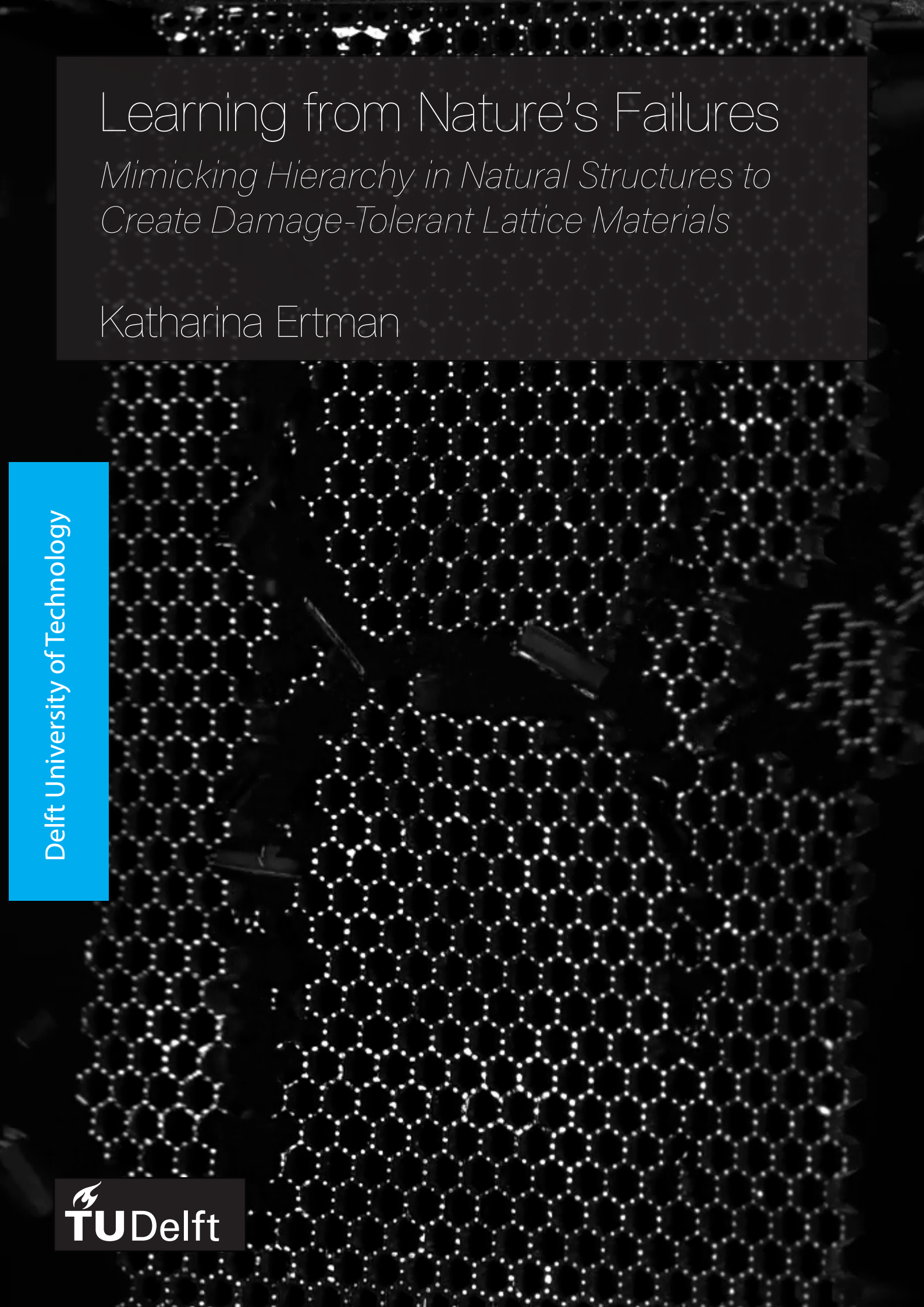

Delft University of Technology

TU Delft

Learning from Nature's Failures

Mimicking Hierarchy in Natural Structures to Create Damage-Tolerant Lattice Materials

by

Katharina Ertman

to obtain the degree of Master of Science
at the Delft University of Technology,
to be defended publicly on Friday July 10, 2020 at 1:00 PM.

Student number:	4590791	
Project duration:	2 September 2019 - 10 July 2020	
Thesis committee:	Dr. C.D. Rans	TU Delft, supervisor
	Dr. J.J.E. Teuwen	TU Delft
	Dr. O.K. Bergsma	TU Delft

TU Delft

Preface

When I started at TU Delft, little did I know what adventures lay ahead of me. If someone had told me that I would be graduating four years later. In a completely different track. With a thesis related to statics and mechanics of materials (far from my best subjects during undergrad) and had the term ”biological” in it somewhere. Having done a full-time board year in the Central Student Council working to make TU Delft a better place. And having met so many amazing, inspiring people along the way...

I would have thought you were completely nuts and had the wrong person. Looking back, I wouldn't have wanted it any other way. I absolutely couldn't have done it alone, and there are so many people I have to thank for helping me along the way.

First of all, thank you to Calvin Rans, my supervisor, for your guidance and trust throughout this thesis and for giving me the freedom to create something that I can call my own. And, of course, for helping me see the ASM light.

Thank you also to my daily supervisor, Megan Walker, for your enthusiasm and insight in navigating the uncharted territory that is the world of experimental lattice structures. It was immensely helpful and comforting to know that I could always come to you if I had a question, needed to talk some ideas through with someone, or just wanted to do a bit of show-and-tell after a day of testing.

None of the experimental work would have happened without the support of the DASML staff, but I have to especially thank Gertjan Mulder for sharing your knowledge and passion for additive manufacturing and graciously putting up with my many questions.

To Gillian and Michiel, thank you for your support and encouragement throughout these years, but also for taking me on for so many great and interesting projects. I might be graduating slightly later because of those, but I can wholeheartedly say it was worth it.

To all the TU Delft friends I've made along the way, from Lijst Bèta to the SI&C/AMT MSc room and everywhere in between, thank you for making this rollercoaster of an education an enjoyable one, filled with lots of laughter and fantastic food.

To my family, I can't even begin to express my gratitude for your constant love and support through every twist and turn over these last four years and for always encouraging me to pursue my passions. And finally, to Yitzi, thank you for your love, endless patience, and the perfect amount of silliness to keep me afloat.

Katharina Ertman
Delft, July 2020

Abstract

To create a more sustainable future for aviation, new, lighter-weight structures and materials will need to be engineered. It will also be critical that damage tolerance and safety are not compromised in the process. Lattice materials represents one avenue of exploration; however, two key challenges arise: limited experimental work has been conducted to date regarding tensile mechanical response and lattice materials are generally considered to be less tough than traditional aerospace materials. Advancements in additive manufacturing in recent years creates the opportunity to rapidly produce high-quality complex geometries, allowing for both challenges to be more easily investigated. To address the issue of toughness and damage tolerance, nature is a source of inspiration, as all of nature's toughest materials derive this characteristic from creating structural hierarchy using intrinsically weak building blocks.

Two sets of lattice structures were fabricated using stereolithographic (SLA) 3D printing and tested under quasi-static tensile loading. Two sets of lattices were fabricated: lattices with uniform strut thickness, or relative density, and mixed-relative density lattices which create structural hierarchy. Using a novel method to track lattice deformation during loading, lattice stiffness-displacement response has been correlated with beam elongation and rotation behavior and the deformation of individual cells. The stiffness-displacement response of uniform lattices can be classified by relative density as either an *elastomeric*, *elastoplastic*, or *hybrid* response. In hierarchical lattices, cell deformations occurring in different relative density regions are directly correlated to features of the stiffness-displacement response.

Aspects of the mechanical response of hierarchical lattices, particularly fracture toughness and fracture pattern, are heavily influenced by the exact configuration of structural hierarchy, spurring a discussion of what characteristics are most important in the pursuit of increased lattice damage tolerance. While none of the lattices represent an optimal solution, each displayed characteristics which, if combined to form a hybrid structure, could substantially improve lattice damage tolerance.

Contents

List of Tables

List of Figures

Nomenclature

Abbreviations

DASML	Delft Aerospace Structures and Materials Laboratory
DIC	Digital image correlation
FE(A)	Finite-element (analysis)
LEFM	Linear-elastic fracture mechanics
MSDS	Material safety data sheet
SLA	Stereolithography apparatus

Greek Symbols

$\bar{\rho}$	Relative density	
ρ	Base material density	kg/m^3
ρ^*	Unit cell density	kg/m^3
σ_{fs}	Base material fracture strength	MPa
θ	Beam deformation angle	°
θ'	Initial beam angle	°
ε_{break}	Elongation at failure	

Latin Symbols

$\bar{E}$	Lattice elastic modulus	MPa
$\bar{K}_{IC}$	Lattice Mode I fracture toughness	MPa$\sqrt{m}$
ΔL	Beam elongation	m
a	Crack length	m
E_s	Base material elastic modulus	MPa
E_{bend}	Flexural modulus	MPa
I	Second moment of inertia	m^4
K_{IC}	Mode I fracture toughness	MPa$\sqrt{m}$
L	Deformed lattice height	m
l	Unit cell length	m
L_0	Initial lattice height	m
$M(x)$	Internal beam moment function at location x	N•m
t	Unit cell thickness	m
$V(x)$	Internal beam shear force function at location x	N
$w(x)$	Beam deflection function at location x	m

1

Introduction

The future of aviation is lightweight; less raw material needed for manufacturing, lower CO2e emissions over the service life of an aircraft. This future will necessitate pushing the boundaries of what structures and materials are used, but this must be done without compromising safety. Most of the aircraft flying above us today have been largely designed to be built from aluminum and titanium. While these materials are very strong, they are monomaterials, and there is generally a limit to the amount of material that can be removed before they no longer retain their damage tolerance to the standards that have been developed in recent decades.

Enter natural structures. Virtually all materials in nature are multi-material structures built from two basic building blocks: brittle minerals and elastic proteins. Individually, neither are very strong or tough, but through millions of years of evolution, nature has cleverly arranged these materials using several layers of structural hierarchy to create some of the world's toughest materials, like cortical bone and mother-of-pearl. Cracks that nucleate in a natural material must navigate a maze of obstructions or follow a path-of-least-resistance which is not parallel to the loading force, both of which aim to reduce crack driving force and slow damage growth. It would not be remotely practical, however, to construct an entire aircraft from mother-of-pearl, but the principles can still be applied to engineering design in the search for new damage-tolerant structures.

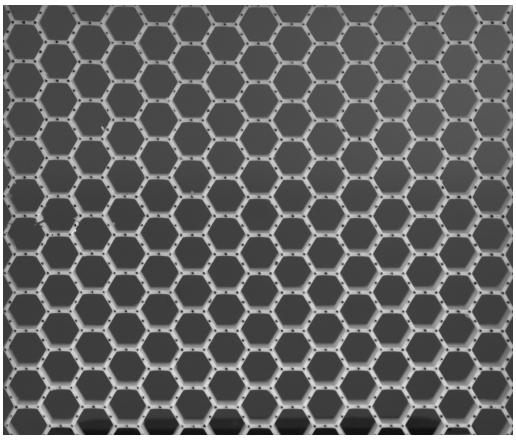

Figure 1.1: *Example of a hexagonal honeycomb structure*

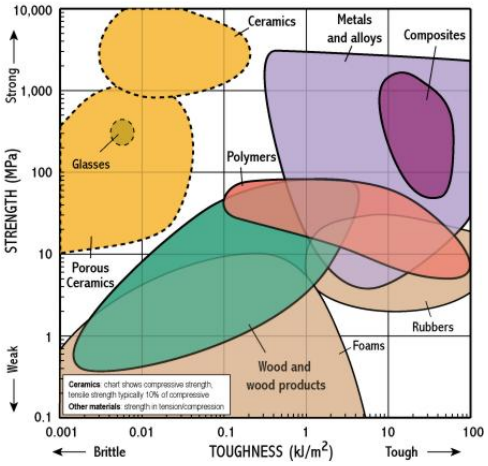

Figure 1.2: *Ashby diagram of strength-toughness ranges for various material families [2]*

One possible avenue for implementing structural hierarchy in engineering design is through the use of cellular materials. Cellular materials, also called honeycombs or lattice structures, typically are idealized natural structures, defined by their regular, periodic structure comprised of unit cells, shown in Figure 1.1. They are, however, generally regarded as weaker than their metallic and ceramic counterparts, as shown in Figure 1.2. It is not outside the realm of possibility that cellular structures, when tuned to a specific application, could be a way to further lighten structures without compromising on strength, stiffness, or toughness. Recent advancements in additive manufacturing have made it possible to rapidly create high-quality, homogeneous lattices, making it possible to investigate and validate numerical models in hopes of gaining more understanding of the experimental behavior of lattice structures. It also creates the opportunity to explore whether structural hierarchy can be incorporated into

these structures and study the impact on damage tolerance. The hierarchical structures of nature provide an excellent starting point. Nature has already done the research into tough, lightweight structures, so why spend time reinventing the wheel?

This thesis explores how adding structural hierarchy affects various aspects of the mechanical response of hexagonal-celled lattice structures, including fracture toughness, stiffness behavior, and fracture and cell deformation patterns. Specimens are additively manufactured using stereolithography and experimentally tested under quasi-static tensile conditions. Drawing inspiration from nature, several configurations of structural hierarchy are adapted from various biological materials. Each configuration is chosen with the intent of highlighting different strategies used in nature to create damage tolerance. A set of non-hierarchical lattices, the uniform lattices, is also investigated to provide a basis for comparison and gain a fundamental understanding of experimental lattice tensile behavior.

At a high level, this thesis is divided into three parts. Part I begins with additional background information on damage tolerance and cellular materials, which aim to provide context for this work, and concludes with the research project definition. Part II further expands on the research definition, detailing the experimental methodology and discussing some limitations and uncertainties in the methods, followed by presentation of the experimental results. Finally, Part III synthesizes results and observations, for both the uniform and hierarchical lattices separately, and engages in a discussion on their implications, what can be concluded from them, and highlights a few opportunities for further work.

I

Background and Research Definition

2

Damage Tolerance and Toughness

No structure is built to last forever, but some are more resilient than others. The more a structure is able to cope with damage without experiencing significant loss of strength or catastrophic failure, the more *tough* and *damage-tolerant* it is considered to be. There is, however, no one-size-fits-all approach, and damage tolerance can take many different forms depending on the boundary conditions of the design problem. In the engineering domain, damage tolerance is seen as an inherent characteristic of the materials used, and understanding how damage progresses has become critical to maintaining safety. Nature, on the other hand, has taken inherently weak building blocks and used structural hierarchy to create materials which are purpose-built to survive in the surrounding environment. Both approaches, though vastly different, ultimately achieve their damage-tolerant goals.

2.1. In aerospace design

In just over 100 years, aviation has seen three major developments in structural design philosophy. At first, aircraft were designed on the safe-life principle; structures were not expected to fail within their intended service life. Prolific accidents such as those involving the De Havilland Comet, however, led to the development of fail-safe design. In fail-safe design, multiple elements create redundancy and ensure there is not a single point of failure. In the 1970s, damage tolerance emerged as a companion to safe-life and fail-safe. Damage tolerant design requires that structures be able to withstand expected loads in the presence of damage until an inspection and repair can be completed [14, 15].

In aerospace design, damage tolerance begins with tough, durable materials. Materials must be able to resist crack initiation for as long as possible, but failure is inevitable. At this point, it is critical that materials have a high fracture toughness and are able to resist rapid, unstable crack propagation. But toughness does not emerge from a single point of origin, rather it is the sum of the interaction of multiple properties and characteristics. Our understanding of toughness in commonly-used aerospace materials has been refined through decades of research, maintenance, and accident investigation. The aircraft of the future will require new materials which could have vastly different properties and characteristics, but they will still need to demonstrate toughness and damage tolerance. It is, therefore, critical to understand the underlying mechanisms that impart toughness.

Fracture toughness emerges as the result of several mechanisms working together to resist further crack growth. These mechanisms, aptly called *toughening mechanisms*, can be observed in various forms. Figure 2.1 give schematic representations of a few commonly-observed mechanisms, which are described below.

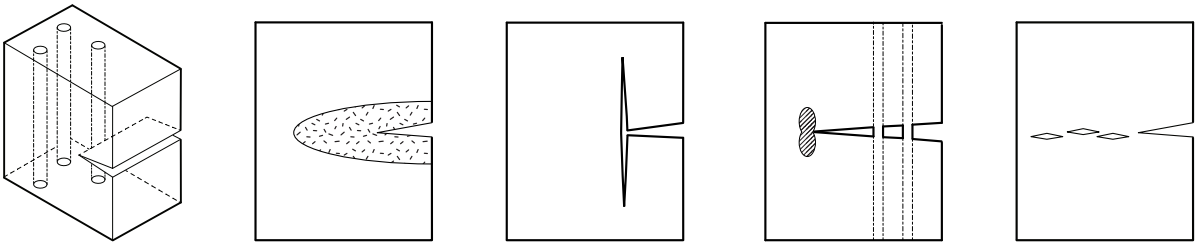

(a) *Crack deflection* **(b)** *Constrained microcracking* **(c)** *Crack branching* **(d)** *Ligament bridging (behind the crack tip)* **(e)** *Ligament bridging (ahead of the crack tip)*

Figure 2.1: *Schematic representations of common toughening mechanisms*

Crack deflection
Cracks ideally want to follow the path of least resistance, but sometimes this is not possible. Inclusions, for instance, can create an impassable obstacle, forcing cracks to divert away from the load plane and requiring higher loads to continue propagation. Crack deflection can also occur due to voids in the microstructure which provide multiple potential ”paths of least resistance” [16, 17].

Constrained microcracking
Microcracking occurs when several small cracks form in the area surrounding the crack tip, often by sacrificial elements, as a way to dissipate fracture energy in the structure and increase material plasticity. It can also help promote crack deflection by providing several ”paths of least resistance” [16, 17].

Crack branching
In brittle materials, a crack may split off in two different directions simultaneously. This can be the result of fast fracture, but can also occur in slow-moving cracks, particularly in materials with complex stress fields. In either case, the goal is to dissipate fracture energy as quickly as possible using multiple channels [18].

Ligament bridging
The exact nature of ligament bridging is often a matter of perspective. It can be seen as a mechanism acting behind a crack tip, where some material remains intact which prevent the fracture planes from further separation, reducing stresses at the crack tip. It can also be viewed as similar to constrained microcracking, where material ahead of the crack fractures to relieve stresses at the crack tip, but the fractures are much larger and extend further into the material than microcracking. For the purposes of this document, the term *ligament bridging* will be used to describe both conditions [16, 17].

2.2. In natural structures

While damage-tolerant design is a relatively new philosophy in aviation, nature has been using it for millions of years to create tough, damage-tolerant structures. Virtually all natural structures are engineered from two base components: brittle minerals, which are weak in tension, and elastic proteins, which collapse immediately under compression loads. Therefore, damage tolerance in nature is not derived from the base materials, but how they are assembled at various levels of structural hierarchy.

The mechanisms that drive damage tolerance and toughness in these materials can be a source of inspiration on improving these characteristics in artificial structures and materials. This section explores some of these materials and the underlying structures which give rise to their tough properties.

Abalone nacre
Nacre, or mother-of-pearl, is one of nature’s toughest materials, owing to a dense brick-and-mortar patchwork of brittle aragonite $CaCO_3$ tablets and compliant biopolymers, shown in Figure 2.2. Under tension loading, the biopolymer interface initially prevents the aragonite tablets from easily sliding past each other. As loading continues and no existing crack is present, small voids begin to form in the tablet layers, dissipating stresses across the entire structure. If there is an existing crack, these voids still form and the crack does progress, but its path becomes tortuous because cracks are guided along the weak biopolymer interfaces, reducing crack driving force and blunting the crack tip [16, 19–21].

Bamboo
Bamboo is one of the most efficient natural materials in terms of mechanical performance per unit weight, having 2-4 times the structural efficiency of a solid beam of the same bending stiffness [17]. This characteristic stems from functional grading in the load-bearing fibers of the stalk, shown in Figure 2.3. The fibers are distributed such that fiber density increases towards the outer edge of the stalk, resulting in a modulus gradient from the inner to outer edges of the stalk. This grading also impacts fracture behavior. Cracks that form in the low-density region are deflected, reducing crack driving force. As a crack reaches the high-density region, the force

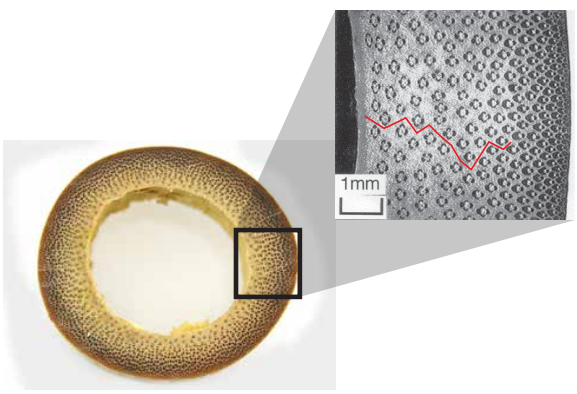

Figure 2.3: *Cross-section of a bamboo stem*
Inset: Microscopic image of section of bamboo stem with a theoretical crack path overlaid. Adapted from [3, 4]

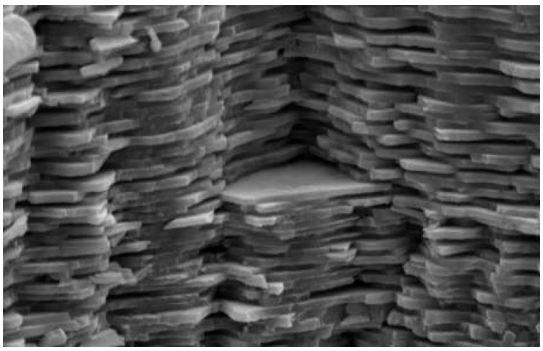

(a) *SEM image showing the brick-and-mortar microstructure of nacre [22]*

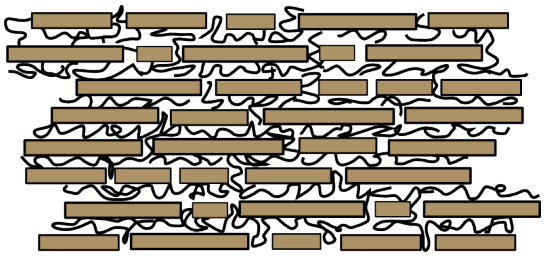

(b) *Schematic representations of the aragonite tablets (brown) and biopolymer (black) that form the microstructure of nacre [23]*

Figure 2.2: *Nacre microstructure, in nature and idealized*

required to continue propagation increases, slowing growth or arresting it entirely [17].

Glass sponge

Where bamboo uses stiff inclusions to divert crack growth, the opposite can be found in glass sponges, such as *Monorhapis chuni* and *Euplectella aspergillum*. Their structure is primarily composed of concentric layers of brittle bioglass separated by soft silicatein layers, shown in Figure 2.4 [6, 21], which work together to resist catastrophic failure.

Cracks that form in the brittle bioglass phase are likely to occur suddenly, but are slowed or stopped by the compliant silicatein layer due to a reduction in crack driving force, also shown in Figure 2.4 [6]. As Kolednik et al. point out, this is a fundamentally different toughening mechanism than that of bamboo or nacre, since it does not force a crack to turn and continue (crack deviation), nor does it rely on some material remaining behind the crack tip to carry additional loads (ligament bridging) [6]. It can seem a bit counterintuitive; toughness is increased by introducing a weaker material into the structure; this structure allows deformation to occur and let the structure adapt to loading, but also ensures that cracks cannot gain enough energy to catastrophically propagate.

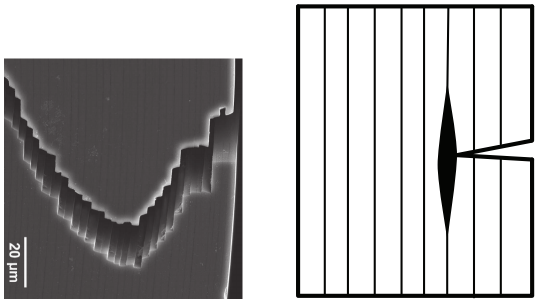

Figure 2.4: *Fracture in an actual (left [5]) and idealized (right, adapted from [6]) M. Chuni glass sponge microstructure*

3

Cellular Materials

Cellular materials [1] have been put to use for thousands of years, but more recently, they have become a source of inspiration for novel structures. Honeycombs first appeared in the aerospace industry in the 1910s. Soon after, research into their mechanical response in various loading modes exploded [24]. The focus, however, was mainly on their out-of-plane properties under compression loads.

The in-plane mechanical behavior of hexagonal honeycomb structures was first extensively studied analytically by Gibson and Ashby [25]. Their work forms our fundamental understanding of these structures and is the basis for further research in the field. Subsequent research, however has been limited to the study of uniform honeycombs using numerical methods that assume linear-elastic behavior, but developments in advanced manufacturing techniques have recently made experimental testing possible, opening up the field to expand beyond uniform structures.

Lattice behavior can be investigated on two levels, which for this thesis will be defined here as either *lattice-level* or *cell-level*. The term *lattice-level* encompasses the information that could be obtained if no images could be recorded during experimental testing; only data collected by the load cell would be available. Without visual information, only the bulk lattice response can be assessed in terms of a homogeneous solid with equivalent mechanical properties. The *cell-level* response, by contrast, is comprised of all the information that could be obtained by knowing what the structure looks like, without knowing information about the applied loads or force-displacement behavior.

3.1. Fundamentals

Lattices are idealized representations of natural structures and can be divided into two groups: honeycombs, two-dimensional structures, and foams, three-dimensional structures, and could be thought of as a composite material made of a base material and the surrounding air. The foundation of a lattice structure is the unit cell. Unit cell properties determine not only individual cell deformation behavior (i.e. cell-level), but also influence the mechanical response of the full lattice (i.e. lattice-level). Three parameters have been identified which play an outsized role in lattice mechanical response, namely base material properties, cell topology, and relative density [7].

3.1.1. Base material properties

The general stress-strain response of a lattice's base material determines lattice stress-strain response. In other words, a lattice made from a brittle material will have a brittle response [7]. This is schematically illustrated in Figure 3.1 for elastomeric, plastic, and brittle lattices under tension loading.

At the cell-level, base material properties also seem to influence how individual cells deform and adapt to increasing loads. Gibson and Ashby identified two main types of cell deformation for honeycombs in tension: cell wall bending and plastic collapse. A third deformation shape was described for brittle fracture, but not explicitly named [7].

Cell wall bending

Initial cell deformation behavior in linear-elastic lattices is described as "cell wall bending", shown in Figure 3.2, and is the result of linear-elastic deformation [26–28] as bending moments are introduced into the strut. Inclined struts also carry axial and shear loads, but these are considered negligible for low relative densities [7]. Bending continues up to failure, when the bending moment in the strut exceeds the fracture strength of the material.

[1] There are a number of terms which can be used interchangeably to describe cellular structures, including cellular structure/material/solid, lattice structure/material, metamaterial, and (hexagonal) honeycomb. In the context of this work, any of these terms refer to a two-dimensional hexagonal lattice comprised of a periodic pattern of nodes and the ligaments that connect them, as shown in Figure 1.1

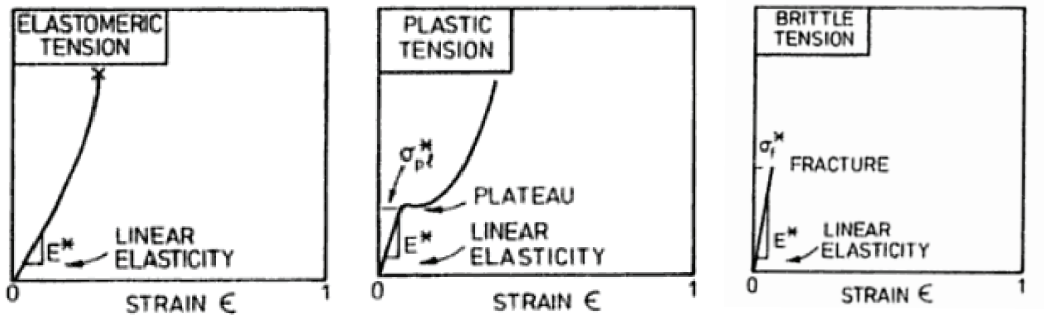

Figure 3.1: *Stress-strain responses of a lattice under tension loading per base material type [7].*

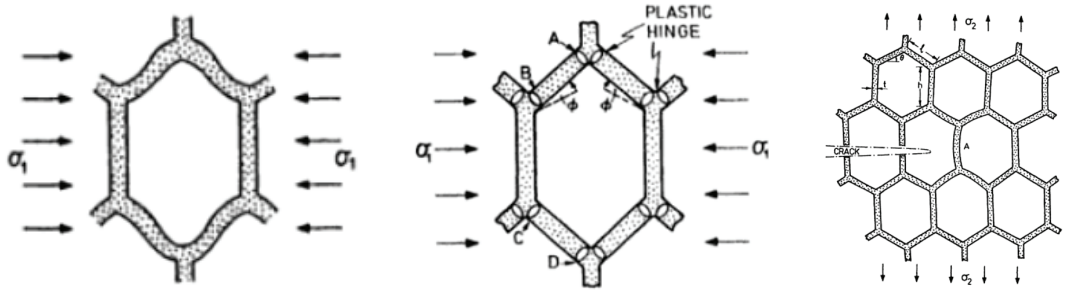

Figure 3.2: *Types of cell wall deformations described by Gibson and Ashby [7].*
From L to R: Cell wall bending, plastic collapse, brittle fracture

Plastic collapse
If a lattice is made of an elastic-plastic material, initial deformation occurs by cell wall bending; however, when the bending moment reaches the fully plastic moment, struts begin to hinge at the node instead of fracturing [7]. Struts rotate about the node up to the failure point and no longer bend.

Brittle bending
For a brittle lattice under tensile loading, little deformation is expected in the cell walls prior to fracture. Though not explicitly addressed by Gibson and Ashby, it was predicted that some amount of deformation occurs in the cell walls immediately ahead of a crack, illustrated on the righthand side of Figure 3.2. This deformation is most pronounced in the cell wall just ahead of the crack, which deflects in one direction only, as opposed to the s-shape present in cell wall bending [7].

3.1.2. Cell topology

The geometric properties of the unit cell, i.e. size, shape, and relative density, collectively define cell topology.

Cell shape dictates how nodes and struts interact under loading. Cell shapes can be broadly classified as either *stretch-dominated* or *bending-dominated*, shown schematically in Figure 3.3. In a stretch-dominated lattice, such as the triangular lattice, failure is defined by the axial strength of the struts. In a bending-dominated lattice, such as the hexagonal lattice, failure occurs when stresses due to bending moments exceed the material strength. This has implications for fracture toughness and crack propagation; bending-dominated structures have a lower fracture toughness and allow faster propagation

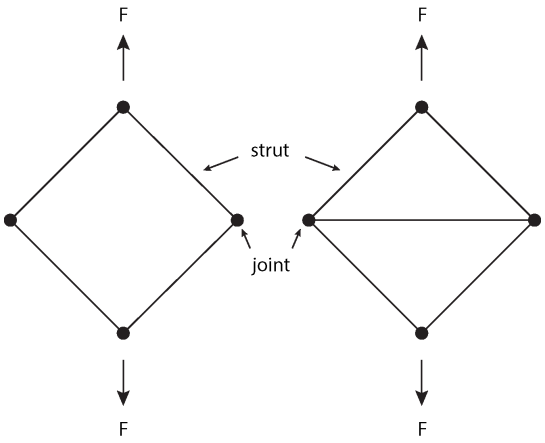

Figure 3.3: *Schematic representation of a bending-dominated lattice (left) and a stretch-dominated lattice (right). Adapted from [8]*

compared to stretch-dominated structures [8].

Cell size, as the name suggests, is the size of a unit cell and dictates the number of cells in a lattice with a given set of dimensions. There is, however, no standard method to calculate cell size. Huang and Gibson and Huang and Chiang defined cell size by strut length, l, exclusively [29, 30]. This definition is confusing, however, as l is linked with cell shape; a hexagonal unit cell of size 0.5mm does not have the same area as, and cannot be compared to, for instance, a square unit cell of size 0.5mm.

Relative density describes the ”stockiness” of struts in a lattice and quantifies the geometric relationship between a lattice and solid, homogeneous material. Relative density can be defined as the ratio of the density of the cellular structure and the density of the base material, as well as by geometric parameters:

$$\bar{\rho} \propto \frac{\rho^*}{\rho} = \frac{t}{l} \tag{3.1}$$

3.2. Lattice-level mechanical response

Lattice-level mechanical response is defined by the complex interactions of individual cells deforming under an applied load. When modelled using analytical and numerical methods, such as the continuum model or boundary layer analysis, lattice properties, such as relative elastic modulus and relative fracture toughness, and behaviors, such as crack propagation patterns and crack tip displacement, can be predicted.

3.2.1. Two modelling approaches

The first model used to assess the mechanical response of lattice structures was the continuum model, developed by Gibson and Ashby [7]. An extension of this model was later proposed by Schmidt and Fleck to address some of the deficiencies of the continuum model [9].

The continuum model, as the name suggests, compares lattices to an equivalent continuum; the average forces and moments acting on a single unit cell are calculated using LEFM principles and then extrapolated to estimate the behavior of the full lattice [7]. This results in expressions for lattice properties, such as relative elastic modulus and fracture toughness. A criticism of using the continuum model for FE lattice analysis was raised by Quintana-Alonso and Fleck, who noted that the model is typically used to predict strength, not fracture toughness, which potentially limits its usefulness [31]. Another disadvantage is that lattices can only be evaluated up to the onset of fracture, since the unit cell is no longer representative of the entire lattice and stress redistributions cannot be calculated.

Boundary layer analysis is a hybrid approach which builds on the continuum model, where the plastic zone of an equivalent elastic continuum is assumed and superimposed onto a lattice model composed of beam elements. This allows a full lattice to be modelled at a relatively low computational cost and lattice behavior to continue to be modelled after the onset of fracture, providing insight into lattice damage progression. This expansion also furthered understanding of the stress fields which develop at an existing crack in a lattice.

Three key assumptions were made in the development of the continuum model. And because boundary layer analysis uses a continuum approach in part, these assumptions also apply to boundary layer analysis.

1. Analyses are valid for $\bar{\rho} < 0.20$
   Gibson and Ashby identified $\bar{\rho} < 0.20$ as the theoretical limit for which axial and shear forces in the struts can be neglected. Therefore, the metamaterial models are generally considered valid for these relative densities [7]. This was corroborated by Huang and Gibson, finding that axial stresses likely cannot be neglected above $\bar{\rho} = 0.20$ [29].

2. Crack length is large relative to cell size ($a/l > 7$)
   In conducting experimental studies, Huang and Gibson concluded that it is unrealistic to assume that cracks will always be large relative to cell size, given that small cracks of 3-4 cells commonly occur in brittle lattices [29]. The presence of small cracks likely increase in experimental lattices to due discrepancies between the ideal and ”as-manufactured” lattice [32].

3. All cell walls have a constant modulus of rupture
   Several researchers noted that since brittle fracture is a stochastic process, the modulus of rupture

is not constant and is influenced by flaw size and frequency [30, 33], and manufacturing quality affects lattice consistency and similarity to numerically-modelled lattices [32, 34].

3.2.2. Lattice properties

Generalized expressions were derived analytically by Gibson and Ashby to describe the relative modulus and fracture toughness of lattice materials [7], called scaling laws, given in Equations 3.2 and 3.3. These expressions are used in both metamaterial models, and any differences between the two metamaterial models are evident in the values of coefficients B, b, D, and d; Table 3.1 provides some values obtained by various researchers for context. Both, however, demonstrate the importance of relative density in lattice tensile response.

$$\frac{\bar{E}}{E_s} = B\bar{\rho}^b \tag{3.2}$$

$$\frac{\bar{K}_{IC}}{\sigma_{ts}\sqrt{l}} = D\bar{\rho}^d \tag{3.3}$$

Table 3.1: *Sample values for scaling law coefficients obtained in literature*

Author(s)	Metamaterial model used	B	b	D	d
Gibson and Ashby [7]	Continuum	2.3	3	0.53	2
Huang and Chiang [30]	Continuum FE	-	-	0.43	2
Fleck and Qiu [35]	Boundary layer analysis	-	-	1.20	2
Tankasala et al. [11]	Boundary layer analysis	1.5	3	0.76	2

Using the continuum model, however, to determine $\bar{K}_{IC}$ has been called into question [31]. In solid materials, K_{IC} should not have any geometric dependencies. In lattice materials, however, geometric and test condition dependencies have been observed by Huang and Chiang, who found that K_{IC} values obtained in three-point bending tests were higher than those obtained in uniaxial tensile tests for lattices of the same dimensions [30]. Despite this uncertainty, subsequent research continues to use the scaling laws and as a means of comparing results in terms of the obtained coefficient values.

3.2.3. Crack propagation

Fracture in lattice structures occurs when the bending moment in a cell wall exceeds the lattice's modulus of rupture. The continuum model predicts that this occurs in the cell wall immediately ahead of the crack tip in brittle lattices, shown in Figure 3.2, while Schmidt and Fleck found that, for elastic-plastic lattices, the highest bending moment occurring in the strut one cell above or below the crack tip, illustrated in Figure 3.4 [7, 9]. Both models are unanimous in their assessment that once fracture has occurred in one strut, the rest of the lattice fails quickly. Cracks tend to propagate either above or below the crack tip with equal likelihood. The fracture of one strut causes stresses to be rapidly redistributed, overloading the surrounding structure which is already nearing its fracture strength. Once fracture has begun, cracks tend to "jump" across cell boundaries strut-by-strut, resulting in ligament bridges behind the crack tip which help relieve stresses ahead [9].

For solid materials, K_{IC} describes the onset of unstable fracture, but Schmidt and Fleck's findings on the strut-by-strut fracture pattern are more in line with an observation made by Mayer on natural ceramic composites. Mayer notes that natural ceramic composite materials have the unique ability to continue carrying load even after the peak load is reached, dissipating load in small steps rather than as

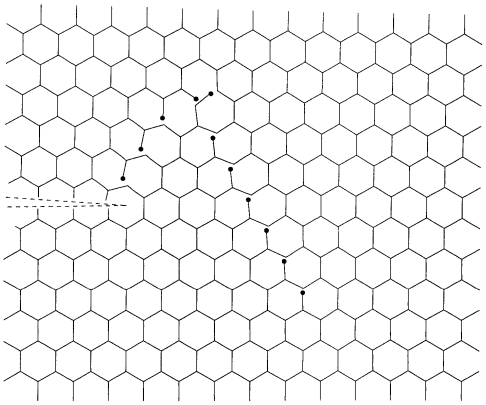

Figure 3.4: *Fracture path for elastic-plastic lattices as predicted by Schmidt and Fleck [9]*

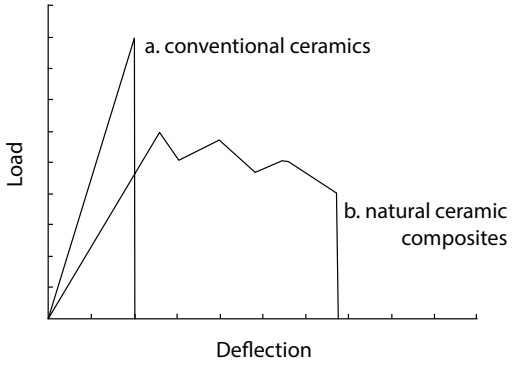

Figure 3.5: *Example load-deflection curves for a conventional ceramic material and a natural ceramic composite material [10]*

a single, instantaneous fracture, shown in Figure 3.5, behavior which is distinctly different from the traditional definition of fracture toughness [10]. In the pursuit of tougher cellular materials, $\bar{K}_{IC}$ is typically held up as the end-all, be-all variable to maximize, meaning that stretch-dominated lattices, which have an inherently higher $\bar{K}_{IC}$, receive more attention in literature compared to "weaker" bending-dominated hexagonal lattices of the same relative density, despite these concerns.

Recalling the assumptions made in the continuum model is that the modulus of rupture, and, therefore, the probability of fracture, is constant throughout a lattice. Investigations conducted by Cherkaev and Ryvkin refute this assumption, finding that struts accumulate damage at varying rates as loads are applied to a lattice, even if they do not fail [36]. They concluded that cumulative damage should not be ignored when considering how lattice structures fracture, and that it is erroneous to assume that all beams maintain their full strength at the time of fracture.

Experimental research into fracture patterns in lattice structures has been limited. Wu and Yang conducted experiments with SLA-printed lattices composed of 10-15 cells, looking specifically at the sequence of strut failure [34]. The limited number of cells, however, casts doubt on whether results would accurately describe failure in larger lattices and whether the cells' relative proximity to the clamps affected how loads were introduced into the structure and whether this impacted damage progression. Seiler et al. conducted similar experiments with lattices made from laser-cut PMMA, also looking at the sequence of strut failure and comparing this to a numerical simulation. To the author's knowledge, however, research has not be conducted on the effects of relative density on the fracture patterns of hexagonal-celled lattice structures.

3.2.4. Crack tip plastic zone

In solid materials, the crack tip plastic zone describes the region of plastic deformation immediately ahead of the crack tip. Utilizing boundary layer analysis, Schmidt and Fleck first predicted the shape and size of the plastic zone for elastic-plastic lattices. When considering plastic strains above $0.5\varepsilon_y$, the plastic zone takes on a double-lobed butterfly shape [9]. Expanding on this work, Tankasala et al. found the same double-butterfly profile, shown in Figure 3.6, and also determined the effect of material plasticity on the size of the crack tip plastic zone [11].

This finding has currently only been explored in FE analyses. Literature limits the discussion in terms of plasticity, so a possible deterrent to experimental work could be a lack of suitable methods for assessing whether plastic deformation is occurring in a lattice

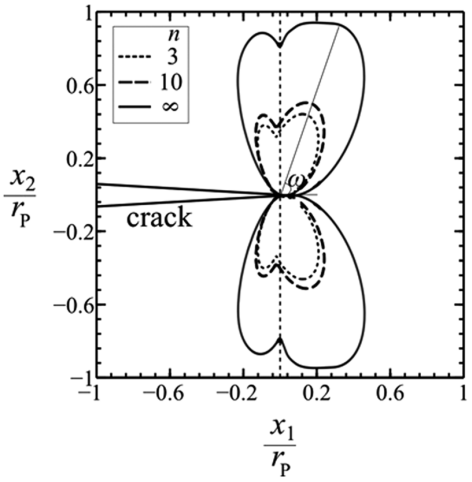

Figure 3.6: *Perimeter of the plastic zone for a hexagonal honeycomb of varying plasticity [11]*

structure which may not reach a yield point uniformly. And while cell wall plasticity is the criteria used in literature, any plastic deformation that occurs in the lattice will be linked with individual cell deformations; the crack tip plastic zone is simply a manifestation of those deformations. Therefore, it is not unreasonable to think that this double-lobed butterfly shape is not exclusive to lattices experiencing plastic deformation, but lattice deformation behaviors have not been experimentally investigated to date.

3.3. Beyond uniform relative density lattices

The field of cellular mechanics is relatively new, even more so for cellular structures in tension. Consequently, research has primarily focused on uniform relative density lattices, but recently there has been a growing interest in expanding beyond the uniform lattice. One promising concept is to introduce structural hierarchy into lattice structures, which has taken a few different forms.

One approach is to look the compliant and brittle material phases present in natural hierarchical structures. Libonati et al. and Dimas et al. conducted experimental research with 3D-printed composite lattices inspired by the structure of cortical bone and nacre, respectively. Both studies found that the predominant material phase and unit cell shape and orientation influence lattice mechanical response, including toughening mechanisms and final fracture path [37, 38]. A drawback of this approach is the use of two distinct materials to create the lattice, leaving concerns about the integrity of the interface between phases. Manufacturing these structures from a single material would eliminate this issue.

One method for creating hierarchy without using multiple materials is to locally vary relative density to create ”superstructures” within a lattice. Considering that relative density is the common thread in nearly all aspects of lattice mechanical response, it is not a stretch to think that lattice mechanical response can be tuned in this way. Lipperman et al. also explored this concept, developing an algorithm which optimized for lattice fracture toughness by redistributing mass within four unit cells which resulted in an 18% increase in $\bar{K}_{IC}$. There are a few limitations with this approach, however [39]. Lattice fracture toughness was the only optimized variable; other parameters, such as fracture pattern or stress (re)distribution, were not considered, This casts doubt on the ”optimal” nature of the solution. Without experimental validation, the reliance on $\bar{K}_{IC}$ as the ideal variable to optimize is also called into question.

The idea of creating varying relative density in a lattice structure to improve damage tolerance is a particularly fascinating one and leads to a flurry of questions. What is the effect of $\bar{\rho}$ variations on, for instance, fracture path or $\bar{K}_{IC}$? Is $\bar{K}_{IC}$ even the best parameter to consider here? Do different regions of $\bar{\rho}$ deform independently or work together to create some kind of hybrid response? Does the exact implementation of $\bar{\rho}$ variations matter? These questions are worth exploring to gain a better understanding of how lattice structures could be tuned for damage tolerance in the future.

4

Research Definition

4.1. Research question, objectives, and scope

Following a review of current literature, gaps in knowledge, questions, and missed opportunities still remain. A significant gap is the serious deficit of experimental work in the field of cellular structures. Much of this is due to the lack of high-quality, inexpensive manufacturing techniques up until very recently; however, this is changing with advancements in additive manufacturing. Continued experimental work would shed light on the accuracy of metamaterial models which form our understanding of cellular structures. Questions emerge concerning the influence of relative density on several aspects of lattice tensile response, such as fracture patterns and deformation during loading, as well as on how lattice behavior would change in lattices with a non-uniform relative density. Regarding the latter, the tough natural structures discussed in Chapter 2 provide a starting point for exploring the effects of additional structural hierarchy. With this in mind, the following question is proposed to guide the research:

How does mechanical response relate to toughening mechanisms that result from structural hierarchy in cellular materials?

The research objective is twofold: first, to investigate whether variations in relative density affect the mechanical response of 3D-printed honeycomb lattice structures, and in doing so, establish the feasibility of using relative density to create structural hierarchy. Second, to explore how mechanical response is affected when adding structural hierarchy to a lattice by only varying relative density. An experimental methodology will be used to assess lattice behavior at the lattice level and cell level.

The field of cellular structures is relatively uncharted, even more so for experimental study. Therefore, the research scope is narrowed to the experimental investigation of the tensile mechanical response of 2D hexagonal lattice structures made from a 3D-printed photopolymer, taking relative density to be the only varied parameter. Two sets of lattices will be used to assess the impact of relative density. Lattices in the first set will have a uniform relative density that varies between lattices, and a second set will use relative density to create different structural hierarchies. Four unique topologies were selected for the hierarchical lattices using two relative densities, shown schematically in Figure 4.1 and described in further detail in Chapter 5. The topologies have been chosen to explore just a few of the millions of possible implementations of structural hierarchy. As such, this thesis intends neither to be an exhaustive study, nor present an optimized solution. The intent, rather, is to spark further research into the intersection of lattice materials and structural hierarchy.

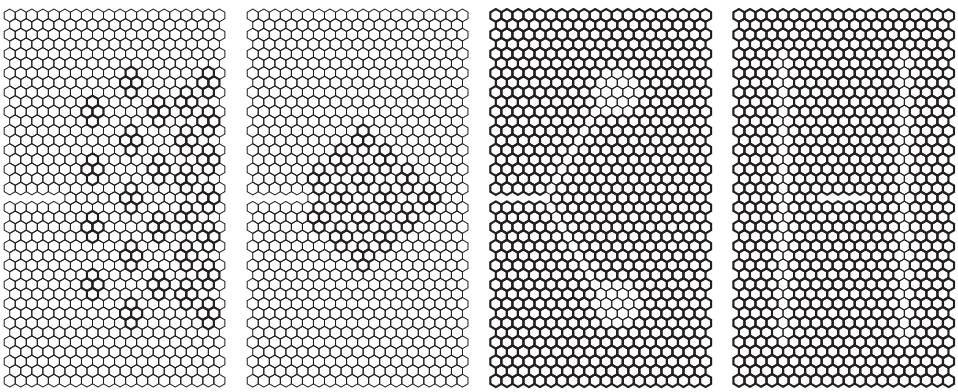

Figure 4.1: *Schematic representations of the four selected hierarchical topologies*

4.2. Hypotheses

Following from the proposed research question, two sets of hypotheses have been formed. The first set focuses on the relationship between relative density and mechanical response of uniform lattice structures, and the second set examines how mechanical response varies when structural hierarchy is introduced into a lattice.

Hypotheses on the influence of relative density and mechanical response of uniform lattices

1.1 Up to $\bar{\rho} = 0.2$, numerical models predicting lattice stiffness and lattice fracture toughness accurately describe mechanical response

1.2 Up to $\bar{\rho} = 0.2$, lattices exhibit the characteristic double-lobed butterfly crack tip deformation field shape described by Schmidt and Fleck

1.3 Beyond lattice stiffness and lattice fracture toughness, mechanical response is not affected by relative density; a lattice made from a brittle base material will exhibit brittle tensile behavior at all relative densities

1.4 Relative density does not affect fracture path or observed toughening mechanisms; predominant toughening mechanisms are crack deflection and ligament bridging

Hypotheses on the influence of structural hierarchy on lattice mechanical response

2.1 The predominant material phase (stiff or compliant) drives overall differences between hierarchical and uniform lattices; differences between lattices of the same predominant material phase are attributed to cell-level responses

2.2 Compliant/stiff configurations

- 2.2a The presence of stiff inclusions result in a higher lattice stiffness compared to an equivalent uniform lattice
- 2.2b The crack tip deformation field shifts to wrap around stiff inclusions, but still retain the double-lobed butterfly shape
- 2.2c The primary toughening mechanism is crack deflection caused by the inclusions
- 2.2d A cluster of inclusions forces cracks to take a tortuous path, while functionally-graded inclusions do not initially impede crack growth, but force a tortuous path as fracture progresses

2.3 Stiff/compliant configurations

- 2.3a Removing material in the form of weak channels will promote crack growth and result in a consistent fracture pattern; fracture is arrested by a stiff phase at the end of the channels
- 2.3b A consequence of removing material is slightly lower lattice stiffness and lattice fracture toughness
- 2.3c Deformation concentrations are primarily observed in the weakened regions

II

Methodology and Results

5

Methodology

To answer the research question and challenge the hypotheses presented in Chapter 4, a research methodology was devised to explore lattice mechanical response in terms of lattice stiffness, lattice fracture toughness, fracture patterns, and cell deformation behavior.

From a base specimen design, two sets of lattices were manufactured: a set of lattices with a single relative density which is varied across the set and a set of lattices with one of four hierarchical topologies which were implemented by locally-varying relative density. Lattices were tested in uniaxial tension. Force-displacement data was recorded and used to obtain information on lattice stiffness behavior during loading and calculate lattice elastic modulus and fracture toughness. Two cameras, one low-speed and one high-speed, capture cell deformations and fracture behavior, respectively. Images from the former were used to visualize and quantify cell deformation behavior using a DIC-like method. Images from the latter were used to understand lattice behavior at the instantaneous moment of fracture.

5.1. Base specimen design

The final specimen design aims to minimize the number of variables during testing, leaving relative density as the primary experimental variable. The general configuration of all lattices is shown on the left side of Figure 5.1. All lattices were built from hexagonal unit cells for two reasons: 1) key assumptions made in literature are based on the hexagonal unit cell, and 2) due to their bending-dominated nature, hexagonal unit cells, in theory, are more sensitive to relative density than other topologies, making them ideal for investigating the effects of relative density and structural hierarchy.

To accurately capture lattice behavior and minimize clamping effects, it is crucial to design lattices with as many cells as possible given the constraints of the Form2 printer, namely print consistency, maximum build size, and print time. Therefore, dimensions were chosen such that two specimens could be printed on one build platform. The final lattice design consists of specimens with 39 rows and 20 columns of cells and a cell size of 3[2]. Specimen thickness of 8mm was a constraint of the hydraulic grips used for testing. An initial flaw, consisting of several consecutive missing struts spanning approximately 20% of the specimen's width, simulates an existing crack.

To improve lattice placement consistency during testing, an interlocking slider and clamping block were designed, shown on the right side of Figure 5.1. The clamping blocks were placed in the test machine at the beginning of testing and remain there for the duration. The slider, added to the ends of the lattice, has a tapered design which allows for easy insertion. A small lip at the opening of the clamping block allows the slider to snap into place, preventing lateral movement during testing.

5.2. Material and manufacturing

Specimens were manufactured using two Formlabs Form2 SLA printers (Friendly Fly and Sturdy Zebra) from Standard Black photopolymer resin (FLGPBK04). Clamping blocks were manufactured using Formlabs Tough resin (FLTOTL05). After printing, specimens were cleaned with isopropyl alcohol in a Form Wash cleaning station and cured in a Form Cure UV curing chamber for 120 minutes at 60°C. Post-cure, specimens were immediately stored in a dark environment until testing, as photopolymer parts continue to cure in ambient lighting.

Table 5.1: *Material properties for Standard Black resin given by Formlabs [1]*

σ_{fs}	65 MPa
E	2.8 GPa
E_{bend}	2.2 GPa
ε_{break}	6%

[2] An alternate definition for cell size was used here to avoid the confusing definition presented in Chapter 3. Cell size is taken as the square root of unit cell area. Here, the area of one cell is 9mm^2, giving a cell size of 3.

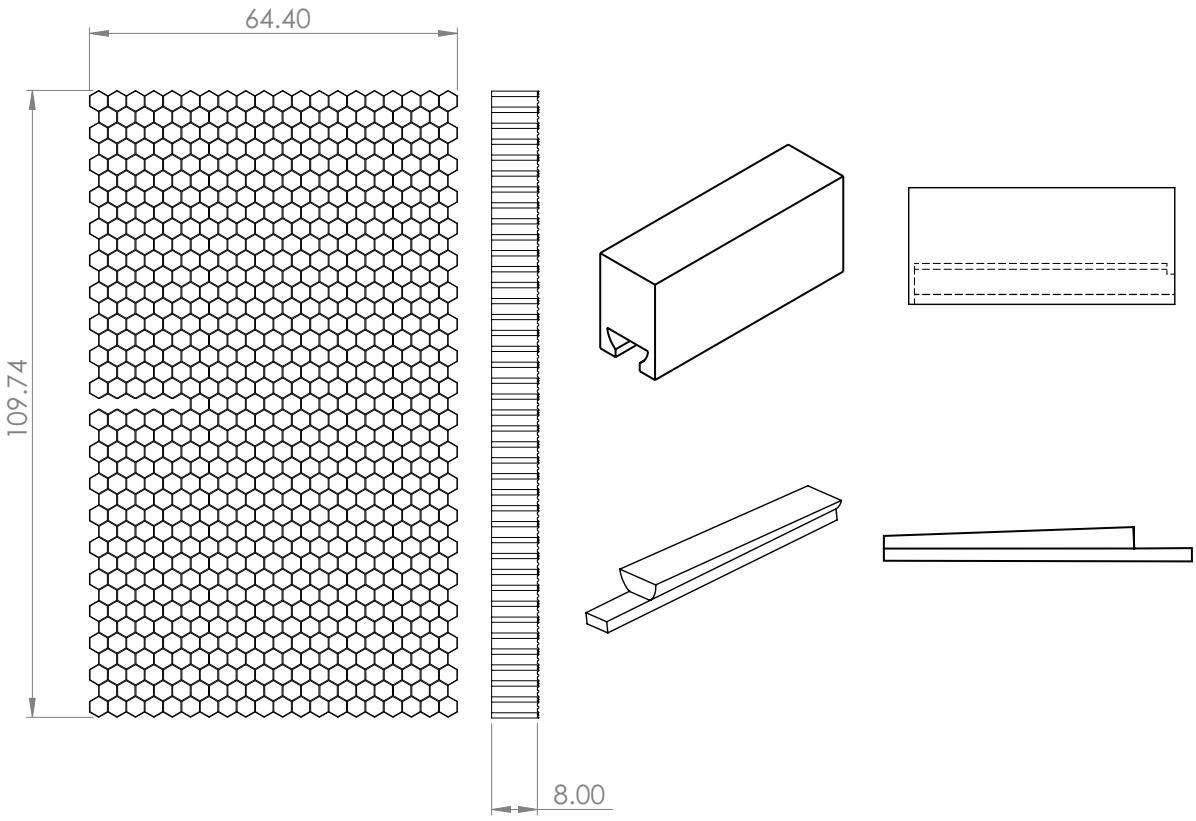

Figure 5.1: *Front and side views of the base lattice design (left) and isometric and side views of slider and clamping block parts (right)*

Black resin was chosen for its brittle properties, a summary of which can be found in Table 5.1. For this research, the material properties provided by Formlabs were taken as accurate and finished parts are considered isotropic. Specimens with no observable flaws (e.g. collapsed or missing struts, misaligned layers, debris trapped in cells, etc.) were considered to be ”good”. This is discussed in further detail in Chapter 6.

5.3. Test matrix

The experimental setup of this research was divided into two phases: uniform relative density lattices and lattices with structural hierarchy. All specimens were given a unique part number for identification with the format ”Set ID_Print Number”. As an example, the third printed $\bar{\rho} = 0.16$ specimen would have the part number ”16_03”. For ease of reading, each set of lattices has an associated icon which will be used as a visual identifier throughout this document. These icons are given per set in Tables 5.2 and 5.3. Because it was not possible to quantify the statistical likelihood of defects in a lattice, it was decided to print as many specimens as possible within a reasonable amount of time, considering that some would ultimately be deemed not suitable for testing.

5.3.1. Uniform relative density lattices

The first phase was intended to provide insight into the relationship between relative density and mechanical response and serve as a baseline for comparing the responses of lattices with structural hierarchy. Most models described in literature assume results are valid for $\bar{\rho} < 0.20$. Therefore, three sets meet this criteria. Three additional sets have a higher relative density in order to more fully assess the impact of relative density on a wide range of lattices. Table 5.2 gives the test matrix for the uniform relative density lattices.

Table 5.2: *Test matrix for uniform relative density specimens*

$\bar{\rho}$	Icon	Set ID	# printed	t (mm)	Ideal mass (g)
0.08		08	8	0.132	17.9
0.12		12	8	0.200	20.5
0.16		16	8	0.270	23.1
0.20		20	20	0.340	25.7
0.30		30	20	0.526	32.1
0.40		40	20	0.721	38.6

5.3.2. Hierarchical lattices

Four topologies were selected for the second set of lattices, shown in Figure 4.1. All configurations contain a combination of $\bar{\rho} = 0.10$ and 0.30 cells. Table 5.3 gives the test matrix for the hierarchical lattices, including equivalent relative density.

Two topologies, Bamboo and Nacre, are predominantly compliant structures with stiff inclusions. For consistency, the stiff inclusions of both topologies are idealized as diamond-shaped sets of four cells. The gradient layout of the inclusions in the Bamboo structure is inspired by the functional grading seen in a bamboo stalk. The densely-packed inclusions of the Nacre lattice is based on the stacked aragonite tablets in a nacre microstructure, with the compliant struts in between acting as the compliant biopolymer.

Contrasting this layout are the Glass Sponge and Etching topologies, which mimic primarily stiff structures with select compliant regions. The Glass Sponge architecture is inspired by the layered structure of *M. Chuni* and the idealization created by Kolednik et al. [6]. The Etching topology is slightly different from the others, as it is not adapted based on a single natural structure. Instead, the topology was designed around the concept that many tough natural materials use pre-defined weak interfaces to guide cracks to structures that impede further growth. The compliant channels extending above and below the crack tip lead to a compliant ”sink” which is intended to blunt the crack tip and slow growth.

Table 5.3: *Test matrix for hierarchical specimens*

Configuration	Icon	Set ID	# printed	Equivalent $\bar{\rho}$	Ideal mass (g)
Bamboo		B	8	0.134	20.8
Nacre		N	8	0.122	20.0
Glass Sponge		G	8	0.269	28.4
Etching		E	8	0.291	29.6

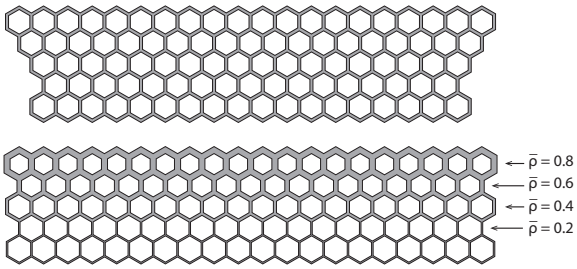

Figure 5.2: *Schematic representations of the tapered lattice (top) and density gradients (bottom) approaches for minimizing clamping effects.*

5.3.3. Specimen design variations

Boundary conditions Due to the compliance of the lattice relative to the solid slider, strategies needed to be adopted to minimize clamping effects, shown in Figure 5.2. A tapered, dogbone-like approach was taken for the uniform specimens, trimming one column of cells from each side of the lattice. This, however, resulted in some unintended effects which will be further described in Chapter 7; the tapering was replaced by a four-row relative density gradient in the hierarchical lattices which intended introduce load more gradually into the lattice.

Layer thickness In order to achieve good part quality, differing layer thicknesses were used to print the lattices. For uniform lattices of $\bar{\rho} \geq 0.20$, a resolution of 100 microns was sufficient, while the low strut thickness in $\bar{\rho} < 0.20$ lattices necessitated a resolution of 50 microns. Due to the $\bar{\rho} = 0.10$ regions, all hierarchical lattices were printed at a resolution of 50 microns. Practically, this should only impact print time; Formlabs' pre-processing software, PreForm, did not indicate that material volume changes with changing layer thickness.

Initial crack Contrary to the base specimen design, the Glass Sponge topology contains a center-crack flaw. This was chosen to better-mimic the *M. Chuni* structural hierarchy and prevent excessive strain energy from building up in the stiff phase of the lattice.

5.4. Measurement techniques

Quasi-static tension tests were performed using a Zwick 1455 10kN tension/compression bench fitted with hydraulic grips. Tests were displacement-controlled at a rate of 5mm/min and a preload of 20N was applied to account for specimens settling. Force vs. displacement measurements were captured by the onboard extensiometer at 100Hz.

To help capture cell deformation behavior, raised dots, hemispheres of radius 0.25mm, were printed onto the lattice face at each node and at the midpoint of each strut. After curing, the dots were painted with white tempera paint to provide contrast, shown in Figure 5.4a. The mass of the dots can be considered negligible. If density is assumed to be 1.20cm/g^3 [40] and a specimen contains around 4,500 dots, the maximum additional mass due to the dots is 0.178 grams. This is further reduced if the dot radius is larger than the strut thickness, as dots were cut to follow the cell's inner perimeter, shown in Figure 5.4b.

During testing, two cameras were used to capture lattice deformation. Over the full duration of a test, an Optomotive Velociraptor camera records images at 2fps. Analog output from the Zwick extensiometer was simultaneously recorded to correlate each image with a force. A Photron Fastcam Mini camera recording at 6,400fps was used to record brittle fracture which could not be sufficiently captured by the Optomotive Velociraptor. The purpose is purely qualitative; high-speed images do not have any force-displacement data associated with them.

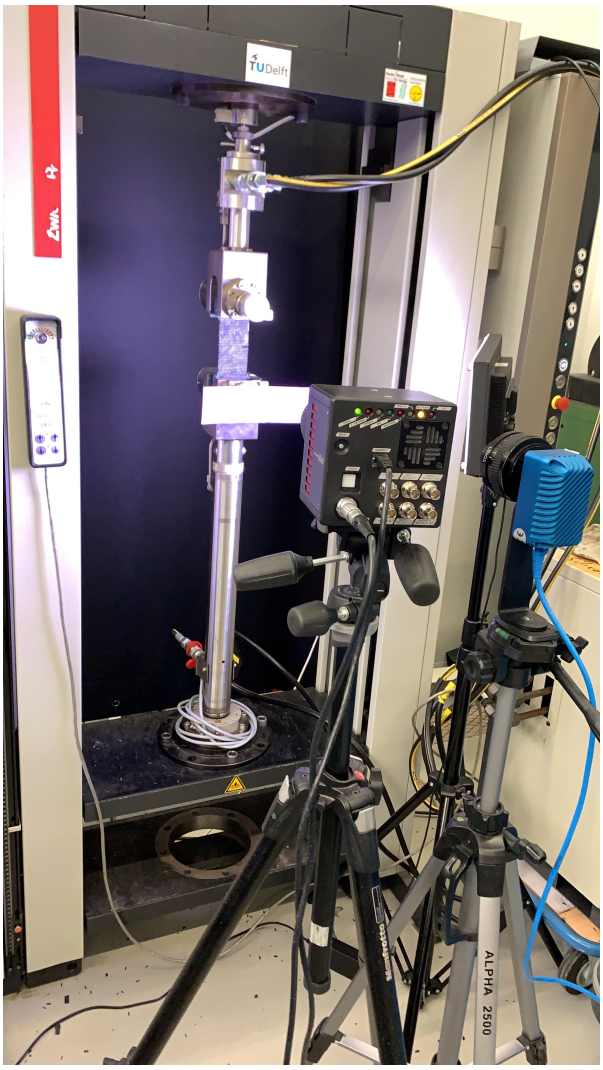

Figure 5.3: *Photo of tensile test setup with a lattice loaded in the test machine. The Photron camera is in the center of the photo, with the Optimotive Velociraptor just to the right.*

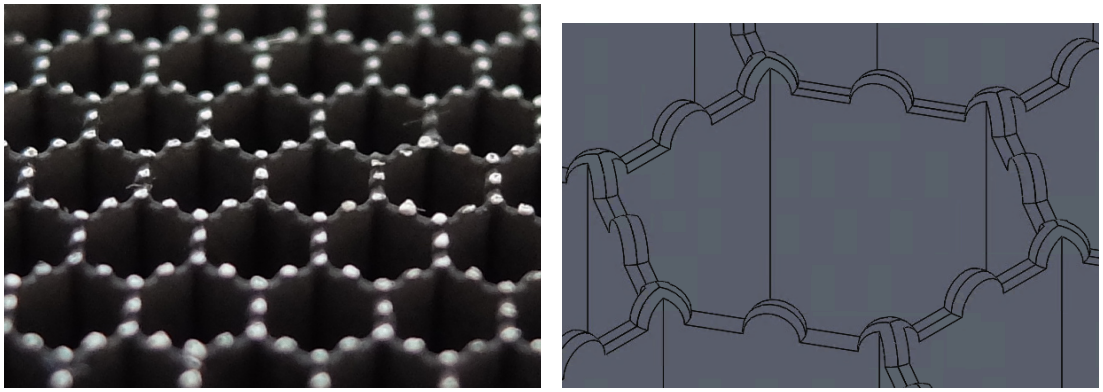

(a) **(b)**

Figure 5.4: *Left: Raised dots on the surface of a lattice after white tempera paint has been applied. Right: Zoomed-in isometric view of $\bar{\rho} = 0.12$ lattice showing the cut raised dots.*

5.5. Data processing

5.5.1. Lattice-level

The lattice-level data processing was comprised of three main parts: stress-strain response, lattice stiffness behavior, and bulk lattice properties.

Stress-strain response

From the force-displacement curves, stress-strain response was obtained by idealizing the lattice as a solid block of material with equivalent properties. Stress was obtained by dividing force by the cross-sectional area of the lattice, and strain was obtained by dividing displacement by the original length of the specimen.

Stiffness-displacement response

Lattice stiffness-displacement response was obtained by taking the first derivative of the stress-strain curve, resulting in a relationship between displacement and the lattice's tangent modulus throughout loading, providing insight on how the lattice is able to resist deformation at various points. As the initial result of this derivation is quite noisy, a local linear regression was applied to smooth the data.

Lattice elastic modulus and fracture toughness

Two lattice properties were of interest in this research, namely lattice elastic modulus and fracture toughness [3]. Lattice elastic modulus, $\bar{E}$ was determined by taking the slope of the stress-strain curve in the linear-elastic regime. Identification of the LE regime was supplemented by the stiffness-displacement response. Lattice fracture toughness, $\bar{K}_{IC}$ was calculated assuming the lattice to be a continuum with equivalent properties and calculating the stress intensity factor at the fracture stress, using the geometric parameters given in Figure 5.5 in Equations 5.1 and 5.2 for edge-cracked and center-cracked specimens, respectively.

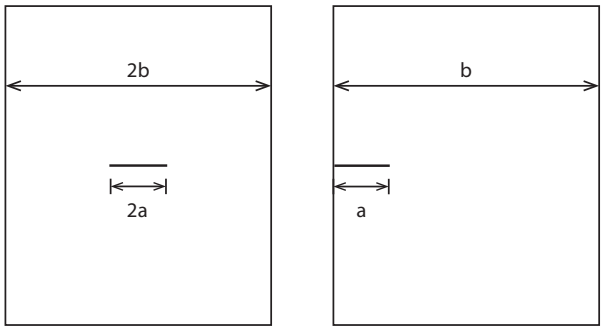

Figure 5.5: *Geometric parameters for a center-cracked (left) and edge-cracked (right) plate*

$$K_{IC} = \sigma_{fs}\sqrt{\pi a}\left[1.122 - 0.231\left(\frac{a}{b}\right) + 10.55\left(\frac{a}{b}\right)^2 - 21.71\left(\frac{a}{b}\right)^3 + 30.382\left(\frac{a}{b}\right)^4\right] \tag{5.1}$$

$$K_{IC} = \sigma_{fs}\sqrt{\pi a}\left[\frac{1 - \frac{a}{2b} + 0.326\left(\frac{a}{b}\right)^2}{\sqrt{1 - \frac{a}{b}}}\right] \tag{5.2}$$

To compare experimental results with literature, the resulting values for $\bar{E}$ and $\bar{K}_{IC}$ were input to the appropriate scaling law from Equations 3.2 or 3.3, respectively, and solved for coefficients B, b, D, and d, using a power1 curve fit in Matlab.

[3] To avoid confusion with properties commonly seen as material properties, the term "lattice" is added as a qualifier to the terms "elastic modulus" and "fracture toughness".

5.5.2. Cell-level

Cell-level behavior reintroduces the lattice as the honeycomb structure comprised of nodes and struts which adapt to increased loading both individually and cooperatively. Cell-level behavior analysis, therefore, stems from images taken during testing to understand how the lattice adapts to changing loads.

To quantify cell deformation behavior, the movement of each dot relative to its surroundings must be established. To that end, a DIC-like method was developed. An accompanying Matlab applet was concurrently developed for ease of use. The applet GUI can be seen in Figure 5.6 and will be used as a guide [4].

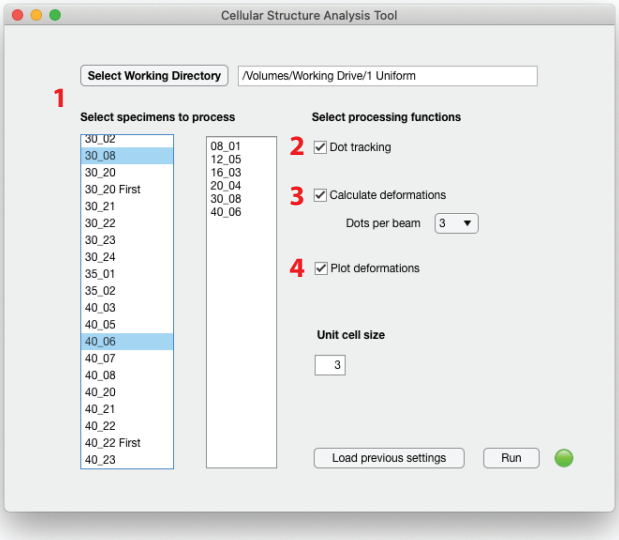

Figure 5.6: *User interface for the Matlab applet developed as a tool to streamline deformation calculations.*

1. **Specimen selection**
   From the selected working directory, a list of specimens which can be processed is generated in the left-hand column. Selected part numbers are automatically copied into the right-hand column.

2. **Establishing dot trajectory**
   Images are processed using an open-source particle tracking code developed by Crocker and Weeks which establishes the trajectory of each dot over the set of images (frames) [42]. The output is a matrix of all tracked dots and their xy-position per frame where each row corresponds to a single tracked dot and each column represents a frame.

[4] All Matlab code used and developed for this method can be found on Github [41]

3. **Deformation calculation**
   This step consists of several sub-steps, described below:

   (a) **Creating associations between dots**
   From the outputted xy-coordinates, associations must be created between dots which link them to neighboring dots to form a beam. This is done with the help of a 2D Delaunay triangulation. This process is shown in Figure 5.7 for a section of a lattice.

      i. **Delaunay triangulation**
      A Delaunay triangulation is applied to the xy-coordinates of dots in the first frame, resulting in a system of triangles connecting each point such that each triangle contains no interior points.

      ii. **Node identification**
      A node is identified exclusively as the confluence of three triangles. The three triangles which share this node as a vertex are noted.

      iii. **Midbeam identification**
      The remaining vertices of the three triangles are identified as midbeam dots connected to that node. Extraneous triangles associated with the midbeam dot are discarded.

      iv. **Reduction to only nodes and midbeams**
      Steps ii and iii are simultaneously applied to the entire lattice, resulting in a wireframe of only nodes and midbeams.

      v. **Beam identification**
      Full beams are associated by matching up half-beams which share a midbeam dot. Beam coordinates are stored as a matrix consisting of Node, Midbeam, and Neighbor xy-coordinates. Duplicate beams are discarded.

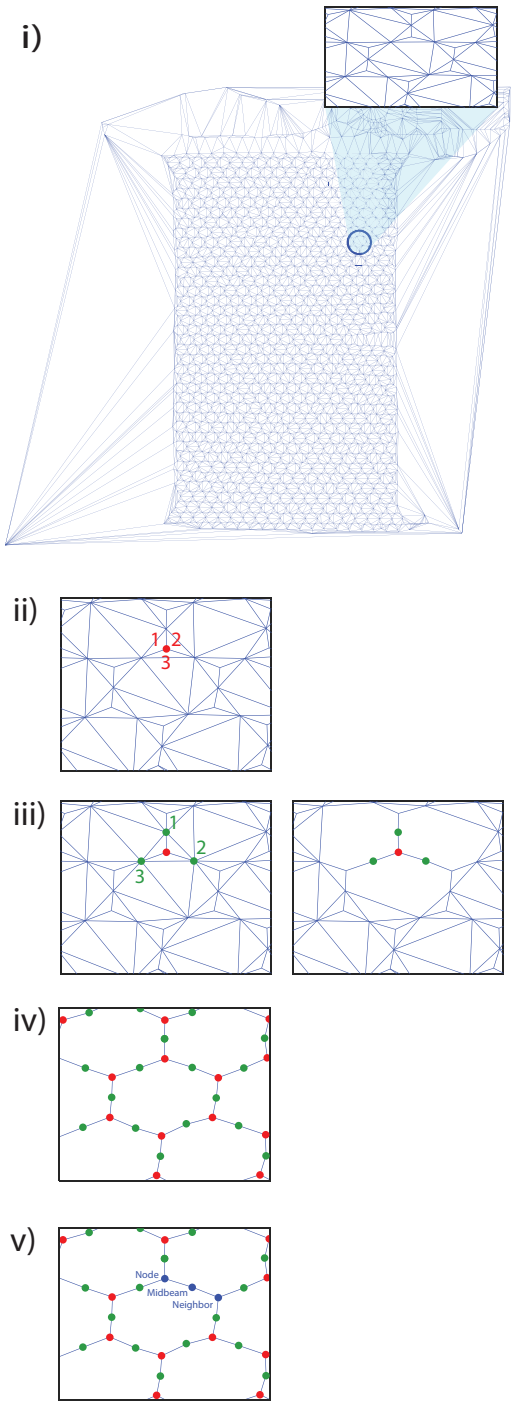

Figure 5.7: *Visualization of the method developed to associate dot position to form beams in order to calculate deformations in a lattice.*

(b) **Beam association through all frames**
Since only the first frame is used to create the beam associations, each dot in the newly-created matrix is correlated with the dot positions in the output matrix from Step 2. The result is a 3-dimensional matrix with associated Node, Midbeam, and Neighbor xy-coordinates for each frame.

(c) **Calculating deformation**
Two types of deformation are considered: elongation and rotation. Elongation is defined as the uniaxial deformation of the beam, given by:

$$\Delta L = \frac{L - L_0}{L_0} \tag{5.3}$$

Only positive elongations are considered. Negative elongations would be the result of various forms of beam bending that cannot be fully captured by uniaxial compression behavior.

Beam rotation is calculated as the change in angle of inclination of each strut compared to the first frame, shown in Figure 5.8. This is done by taking the four-quadrant inverse tangent (*atan2* function in Matlab), which automatically accounts for the direction of rotation.

4. **Visualizing results**
Lattice deformation results are visualized by plotting each beam as a line which an associated color. To minimize visual clutter, all beams are gray except those which are contributing to 90% of the total deformation; the cutoff value was chosen to balance visual clarity and usefulness. Beam colors are assigned based on the jet colormap.

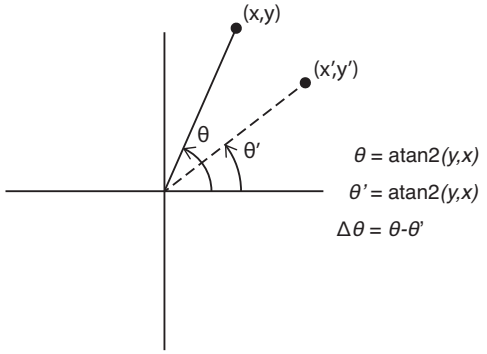

Figure 5.8: *Sample sketch of rotation deformation calculation using the atan2 function.*

6

Sources of Uncertainty

As with any research, every effort is made to ensure that results are free from unintended variation. The nature of research, especially experimental research, does not always lend itself to this, and variation is inevitable. In the spirit of providing a more complete picture, the following chapter addresses some potential sources of uncertainty in the results.

6.1. Material and manufacturing

The choice of material was primarily a practical one. As far as rapid prototyping processes go, SLA produces consistently high-quality, isotropic parts and was readily available in the DASML. Black Standard resin was chosen for ease of capturing image data during testing. With these choices came inherent uncertainties, namely in polymer behavior and the manufacturing process.

Polymer behavior In literature, the base material of a lattice is assumed to be linear-elastic, have an elastic-brittle response with no strain-rate or hydrostatic sensitivities. Manufacturing the experimental lattices from a polymer material, therefore, introduces some uncertainties which must be considered in the context of this work.

Polymers are notoriously weak in tension. This is partially due to their sensitivity to hydrostatic pressure, evidenced by the Von Mises yield surface for polymers, shown in Figure 6.1. Entanglements and polymer chain length also factor into this disparity. In compression, chain length is not an issue, as polymer chains densify with increasing load, thereby increasing stiffness and yield strength. In tension, however, the variation in chain length can lead to void formation, meaning that any structural weakness will become apparent much more quickly [43]; however, it is virtually impossible to know where these defects may be located, so this must be considered as a possible reason for premature failure.

Polymers are also strain-rate sensitive and exhibit viscoelastic behavior. All specimens were tested at a rate of 5mm/min to maintain consistency across the test matrix, but the lattice is also strain-rate sensitive; a 5mm/min test machine strain rate does not directly translate to a 5mm/min strain rate at all locations in the lattice itself. Consequently, further testing would be needed to determine lattice strain-rate sensitivity.

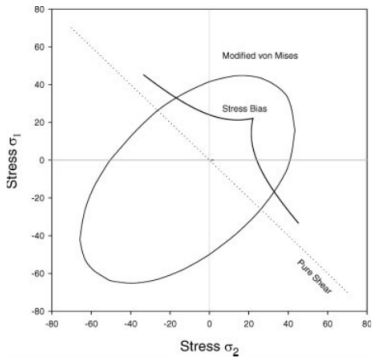

Figure 6.1: *Modified Von Mises yield envelope for polymer materials. Note the stress bias line which delineates the onset of crazing in polymers under tension [12].*

Material unknowns As Formlabs resins are proprietary, there is limited information about their composition and properties. The Standard Black resin MSDS states that it is a mixture of methacrylated oligomers and monomers, photoinitiators, and dye [44]. Therefore, for the purposes of analysis, it is assumed that final properties are similar to PMMA.

Manufacturing process There are several opportunities for uncertainty to arise in the manufacturing process. To determine the effects of various parameters, an informal study was conducted during the manufacture of a set of uniform lattices, where the printer used, date and time of print start and end, date and time of post-processing start and end, relative humidity and ambient temperature, and print quality were recorded and later compared to mechanical performance. The full results accompanied by a short discussion can be found in Appendix A. It was concluded that visual print quality was the determining

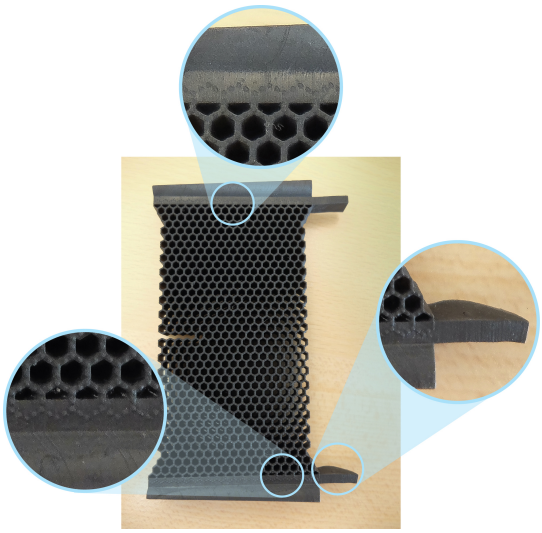

Figure 6.2: *Examples of poor-quality lattices. Note the filled cells in the top row, the lack of definition in the raised dots, and separation between the slider and pull-tab*

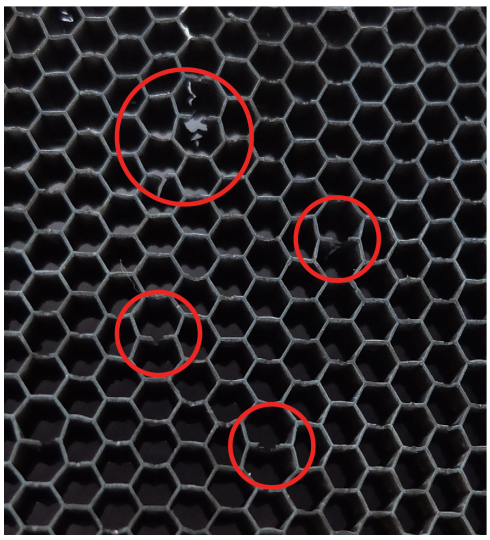

Figure 6.3: *Partially-broken struts in a $\bar{\rho} = 0.08$ lattice due to support material removal*

factor in mechanical response. Parts with resin-filled cells or those that lacked sharp internal vertices, exemplified in Figure 6.2, did not perform consistently relative to parts of the same relative density. Going forward, it was assumed that visually-okay parts were also structurally acceptable.

Upon completion of post-processing, support material was removed from parts. Particularly at low relative densities, this sometimes resulted in partially-broken struts, shown in Figure 6.3 with red circles highlighting some damaged areas. In theory, this should not impact mechanical behavior significantly; small variations z-direction strut thickness slightly alter the cross-sectional area at that location, but in the context of the full lattice, it is assumed that these should not substantially affect structural integrity.

6.2. Specimen design

Switching from the dogbone-like end configuration in the uniform lattices to the density gradient configuration in the hierarchical lattices was done to minimize interference from the sharp change in stiffness near the clamp, based on knowledge gained during testing. This decision comes with uncertainty. Since the uniform lattices were not repeated with this density gradient, it is reasonable to assume this change has a not-insignificant effect on mechanical response, and caution should be taken when interpreting and comparing results, particularly lattice-level results.

6.3. Testing

Further uncertainty is related to the experimental setup itself. The decision to design and use fixed clamping blocks was driven by testing ease and repeatability. The same guide tools were used any time blocks were placed or replaced, making it reasonable to assume that all specimens experienced loading in the same way. Because blocks did occasionally break outside of testing, several sets of clamping blocks were produce and were assumed to have the same properties and dimensions.

7

Results

This chapter presents the results of the experimental and analysis methods described in Chapter 5 and is divided into two main sections: uniform relative density lattices and hierarchical lattices. Each section is further divided into lattice-level and cell-level results. Where applicable, relevant observations made during testing are also included. Interpretation of the following results and observations, as well as a more-detailed discussion on their implications, will be done in Chapters 8 and 9 for the uniform and hierarchical sets, respectively.

Every tested specimen has a large set of test data and images and processed data associated with it, making it impractical to provide all results in this chapter. Therefore, for ease of reading and convenience, results can be explored in several ways, outlined in Table 7.1[5].

Table 7.1: *Summary of available data and results, including location.*

Location	Test images	Force-displacement and derived data	$\bar{E}$, $\bar{K}_{IC}$	Fracture path	Deformation fields
Chapter 7	-	Representative specimens	Average per set	Representative specimens	Representative specimens (still image only)
Appendix C	-	Select additional specimens	-	Select additional specimens	Select additional specimens (still image only)
Online	All specimens	All specimens	-	All specimens	All specimens (still images and videos)

7.1. Uniform relative density lattices

7.1.1. Lattice-level

A summary of lattice level results can be found in Table 7.2 with number of specimens tested, mass characteristics, and average force-displacement behavior for each relative density set.

Table 7.2: *Summary of mass characteristics and force vs. displacement response for all specimens. Column 2 reflects the number of specimens used for analysis, and the discrepancy between the number of specimens in Tables 5.2 and 7.2 is a result of either poor print quality, accidental fracture prior to testing, or unsalvageable dot painting.*

Configuration	# tested	Avg. actual mass (g)		Avg. F_{max} (N)	Avg. ΔL (mm)
8	5	20.2	(12.8%)	177.83	14.63
12	5	20.6	(+0.5%)	153.78	11.49
16	5	22.3	(-3.5%)	203.64	12.79
20	6	24.8	(-3.5%)	399.30	13.49
30	8	30.0	(-5.0%)	695.04	8.48
40	9	36.0	(-6.7%)	1378.60	5.87

[5]Online data can be found on OSF

Force vs. displacement

Figure 7.1 shows the unaltered force vs. displacement curves for a representative specimen per relative density. As the force-displacement behavior varied slightly within a set, the representative specimen was chosen to be one whose force-displacement curve fell more-or-less in the middle of the set in terms of maximum force and displacement. The corresponding stress-strain curves derived from the force-displacement curves are given in Figure 7.2. Representative stiffness curves for each relative density are given in Figure 7.3. During testing, a brief cracking noise was often heard in several lattices of all relative densities around the point where the slope of the force-displacement curve noticeably changes.

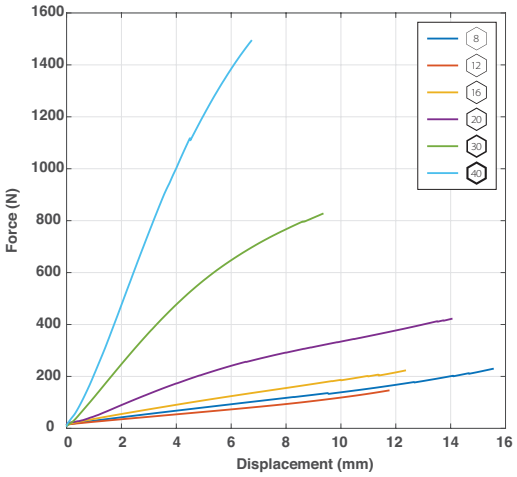

Figure 7.1: *Raw force-displacement curves for representative specimens of each uniform relative density set.*

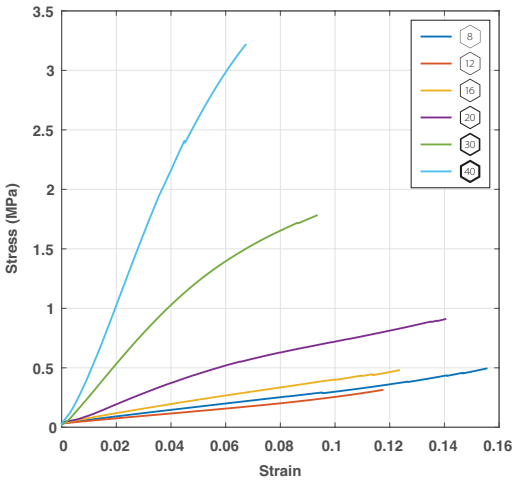

Figure 7.2: *Resulting stress-strain curves for representative specimens of each uniform relative density set.*

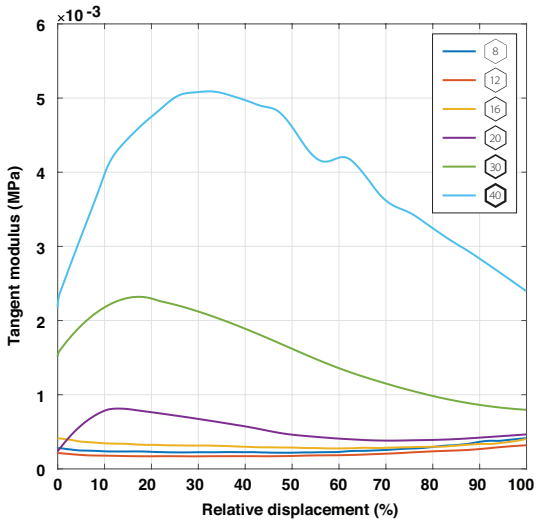

Figure 7.3: *Stiffness curves for representative specimens of each uniform relative density. Stiffness is plotted w.r.t. relative displacement such that all curves are plotted from 0 to 100% of total displacement.*

Lattice elastic modulus and fracture toughness

Figures 7.4 and 7.5 show the average lattice elastic modulus and lattice fracture toughness per relative density, respectively. As described in Section 5.5.1, lattice fracture toughness is calculated based on an initial crack length; however, fracture did not consistently initiate at the existing crack tip. Therefore, when fracture initiated elsewhere in the lattice, the value for a was set based on the number of fractured cells which constituted the ”new” crack tip, illustrated in Figure 7.6. If fracture initiated at a point where no cell walls had broken, a is taken to be the width of one cell [7].

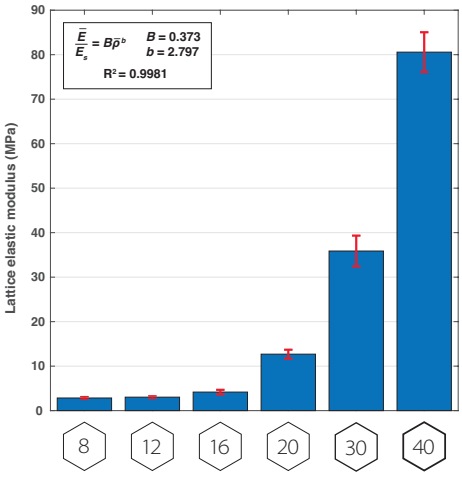

Figure 7.4: *Average lattice elastic modulus for all uniform relative density sets. Error bar indicates standard error of the mean.*

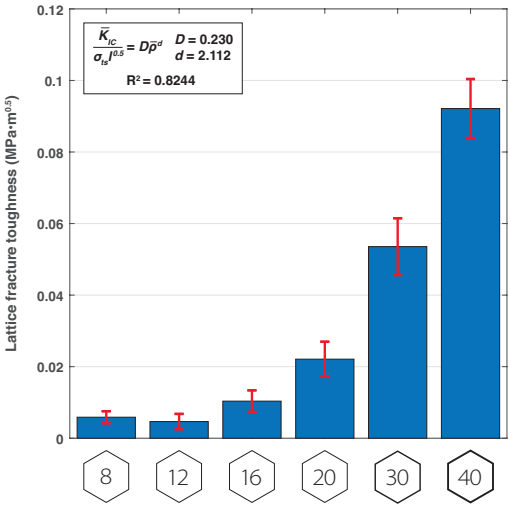

Figure 7.5: *Average lattice fracture toughness for all uniform relative density sets. Error bar indicates standard error of the mean.*

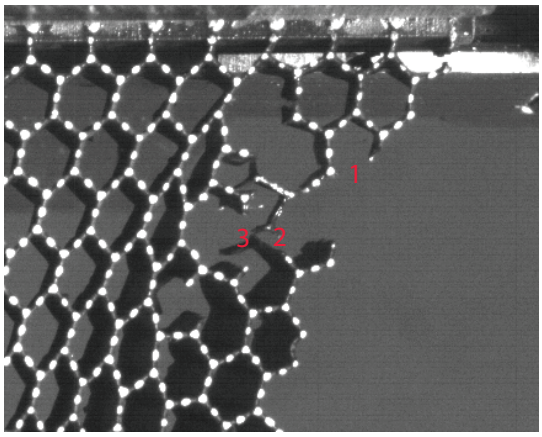

Figure 7.6: *Example of lattice with an altered value for crack length, a, to calculate $\bar{K}_{IC}$. The lattice failed at the upper-right hand corner where three cells had already fractured. Therefore, the value for a is changed to reflect this ”crack length”.*

7.1.2. Cell-level

This section presents the cell-level results, consisting of the fracture images and deformation fields.

Fracture

Using images from the Optomotive Velociraptor camera, a timeline of damage progression was established. High-speed images, if available, were used to determined which strut failure initiated final fracture. Figure 7.8 shows the extent of damage in the representative lattices; the final fracture path(s) is indicated by a red line, the catalyzing fracture, if known, is shown in yellow, and any intermediate fractures which did not induce final fracture, are shown in blue.

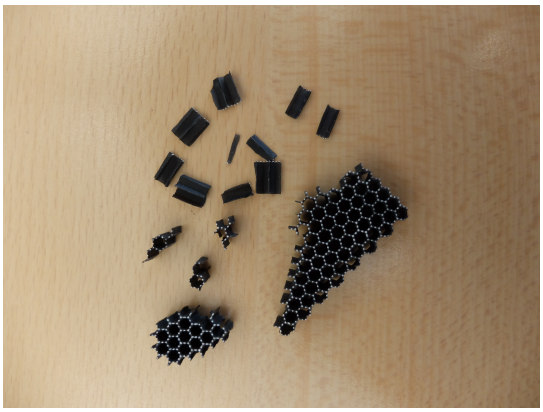

Figure 7.7: *Samples of debris of various sizes which broke from lattices during testing.*

Fracture in all specimens often resulted in debris of varying size, ranging from one to two struts to large chunks which blew out from the lattice, shown in Figure 7.7. In low-density lattices, fracture was aurally characterized by several cracking noises in succession, followed by final fracture which did not necessarily propagate through the entire lattice. At high relative densities, by contrast, fracture occurred loudly, violently, and with little warning; the latter two are illustrated by high-speed images which can be viewed here.

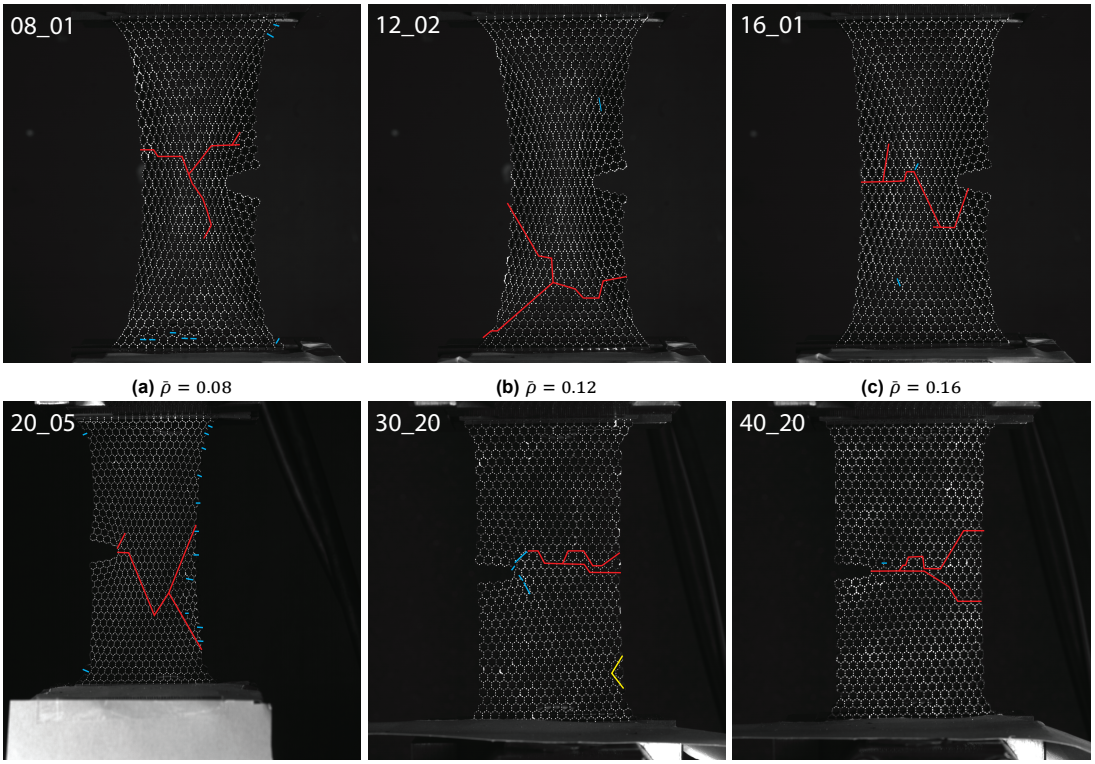

(a) $\bar{\rho} = 0.08$ **(b)** $\bar{\rho} = 0.12$ **(c)** $\bar{\rho} = 0.16$

(d) $\bar{\rho} = 0.20$ **(e)** $\bar{\rho} = 0.30$ **(f)** $\bar{\rho} = 0.40$

Figure 7.8: *Fracture paths for selected specimens of each uniform relative density set*

Deformation fields

The elongation and rotation deformation fields for representative lattices are given in Figures 7.9 and 7.10, respectively. A summary of the average maximum elongation and rotation values per relative density is given in Figure 7.11. There are sporadic gaps in the deformation fields. There are two conditions that could cause this:

1. A dot was not visible or distinguishable to the particle tracking code. Consequently, when the Delaunay triangulation is applied the surrounding unit cell is not processed and leaves a gap in the deformation field.

2. There is an erroneous dot close to a node, resulting in a node that is the confluence of four triangles, not three. The dot is, therefore, not identified as a node. Widening the search scope to include the confluence of four triangles would have required additional, highly specific constraints to accurately identify the node in these cases and was deemed not necessary given that this condition does not occur frequently.

While the deformation fields are useful for understanding where deformations concentrate in the lattice, it is difficult to discern and appreciably understand how deformation is distributed throughout the lattice. Therefore, a half-normal distribution is fitted to the histogram of all (elongation and rotation) deformation in the final frame in order to more-easily visualize this distribution. An example is illustrated in Figure 7.12, and Figure 7.13 shows the average distribution function per deformation type per relative density.

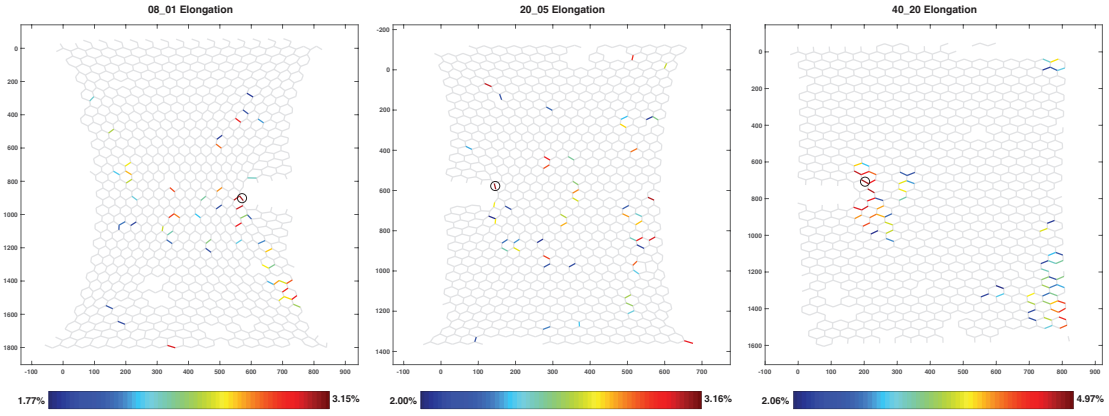

(a) $\bar{\rho} = 0.08$ **(b)** $\bar{\rho} = 0.20$ **(c)** $\bar{\rho} = 0.40$

Figure 7.9: *Elongation deformation fields for* $\bar{\rho} = 0.08, 0.20,$ *and* 0.40 *lattices*

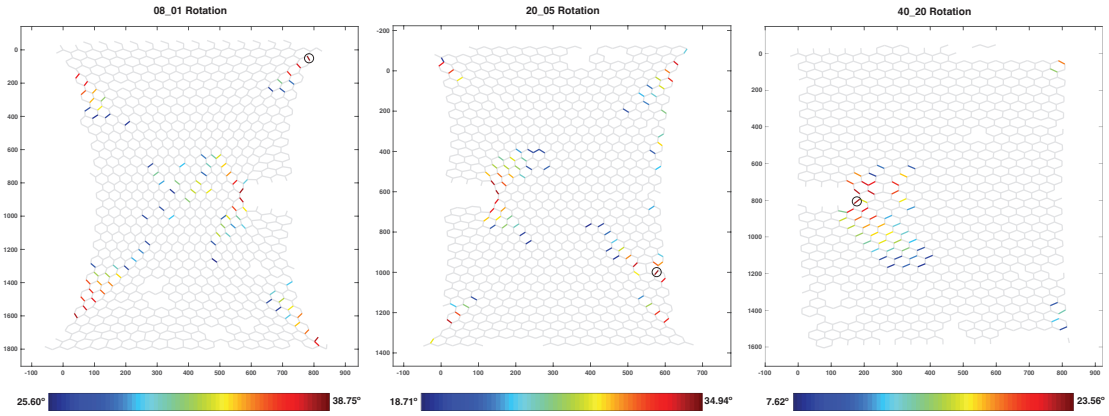

(a) $\bar{\rho} = 0.08$ **(b)** $\bar{\rho} = 0.20$ **(c)** $\bar{\rho} = 0.40$

Figure 7.10: *Rotation deformation fields for* $\bar{\rho} = 0.08, 0.20,$ *and* 0.40 *lattices*

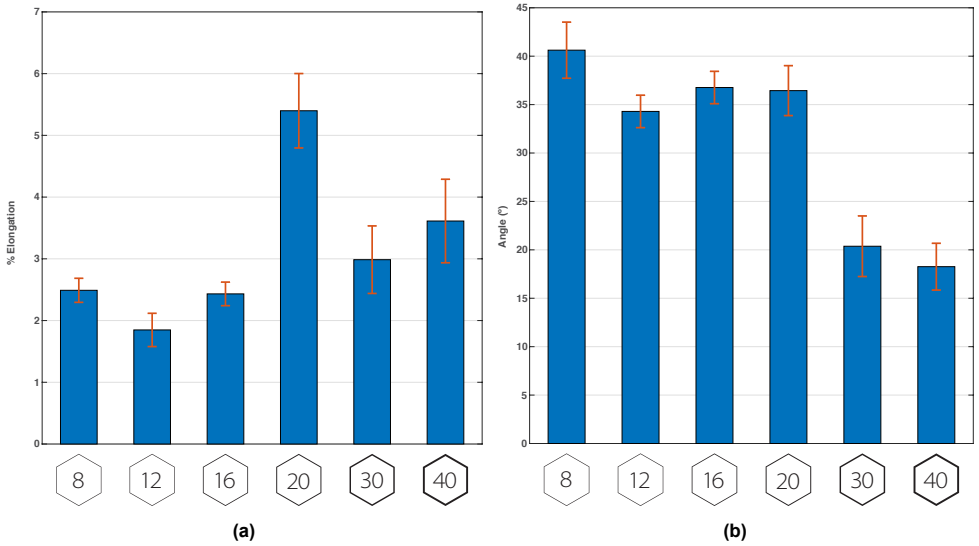

Figure 7.11: *Average maximum beam elongations (left) and rotations (right) in the final frame prior to failure in uniform relative density lattices. Error bar represents the standard error of the mean.*

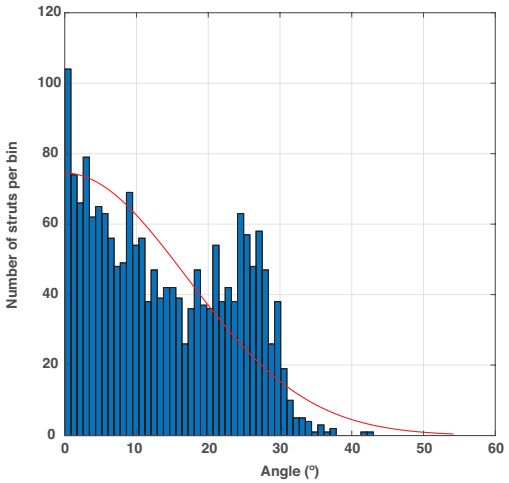

Figure 7.12: *Example of half-normal distribution fitted to the histogram of all beam rotations in the final frame of a $\bar{\rho} = 0.08$ lattice.*

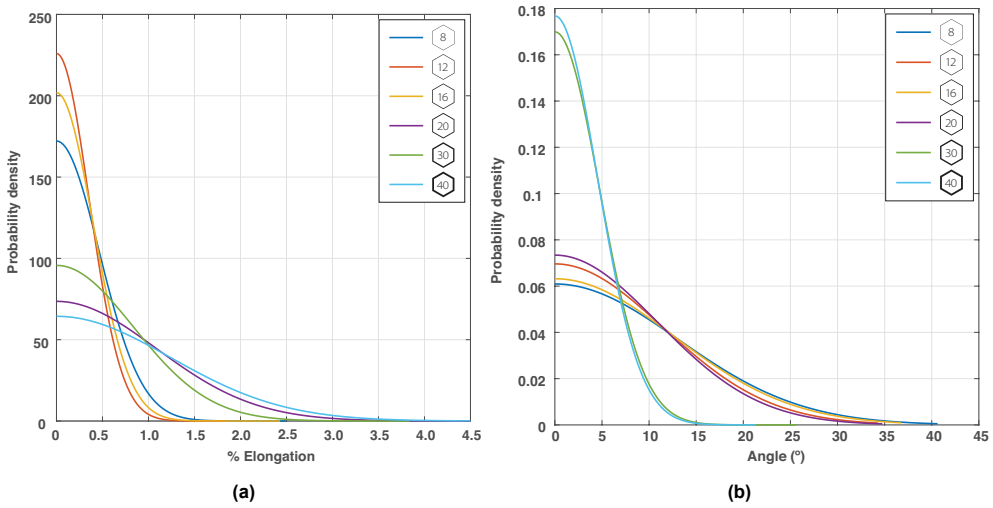

Figure 7.13: *Average half-normal distribution fit for beam elongations (left) and rotations (right) in uniform relative density lattices.*

7.2. Hierarchical lattices

7.2.1. Lattice-level

A summary of lattice level results can be found in Table 7.3 with number of specimens tested, average mass characteristics, and average force-displacement behavior per hierarchical configuration. Both 3D printers underwent maintenance prior to this set. Combined with an improved understanding of dot painting, a larger fraction of printed lattices were deemed suitable for tested. One challenge emerged for the Etching lattices, however; the angle of the compliant channel left these lattices susceptible to shearing while placing them in the clamping blocks. Extra care was taken to ensure fracture would not occur during this step, but nonetheless a few lattices were lost prior to testing.

Table 7.3: *Summary of mass characteristics and force vs. displacement response for all specimens*

Configuration	# tested	Ideal mass (g)	Avg. actual mass (g)		Avg. F_{max} (N)	Avg. ΔL (mm)
	5	20.8	23.5	(13.0%)	198.05	6.80
	5	20.0	21.3	(+6.5%)	148.32	5.68
	6	28.4	28.4	(-)	605.67	4.80
	6	29.6	29.2	(-1.0%)	445.83	3.66

Force vs. displacement

Figure 7.15 shows the unaltered force-displacement curves for a representative lattice of each hierarchical configuration, and the stress-strain curves derived from the force-displacement behavior are shown in Figure 7.16. The corresponding representative stiffness curves for each hierarchical set are given in Figure 7.14.

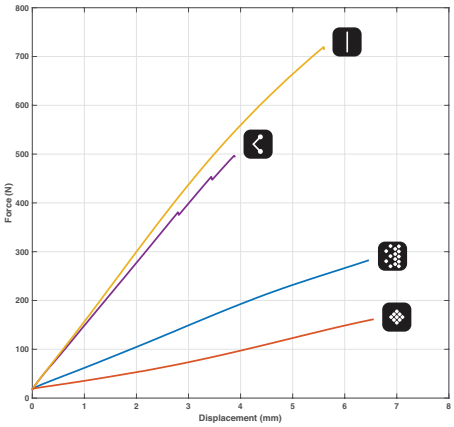

Figure 7.15: *Raw force-displacement curves for representative specimens of each hierarchical lattice configuration.*

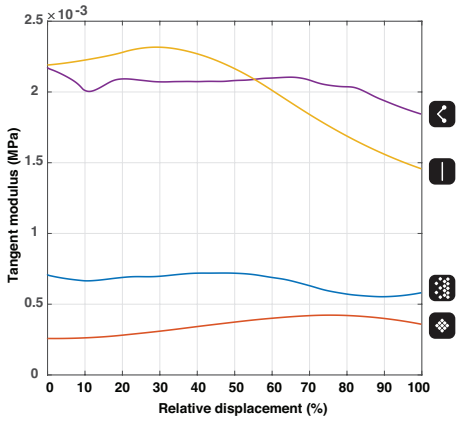

Figure 7.14: *Stiffness curves for a representative lattice of each hierarchical configuration. Stiffness is plotted w.r.t. relative displacement such that all curves are plotted from 0 to 100% of total displacement.*

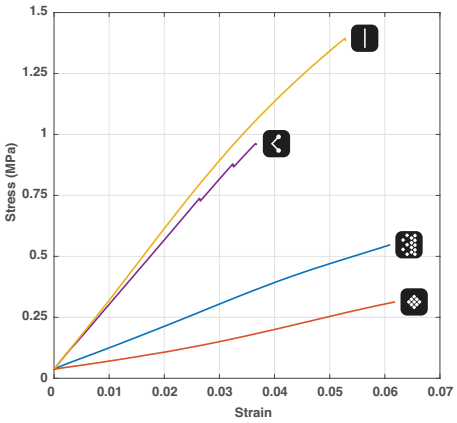

Figure 7.16: *Resulting stress-strain curves for representative specimens of each hierarchical configuration.*

Lattice elastic modulus and fracture toughness

Figure 7.17 shows the lattice elastic modulus and lattice fracture toughness values obtained for the hierarchical lattices. Similar to the uniform relative density lattices, the value of a for lattice fracture toughness was adjusted depending on where fracture initiated.

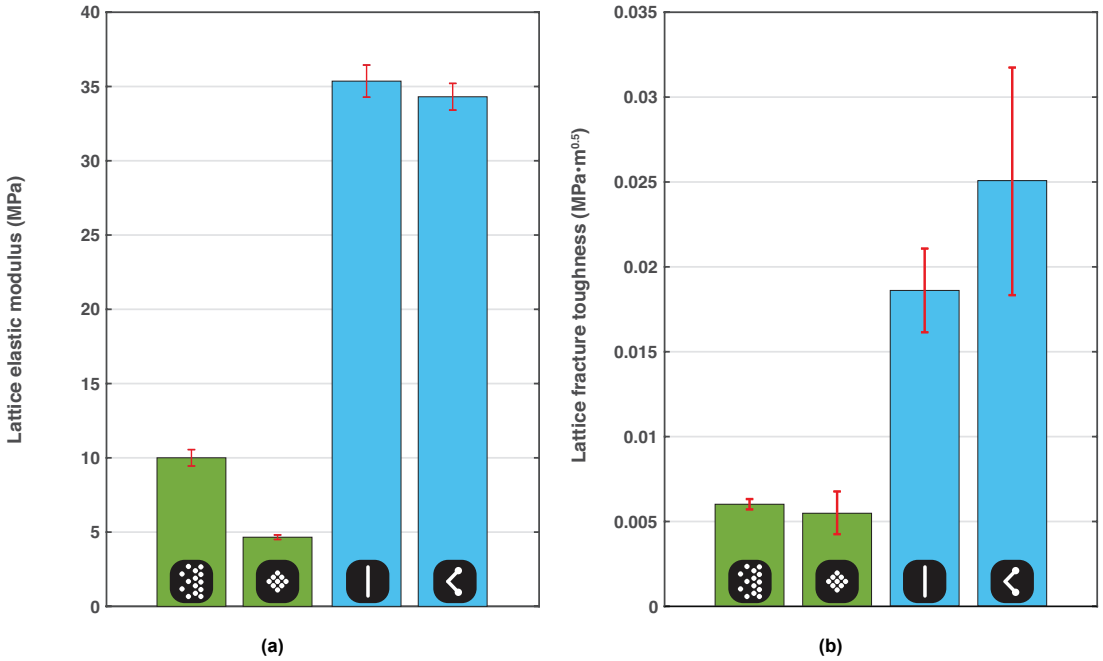

Figure 7.17: *Average lattice elastic modulus (left) and lattice fracture toughness (right) for all relative density sets. Error bar indicates standard error of the mean.*

7.2.2. Cell-level

Fracture

Figure 7.18 shows the fracture patterns for representative lattices of each configuration. Like the uniform lattices, the final fracture path is indicated by a red line, the catalyzing fracture, if known, is shown in yellow, and any intermediate fractures which did not induce full failure are shown in blue.

Fracture occurred quite quickly in all hierarchical lattices, though there were differences in the explosiveness of varying configurations. These differences are best illustrated by the high-speed images for a Nacre and Glass Sponge lattice, which can be viewed here. The exception to this are two Bamboo lattices (B_04 and B_06) which experienced partial fracture and continued to withstand loading for several more millimeters.

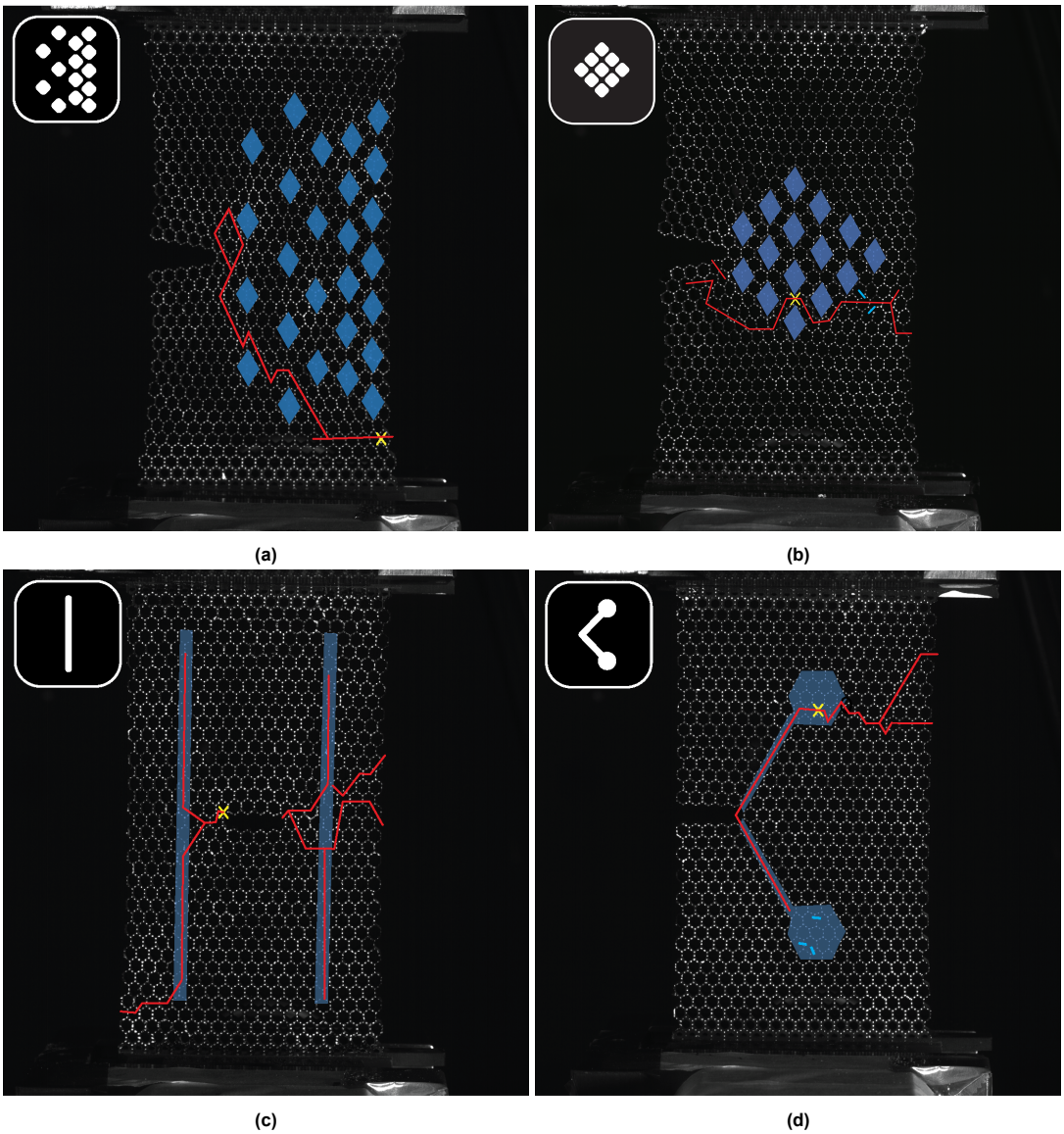

Figure 7.18: *Fracture paths of representative specimens of each hierarchical configuration. The transparent blue areas indicate the location of the stiff inclusions or compliant regions.*

Deformation fields

The elongation and rotation deformation fields for a representative hierarchical lattice are given in Figures 7.19 and 7.20, respectively. A summary of the average maximum elongations and rotations per configuration are presented in Figure 7.21. Like the uniform relative density lattices, a half-normal distribution function can be fitted to the histogram containing all deformation values in the final image before fracture, shown in Figure 7.21.

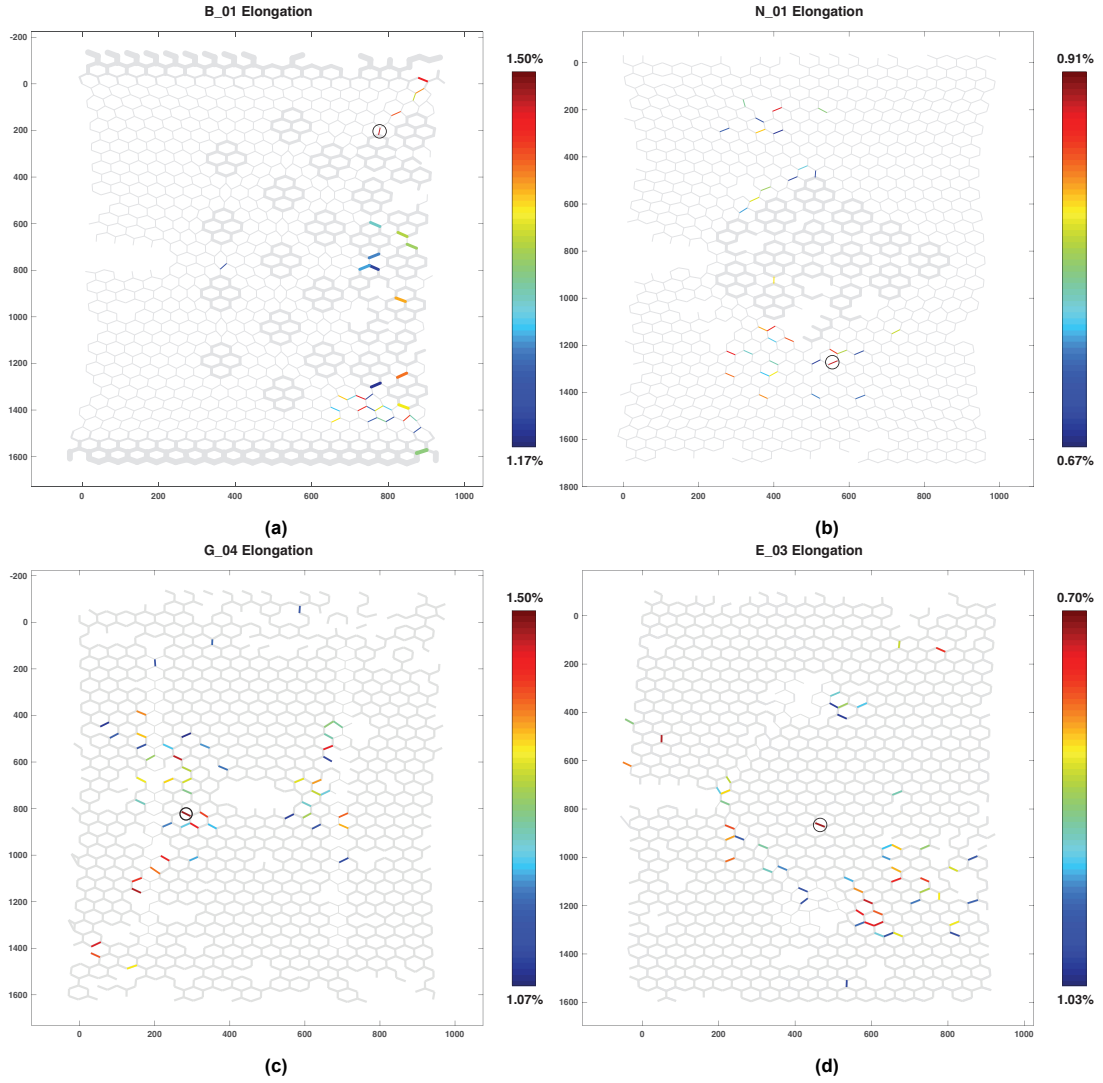

Figure 7.19: *Elongation deformation fields for hierarchical lattices. Clockwise from top-left: Bamboo, Nacre, Etching, Glass Sponge*

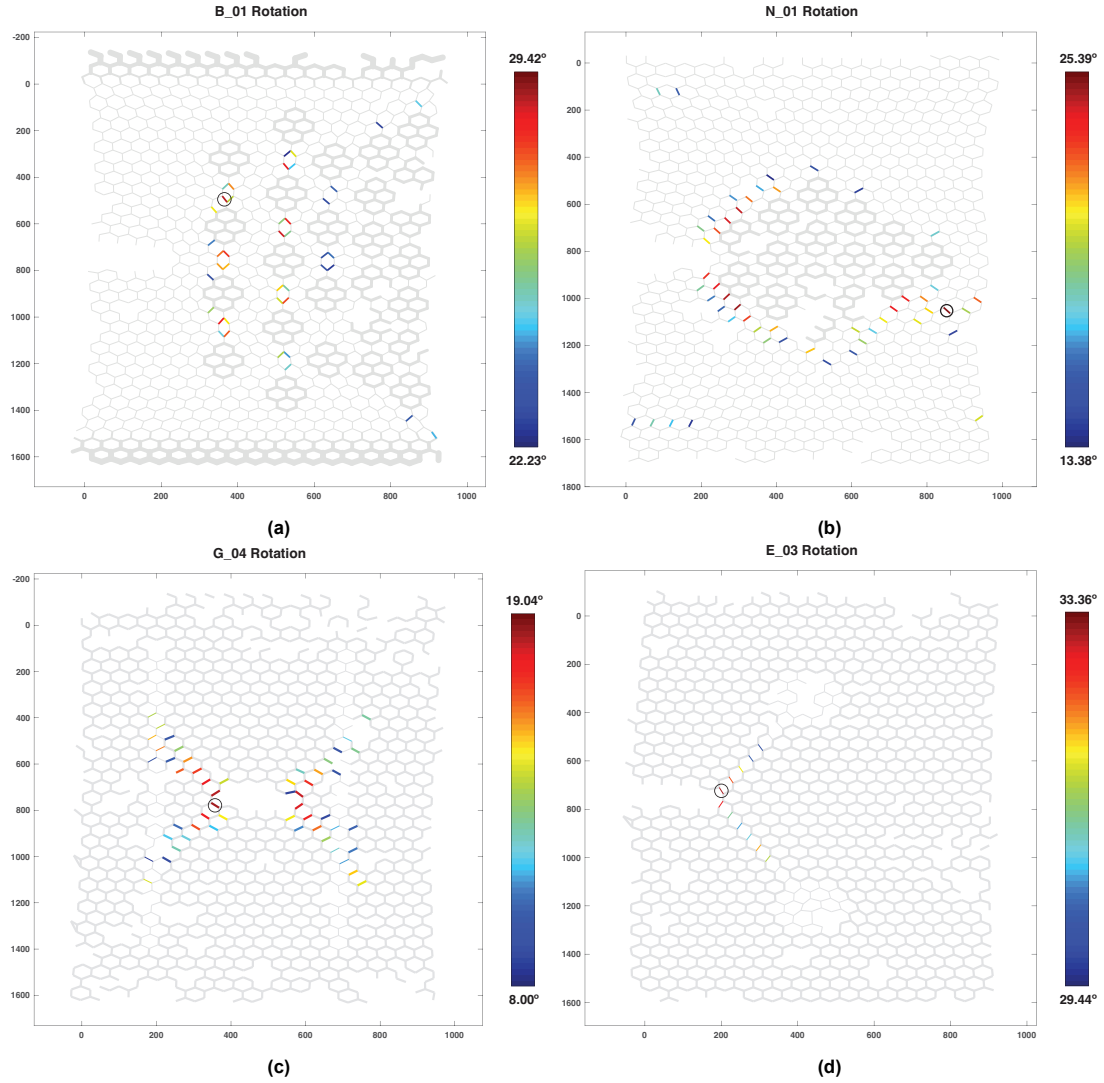

Figure 7.20: *Rotation deformation fields for hierarchical lattices. Clockwise from top-left: Bamboo, Nacre, Etching, Glass Sponge*

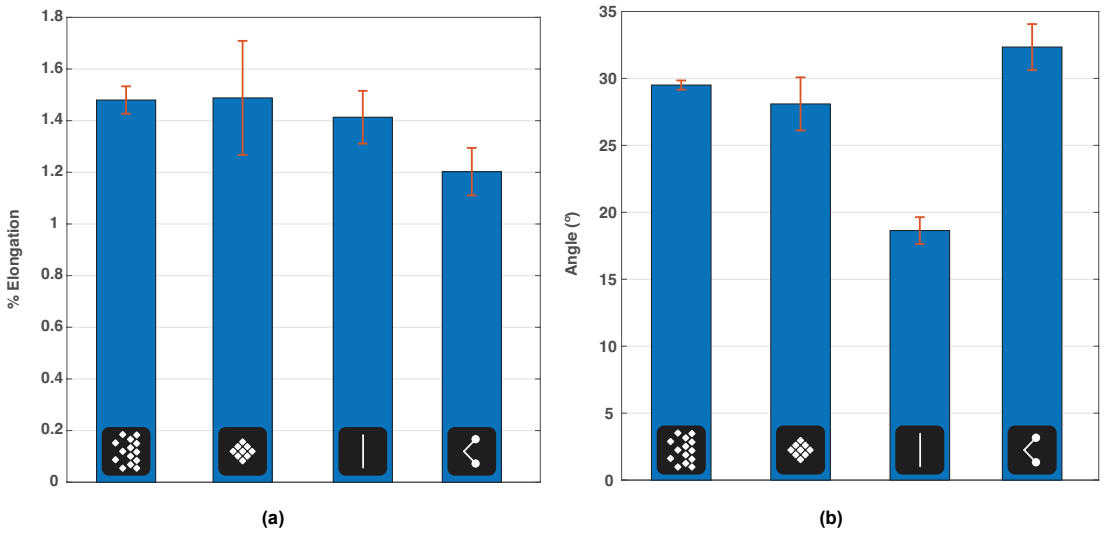

Figure 7.21: *Average maximum beam elongations (left) and rotations (right) in the final frame prior to failure in hierarchical lattices. Error bar represents the standard error of the mean.*

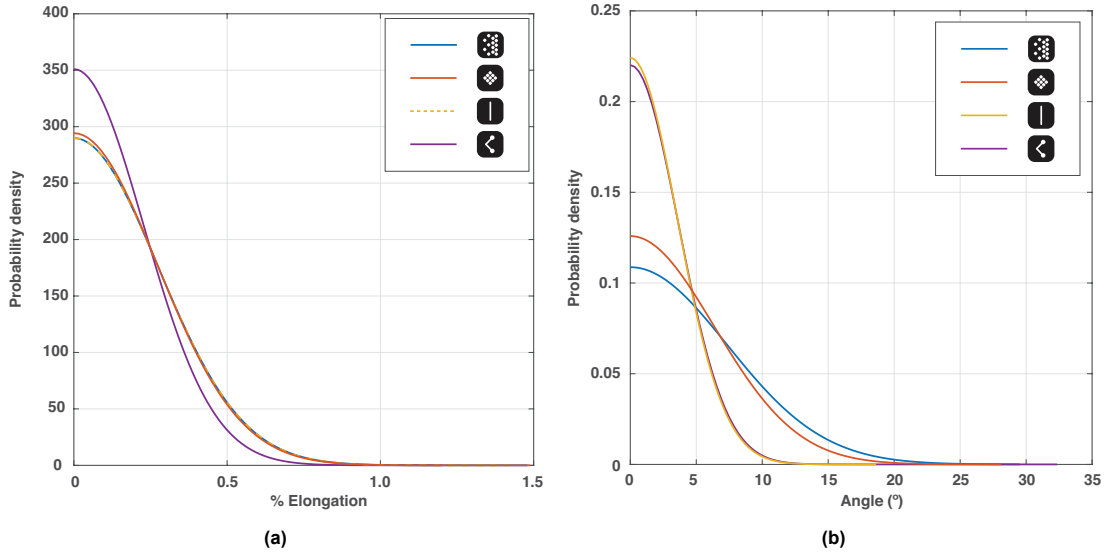

Figure 7.22: *Calculated half-normal distribution fit for beam elongations (left) and rotations (right) in hierarchical lattices.*

III

Discussion and Conclusions

8

Discussion: Uniform Relative Density

8.1. Introduction

One of the most, if not the most, important parameters in cellular material mechanical response is relative density. There is a growing body of knowledge in this field, though much of it remains at the lattice level and is the product of numerical methods. But ultimately, lattice behavior is determined by how individual nodes and ligaments deform in response to loading. The question naturally arises of whether a relationship can be identified which ties cell-level deformations to global lattice mechanical response, and, if so, how does relative density influence this relationship? Chapter 8 will explore these questions for the set of uniform relative density lattices, after which Chapter 9 will continue with a discussion on the hierarchical lattice results.

In investigating this potential link, the deformation behavior of individual cells will be examined. Though two cells rarely deform in the same way, three general deformation shapes can be seen in the experimental lattices, described below and visualized in Figure 8.1 to guide the reader and provide a point of reference.

- **Nodal hinging** This shape is characterized by nodes which appear to act as pin joints. Struts remain straight and rotate in towards the center of the unit cell.
- **S-bending** The nodes of s-bending cells act more like a fixed supports and allow little rotation. Coupled moments created by the nodes cause struts to bend in the characteristic ”S” shape with an inflection point in the center of the strut
- **U-bending** Similar to s-bending, nodes behave like fixed supports and allow little rotation. Opposite moments created by the nodes cause struts to bend in a u-shape with no inflection point

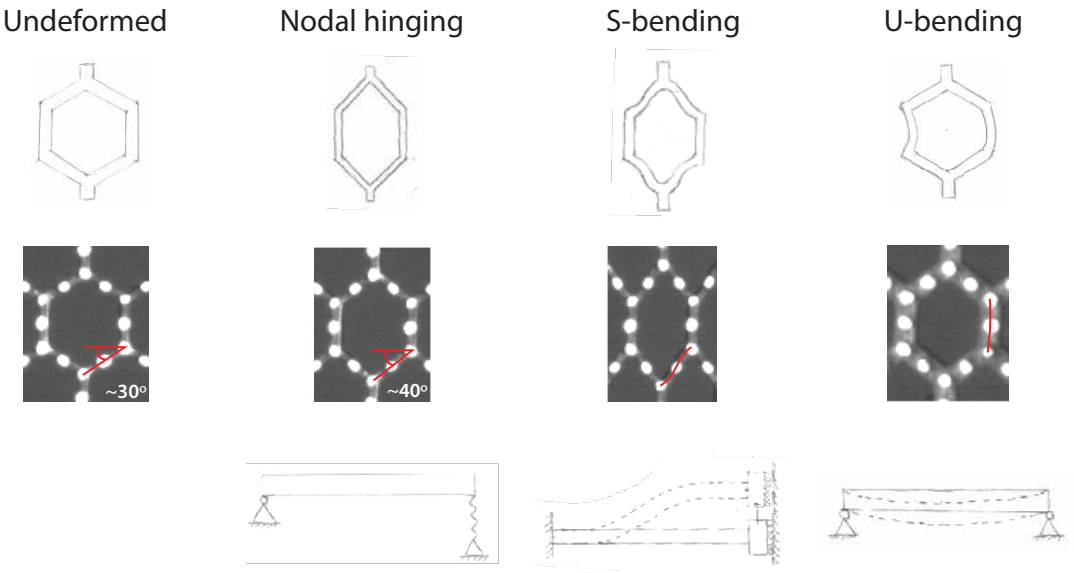

Figure 8.1: *Cell deformation shapes identified in experimental lattices*

8.2. Interpretation of results and observations

The remainder of this chapter focuses on the uniform relative density lattice results. Recalling Chapter 4, the research intent of this set of lattices is to establish a relationship between lattice mechanical response and relative density which can be compared to literature and the mechanical response of the hierarchical lattices which will discussed in Chapter 9. Guiding this intention is the first set of hypotheses presented in Chapter 4, recalled below for ease of reading.

The first two hypotheses focus on how the lattice-level responses compare to existing mechanical models in literature. The latter two hypotheses look more at the impact of relative density on how the lattice adapts to loading at the cell-level. Following from the results presented in Chapter 7, several observations can be made which will be discussed here in context of literature and these hypotheses.

1.1 Up to $\bar{\rho} = 0.2$, numerical models predicting lattice stiffness and lattice fracture toughness accurately describe mechanical response

1.2 Up to $\bar{\rho} = 0.2$, lattices exhibit a double-lobed butterfly crack tip deformation shape

1.3 Beyond lattice stiffness and lattice fracture toughness, mechanical response is not affected by relative density; a lattice made from a brittle base material will exhibit brittle tensile behavior at all relative densities

1.4 Relative density does not affect fracture path or observed toughening mechanisms; predominant toughening mechanisms are crack deflection and ligament bridging

Using parameters based on bulk properties to describe lattice behavior may not be adequate

The scaling law coefficients obtained from Equations 3.2 and 3.3 and presented in Figures 7.4 and 7.5 can be compared to literature. Figure 8.2 shows the experimental values plotted against the expected values from literature over the same range of relative densities.

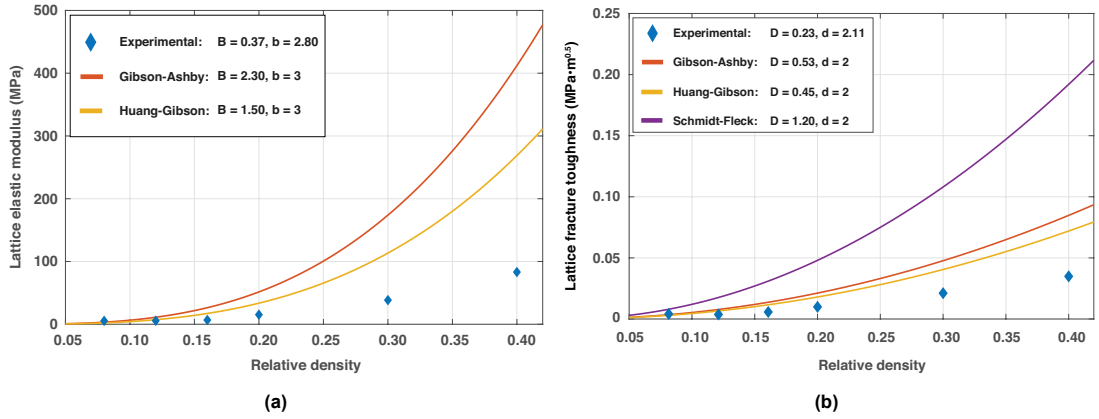

Figure 8.2: *Calculated experimental $\bar{E}$ (left) and $\bar{K}_{IC}$ (right) values compared to numerical predictions from literature*

For this comparison, the value of the exponential coefficient is of greater importance than the constant coefficient. The initial constant coefficient value must be divided by E_s or σ_{ts} for lattice elastic modulus and fracture toughness, respectively, making its value dependent on the chosen material properties which, as discussed in Chapter 5, are assumed to be correct. Therefore, any discrepancy in B and D between the experimental results and literature is likely related to material properties. That said, when the full range of $\bar{\rho}$ is considered, there is generally good agreement with literature for both lattice elastic modulus and lattice fracture toughness for the exponential coefficients, as b only varies by 6.8% and d by 5.6%, suggesting that despite differences in base material properties, these coefficients are primarily linked with cell topology.

To assess the validity of the assumption that results are valid when $\bar{\rho} < 0.20$, the scaling law coefficients are recalculated for the sets $0.08 < \bar{\rho} < 0.20$ and $0.20 < \bar{\rho} < 0.40$ and presented in Table 8.1. For both parameters, interestingly, the coefficients obtained in the high-density lattice set align more closely with literature than the low-density set. This difference could arise from a lack of printing

Table 8.1: *Scaling law coefficients for lattice elastic modulus and fracture toughness broken down by low- and high-density*

	$\bar{E}$		$\bar{K}_{IC}$	
	B	b	D	d
Full	0.373	2.796	0.23	2.11
$0.08 \leq \bar{\rho} \leq 0.2$	1.53	3.491	1.31	2.56
$0.12 \leq \bar{\rho} \geq 0.2$	-	-	0.838	2.91
$0.20 \leq \bar{\rho} \leq 0.40$	0.323	2.618	0.57	1.99

precision at low relative densities, which possibly misrepresented the true relative density in sub-0.20 lattices. Given that the actual mass and $\bar{K}_{IC}$ for $\bar{\rho} = 0.08$ and 0.12 is quite similar. If $\bar{\rho} = 0.08$ was causing problems, one would then expect the coefficients to align more closely with literature when it is omitted from the curve fitting; however, this is not the case.

This leaves the evidence supporting Hypothesis 1.1 is, therefore, somewhat confusing. Over a wide range of relative densities which includes $\bar{\rho} > 0.20$, the scaling laws seem to accurately describe lattice behavior, but the relation breaks down when only $\bar{\rho} \leq 0.20$ lattices are considered. Another possibility lies with the scaling law itself, that it is developed based on a solid continuum. This would cause the relation to more accurately describe lattices which behave more like a continuous medium, in this case the high-density lattices This raises further questions about, a) how representative these lattices are with respect to an ideal lattice, and b) whether $\bar{K}_{IC}$ is a suitable parameter for describing lattice behavior.

Relative density affects how cell deformations concentrate and manifest within a lattice
Evidence presented in Figures 7.9, 7.10 and time-lapse videos of the deformation fields demonstrate the effects of relative density has on how deformations develop during loading. An interesting observation is that the rotation field of low-density lattices early in loading look similar to that of a high-density lattice at failure, illustrated in a side-by-side comparison in Figure 8.3. This trend is observed at all relative densities; all lattices exhibit similar deformation behavior initially, but as loading continues, the compliant, low-density lattice deformations continue developing, wile high-density lattices simply fracture.

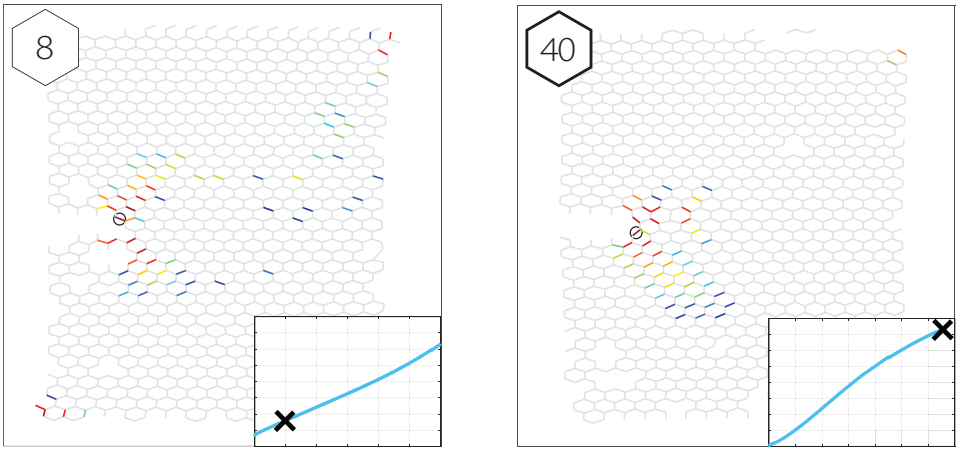

Figure 8.3: *Rotation deformation fields for $\bar{\rho} = 0.08$ near the beginning of loading (left) and 0.40 just prior to final fracture (right).*

Another observation that can be made in the deformation fields relates to Hypothesis 1.2. In Figure 7.10a, a vague double-lobed butterfly contour can be seen, similar to the contour of the plastic zone seen in Chapter 3. Figure 8.4 shows one of the rotation deformation fields with this profile highlighted with the plastic zone prediction by Tankasala et al. for comparison. The similarity not only corroborates Hypothesis 1.2, but provides evidence that the deformation field at the crack tip could be seen as analogous to a plastic zone, even though plasticity has not been measured.

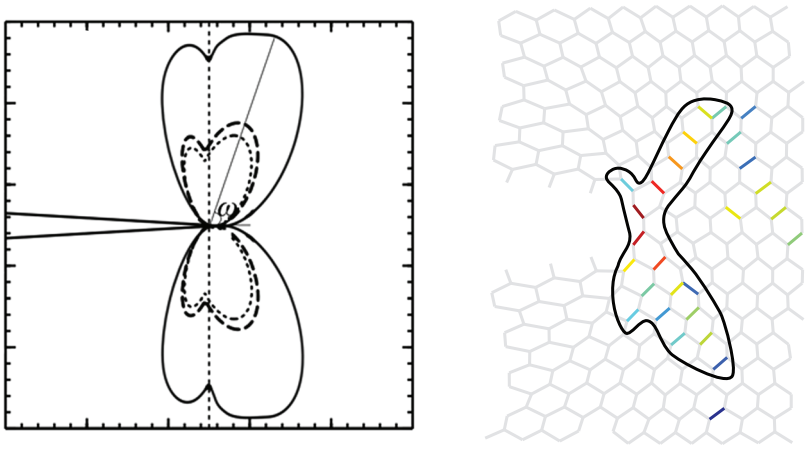

Figure 8.4: *Comparison of shape of crack tip plastic zone predicted by Tankasala et al. (left, adapted from [11]) and the rotation deformation field for Specimen 08_02 (right)*

Brittle base material does not necessarily mean brittle response
Both lattice-level results and cell-level observations seem to provide evidence that, despite having the same base material, relative density significantly impacts mechanical response. As the base material is considered to be a brittle polymer, Hypothesis 1.3 predicts that the stress-strain response and fracture behavior will be brittle. Disregarding the differences in mechanical response after $\bar{\rho} = 0.20$, the low-density lattice force-displacement and stiffness-displacement behavior seen in Figures 7.1 and 7.3 seem to contradict this hypothesis, as these appear to be more elastomeric than brittle. The force-displacement and stiffness-displacement behavior of the $\bar{\rho} = 0.40$ lattices, by contrast, suggests a more brittle response. Even more interesting is the stiffness response of the $\bar{\rho} = 0.20$ and 0.30 lattices, which appear to have elements of both stiffness responses. The stark contrast in fracture pattern, seen in Figure 7.8 and the explosive nature of high-density lattices, also attests to the effect of relative density on lattice behavior. Based on these observations, Hypothesis 1.3 cannot be validated.

Relative density affects fracture path and toughening mechanisms present
To confirm Hypothesis 1.4, the fracture behavior of the uniform lattices should remain relatively consistent. And while the exact fracture paths are unique to each lattice, there are noticeable differences between relative densities which serve to invalidate Hypothesis 1.4:

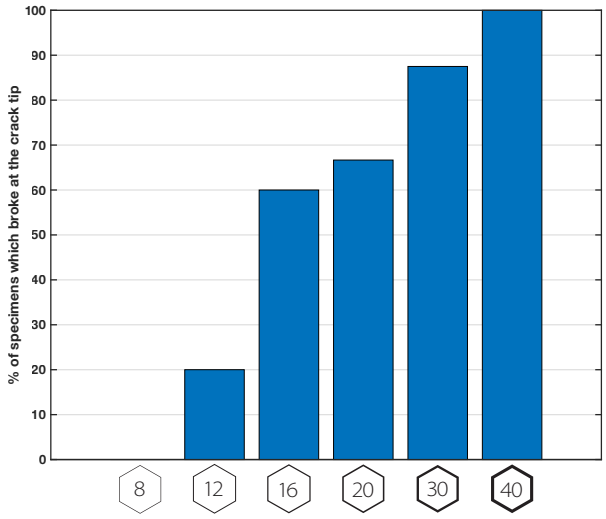

Figure 8.5: *Percentage of tested lattices which broke at the existing crack tip per uniform relative density set*

- **Variation**

At low relative densities, there is significant variation in where cracks form and the paths tend to be quite erratic. The number of lattices which broke at the existing crack tip increases with relative density and path variability decreases, shown in Figure 8.5. Additionally, several low-density lattices fractured at the interface between the lattice and slider bar, indicating that the intended stress concentration at the existing crack tip was not sufficient to force fracture to initiate there. This correlates somewhat with particularly the rotation deformation fields of Figure 7.10, which show large rotations radiating from the corners. Neither the deformation concentration locations, nor the location of the most-rotated strut, however, were necessarily predictive of failure location.

- **Intermediate fracture**
  Small load drops occur frequently at every relative density, corroborated by Figures 7.1 and 7.8, but their nature seems to change with relative density. Intermediate fractures appear more dispersed in the lattice at low relative densities, while they are almost exclusively located near the crack tip at high relative densities.

- **"Exit-lane-ing"**
  A phenomenon seen almost exclusively in $\bar{\rho} < 0.20$ lattices is a form of crack branching, which will be termed here as "exit lane-ing". "Exit lane-ing" is similar to crack branching; the crack splits into two paths to help dissipate energy, but instead of the symmetrical split typically associated with crack branching, one branch continues to propagate without changing direction and the other branch is an offshoot which turns sharply towards the applied load, the "exit lane". This phenomenon is illustrated in the fracture path of Specimen 16_01 in Figure 7.8.

- **Crack deflection**
  Large crack deflections occur almost exclusively in $\bar{\rho} < 0.30$ lattices. Some crack deflection occurs at high relative densities, but the deviations are small and typically rejoin after a few cells. This is evidenced by closer inspection of the high-speed images for a $\bar{\rho} = 0.40$ lattice, where a cluster of cells remains in focus while the surrounding lattice is out-of-focus and two cracks form around the cluster.

8.3. Three distinct responses

In synthesizing the results and observations, a deficiency in the hypotheses emerges. Lattice- and cell-level behaviors are addressed individually, and there clearly is a relationship between relative density and mechanical response at each level. At the lattice-level, this can be most clearly seen in how the stiffness curves take form throughout loading. At the cell-level, differences arise in how deformations concentrate and how fracture propagates in the lattice. The hypotheses, however, do not go far enough to sufficiently explain the connection between the two levels. The missing link is an understanding how cell-level behaviors manifest themselves at the lattice-level. To explore the connection between lattice- and cell-level behaviors, cell deformation behavior, including individual cell deformations and the deformation fields, will be examined at various points of interest during loading and correlated with the stiffness-displacement curves.

Based on the stiffness curves in Figure 7.3, three unique profiles can be identified: elastoplastic ($\bar{\rho} = 0.40$), elastomeric ($\bar{\rho} = 0.08, 0.12, 0.16$), and hybrid ($\bar{\rho} = 0.20, 0.30$). In the following subsections, each profile will be analyzed, correlating stiffness with cell deformations and deformation field behavior at various points of interest. Each response is accompanied by a figure showing:

1. The stiffness-relative displacement curve for a representative lattice exhibiting that stiffness response with points of interest marked by a dot and a number;

2. An image of a selected set of cells corresponding to each point of interest, and;

3. A schematic representation of the lattice showing the location of the highlighted cells

A written summary of the deformation field and cell deformation behaviors corresponds with the point(s) of interest. Videos of the deformation field progression for each type can be downloaded here.

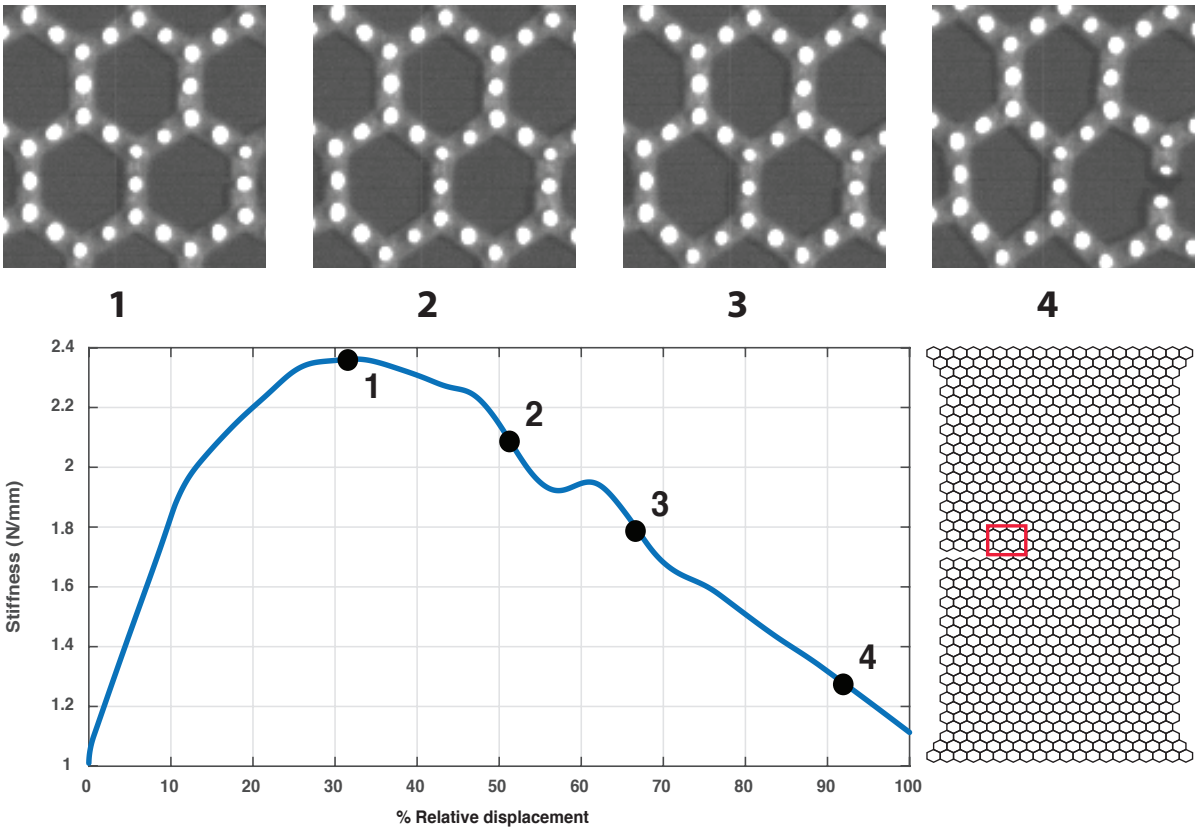

Figure 8.6: *Stiffness curve for $\bar{\rho} = 0.40$ lattice with highlighted points of interest and corresponding cell deformation behavior*

8.3.1. Elastoplastic

The elastoplastic response is seen exclusively in $\bar{\rho} = 0.40$ lattices, and is characterized by settling period followed by a brief LE plateau, after which strain softening occurs up to failure.

1 Linear-elastic regime
Up to this point, both the elongation and rotation deformation fields are almost exclusively noise as the deformations are still very small. At the end of the settling period, large elongation and rotation concentrations begin to form at the crack tip. At the end of the LE regime, the largest elongations shift from occurring in vertical struts to the inclined struts. Cell deformation is minimal; however, struts remain unbent and nodal hinging is likely occurring here.

2 Initial lattice strain softening
This period is marked by several changes in the lattice. Initially, the rotation deformation concentration appears to be two amorphous lobes above and below the crack tip and is often very asymmetrical. As strain softening continues, this asymmetry balances out and continues to do so until failure. Throughout, the elongation deformation concentration increases in size.

Around the midpoint of this regime, several beams begin to exhibit slight s-bending. Close to the crack tip, some beams exhibit u-bending, seemingly due to high stresses caused by rotation in the struts at the crack tip to the left and the stiffness of the rest of the lattice to the right.

3-4 Change in lattice strain softening rate
Most of the changes observed in this regime are seen in the test images. S-bending can be seen, even if vaguely, in most of the lattice, suggesting that the change in stiffness rate is the result of all nodes reaching their maximum rotation and, therefore, stiffness. Intermediate fracture, if it occurs, occurs during this period, though it does not appear to induce strain softening behavior.

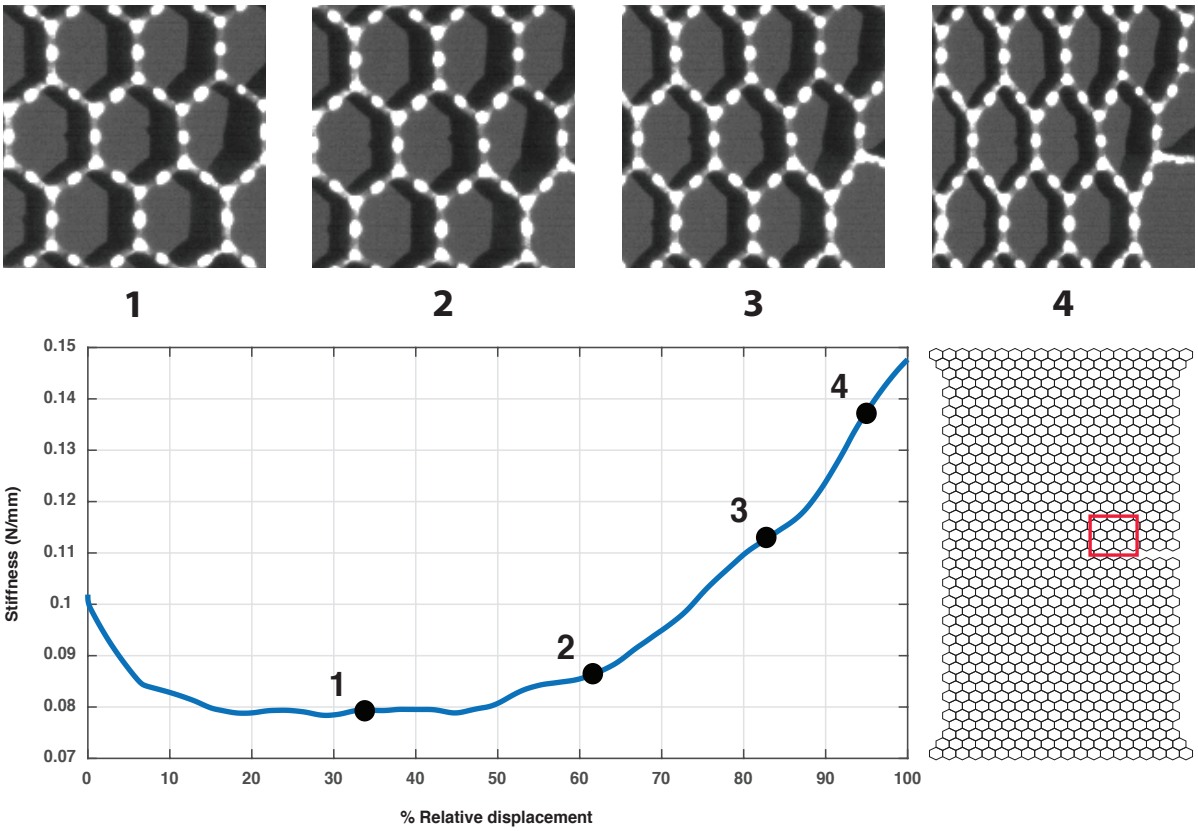

Figure 8.7: *Stiffness curve for $\bar{\rho} = 0.12$ lattice with highlighted points of interest and corresponding cell deformation behavior*

8.3.2. Elastomeric

The elastomeric response is characteristic of lattices with $0.08 \leq \bar{\rho} \leq 0.16$. Its profile is quite different from the elastoplastic response, exhibiting a long LE regime which gives way to lattice strain stiffening up to fracture.

1 Linear-elastic regime
Several phenomena are visible during the long LE regime in low-density lattices. Deformation is characterized by nodal hinging in virtually every cell. Vertical bands opposite the crack tip form initially in the elongation deformation field, but gradually shift towards the crack tip as the LE behavior continues. At the onset, the rotation deformation field looks very similar to that of elastoplastic-type lattices, two large, amorphous lobes extending above or below the crack tip; this rotation concentration typically grows slightly during this period.

2-3 Lattice strain hardening
The rotation concentration at the crack tip begins to shrink and form the characteristic double-lobed butterfly shape. The highest-rotated strut is now consistently immediately ahead of the crack tip. Most of the largest elongations are concentrated near the crack tip, if not at it, though the highest-elongated beam often fluctuates. S-bending begins to appear, but is very sporadic and confined to specific areas, particularly in the corners or center of the lattice.

4 Linear lattice strain hardening
The last microcrack marks the start of the final stiffness regime, which is characterized by a sharp increase in lattice strain hardening which continues up to failure. At this point, the shape and size of elongation and rotation concentrations do not change much; however, if the largest rotation moves away from the crack tip, it will do so during this period. The predominant cell deformation begins to shift from nodal hinging to s-bending, though still not all struts show s-bending just before final failure.

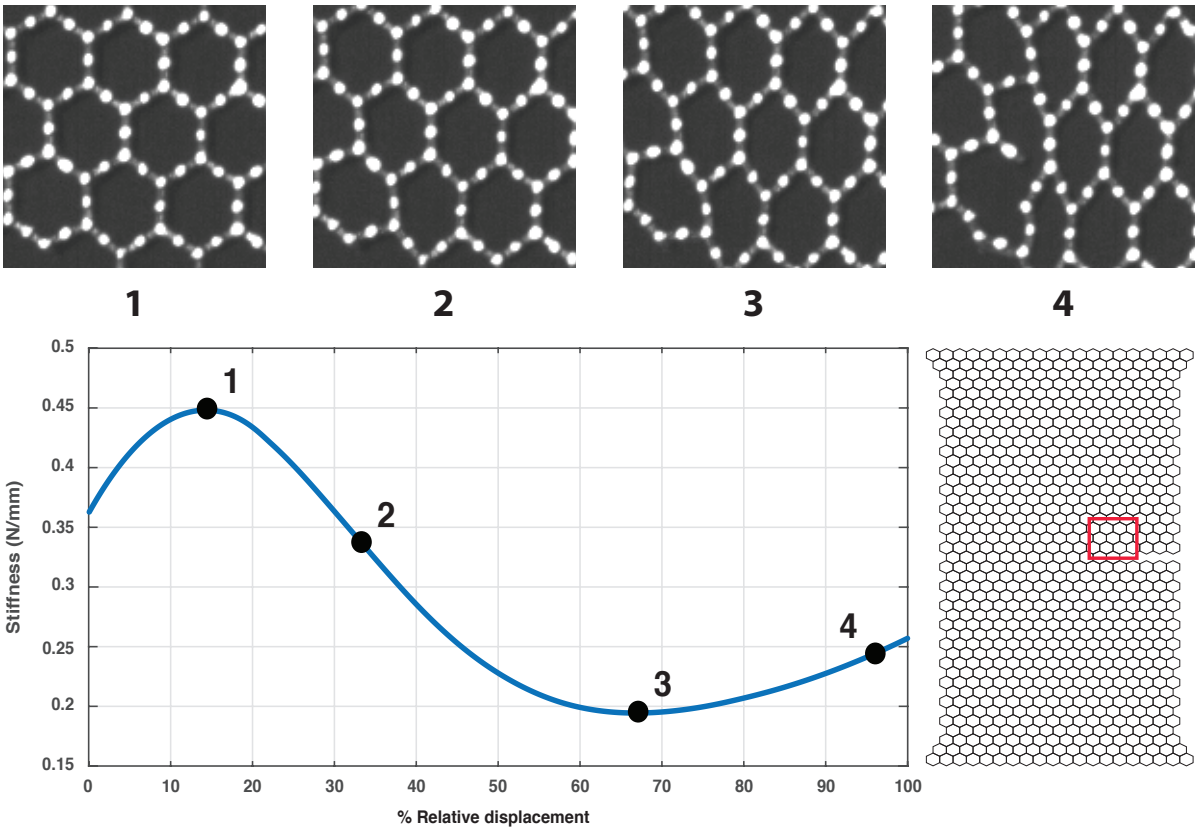

Figure 8.8: *Stiffness curve for $\bar{\rho} = 0.20$ lattice with highlighted points of interest and corresponding cell deformation behavior*

8.3.3. Hybrid

Lattices with $\bar{\rho} = 0.20$ and 0.30 exhibit an interesting stiffness response that could be seen as a hybrid of the elastoplastic and elastomeric responses. These lattices experience the initial strain softening behavior commonly seen in elastoplastic-type lattices before reaching a minimum and subsequently experience a slight elastomeric-like strain stiffening up to failure.

1 Initial plateau
The elongation deformation field is very noisy throughout this period, though more vertical struts appear to be contributing to 90% of the total elongation. Very little, if any, cell deformation is visible.

2 Loss of stiffness
The 30°struts appear to begin hinging at the nodes. This correlates with a rotation concentration beginning to take shape during stiffness loss, which increases in size over this regime. The elongation deformation field continues to be very noisy, though there is a noticeable shift in the largest values from the vertical struts to 30°struts.

3 Bottom of bathtub curve
The largest elongations shift to concentrate at the crack tip, though there is still significant noise. Several cells begin to show s-bending and the rotation concentration at the crack tip stops growing.

4 Stiffness increase to failure
Struts have reached their maximum rotation angle and begin to elongate up to failure. The rotation concentration at the crack tip shrinks, the extent depending on the length of this regime. Nearly all large elongations have concentrated at the crack tip.

8.4. Discussion on stiffness curve classification

Lattice mechanical response is the result of complex cell-level interactions, making it difficult to neatly categorize all behavior in relation to relative density. Using lattice stiffness as a base for categorization is one of many possible methods, but it is by no means all-encompassing. Consequently, some ambiguity remains in this categorization as lattices may not always fit into these defined boxes. This section explores some of these ambiguities and contradictions to provide a more robust picture of the intricate cell-lattice relationship.

Deformation in $\bar{\rho} = 0.08$

At first glance, s-bending appears to occur in several beams in $\bar{\rho} = 0.08$ lattices, but comparing the first and final images shows that many of these beams were, in fact, warped prior to testing and did not straighten out during loading. If the nodes were able to impart any strength or stiffness on its connected struts, it would be expected that some of the warped struts would have straightened at least partly. This suggests these nodes were much more compliant than those in the other low-density lattices and allowed virtually free rotation up to failure. Fracture often occurred at the corners where several adjoining struts had almost become completely aligned, shown in Figure 8.9, implying that beams here were stretched, not bent, to failure. By contrast, $\bar{\rho} = 0.12$ and 0.16 lattices displayed more consistent s-bending behavior towards failure, suggesting that the failure mechanism of $\bar{\rho} = 0.08$ here may be different from other low-density lattices.

Beam elongation/rotation distribution

If the stiffness classification would be applied to Figures 7.11, it would be expected that the deformation distributions would fall into three groupings, but this is not the case. Instead, the elongation distribution shows a clear groupings between elastomeric- and hybrid/elastoplastic-type lattices. In the rotation fields, however, $\bar{\rho} = 0.20$ joins the elastomeric-type lattices, lending plausibility to the hypothesis that $\bar{\rho} = 0.20$ represents a transition point, as elongations and rotations are both relatively evenly-spaced rather than having a predominant deformation mechanism.

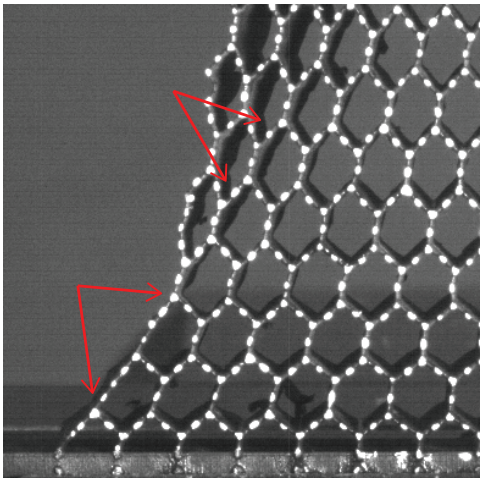

Figure 8.9: *Example of inclined struts aligning at the lower-left corner of Specimen 08_02*

Role of intermediate fracture

Lattice fracture paths, including intermediate fracture, are influenced by relative density, but these patterns do not always align with the stiffness profile division.

Microcracking is common in elastomeric-type lattices and occurs exclusively in the lattice strain stiffening regime. The location of these intermediate fractures appears to be random and are typically not near the existing crack tip. Just prior to an intermediate fracture, the deformation fields typically yield little insight into which beams will fail. As struts fail prematurely, lattice stiffness typically increases, behavior which is consistent with the expected effects of microcracking.

As relative density increases, microcracking is no longer directly associated with lattice stiffening, though there are still differences between relative densities. For example, there is a noticeable decrease in number of intermediate fractures between $\bar{\rho} = 0.20$ and 0.30 lattices. Despite both having the hybrid-type stiffness profile, the fracture behavior of $\bar{\rho} = 0.30$ lattices seems to align more with elastoplastic-type lattices, while $\bar{\rho} = 0.20$ lattices exhibit random fracturing similar to elastomeric-type lattices, microcracking in $\bar{\rho} = 0.30$ and $\bar{\rho} = 0.40$ lattices is typically confined to the region immediately surrounding the crack tip.

These differences point to a possible explanation on the purpose of intermediate fracture at different relative densities. In lattices with $\bar{\rho} \leq 0.20$, microcracking seems to be associated with fault-tolerance, as weaker beams are sacrificed early in loading when the strain energy is low and premature failure is not catastrophic. Intermediate fracture in $\bar{\rho} = 0.30$ and 0.40 lattices and appear to be more related to the ligament bridging where the crack ”jumps” across cell wall boundaries and do not contribute to changes in lattice strain behavior.

Final fracture path
Within the elastomeric-type and elastoplastic-type lattice, the final fracture paths are internally consistent; the former is characterized by random fracture patterns with large deflections, while lattices in the latter fracture more consistently straight across the structure. The hybrid group is split, however, with $\bar{\rho} = 0.20$ lattices aligning more with the elastomeric-type lattices with large crack deflections and $\bar{\rho} = 0.30$ lattices fracturing more similarly to the elastoplastic group. Combined with observations on the toughening mechanisms described above, this provides more evidence that the hybrid response category does, in fact, represent some kind of transition point in lattice mechanical response.

8.5. Summary

This chapter has put forth a discussion on the experimental results of the set of uniform relative density lattices. This discussion initially centered around four hypotheses that were formulated in relation to how relative density impacts lattice-level and cell-level behaviors. How cell-level deformations manifest themselves at the lattice-level, however, is not sufficiently addressed by the hypotheses.

An investigation into the relationship between cell deformation behavior and stiffness response curves constitutes a first step in establishing an experimental link. Three general profiles for the stiffness curves have been identified and correlate with relative density. Irrespective of stiffness curve profile, all lattices deform first by nodal hinging followed by s-bending. This is contrary to Gibson and Ashby's prediction that s-bending occurs first, followed by nodal hinging in polymer-based lattices [7]. Changes in stiffness response can also be identified in the elongation and rotation deformation fields.

Furthermore, although using the stiffness curves as a basis for correlating lattice- and cell-level behavior is useful, it is not an airtight classification, and a number of contradictions and ambiguities remain. Two observations, in particular, are worth highlighting:

- Similarities in stiffness behavior, but differences in fracture pattern and distribution of deformations in $\bar{\rho} = 0.20$ and 0.30 lattices suggest that these lattices should not be grouped together. It does suggest, however, that these lattices likely represent a transition point in lattice mechanical response and that this point may be different for cell- and lattice-level behaviors.
- Lattices in the elastomeric grouping had remarkably similar lattice-level behavior, but $\bar{\rho} = 0.08$ lattices differed from the rest of the grouping in cell deformation behavior, in particular.

A more-robust approach is needed to further strengthen the link between cell deformations and lattice behavior. This includes a quantitative study of beam deformation behavior by using five dots per beam instead of three. In doing so, the onset of nodal hinging and s-bending can be quantified in relation to the stiffness response, and the internal moments and shear forces, and subsequently stresses, can be calculated, providing the stress state at any given location in the lattice.

9

Discussion: Hierarchical Lattices

The second set of lattices, the hierarchical lattices, builds on the previous set by taking a uniform lattice and adding structural hierarchy in the form of local variations in relative density. The research intention was to evaluate lattice mechanical response in terms of the lattice- and cell-level behavior and relate differences between the two sets to the implementation of structural hierarchy.

This chapter is divided into two main sections. First, results and observations from Chapter 7 are gathered and discussed using the second set of hypotheses set forth in Chapter 4 as a guide, as well as results from the uniform relative density set. The second section applies the stiffness curve-cell deformation analysis proposed in Section 8.3 to highlight how different structural hierarchy elements interact with each other to influence lattice mechanical response.

9.1. Interpretation of results and observations

The addition of structural hierarchy by means of relative density affects several aspects of lattice mechanical response. Results and observations at both the lattice- and cell-level, presented in Chapter 7, provide corroborating evidence and will be discussed here. The second set of hypotheses will be used to guide this section and are recalled below. Following the structure of the hypotheses, some general remarks will first be made on the set of all hierarchical lattices, followed by a closer look at the behaviors seen in each hierarchical configuration (i.e. compliant/stiff or stiff/compliant).

2.1 The predominant material phase (stiff or compliant) drives overall differences between hierarchical and uniform lattices; differences between lattices of the same predominant material phase are attributed to cell-level responses

2.2 Compliant/stiff configurations

- 2.2a The presence of stiff inclusions result in a higher lattice stiffness compared to an equivalent uniform lattice
- 2.2b The crack tip deformation field shifts to wrap around stiff inclusions, but still retain the double-lobed butterfly shape
- 2.2c The primary toughening mechanism is crack deflection caused by the inclusions
- 2.2d A cluster of inclusions forces cracks to take a tortuous path, while functionally-graded inclusions do not initially impede crack growth, but force a tortuous path as fracture progresses

2.3 Stiff/compliant configurations

- 2.3a Removing material in the form of weak channels will promote crack growth and result in a consistent fracture pattern; fracture is arrested by a stiff phase at the end of the channels
- 2.3b A consequence of removing material is slightly lower lattice stiffness and lattice fracture toughness
- 2.3c Deformation concentrations are primarily observed in the weakened regions

9.1.1. All configurations

Lattice-level response is grouped by hierarchical configuration
Figure 7.15 provides the most clear evidence that the overall mechanical response of hierarchical lattices is driven by the dominant phase (compliant or stiff), corroborating Hypothesis 2.1. Variation in the compliant/stiff lattices in the force-displacement curves is likely the result of specific topology and will be addressed in the next section. That said, the general trend holds that these lattices behave fairly similarly. The stiff/compliant lattices show remarkably similar behavior, a trend that is visible in the full set of hierarchical lattices. This categorization by dominant phase is also evident in Figure 7.17. Like the force-displacement behavior, $\bar{E}$ and $\bar{K}_{IC}$ generally group by hierarchical configuration, but show differences between specific topologies.

The stiffness curves in Figure 7.14 generally support Hypothesis 2.1, but the influence of specific topology becomes more evident. In Figure 9.1, one can see the uniqueness of each hierarchical lattice stiffness response. Comparing these to the elastomeric and hybrid profiles the hierarchical response, for the most part, do not show any obvious similarity, highlighting the influence of hierarchy.

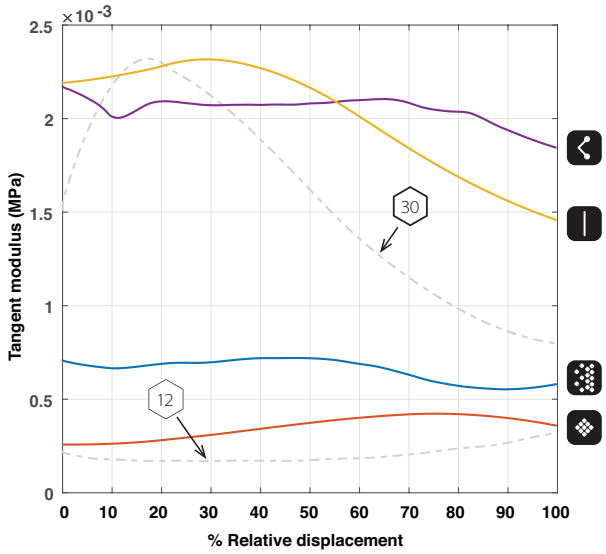

Figure 9.1: *Hierarchical stiffness curves with those of $\bar{\rho} = 0.12$ and 0.30 for comparison*

9.1.2. Compliant/stiff

Stiff inclusions in a compliant lattice likely contribute to an increase in lattice elastic modulus
Average $\bar{E}$ values obtained for the Bamboo and Nacre lattices can be compared to that of the average $\bar{E}$ for the $\bar{\rho} = 0.12$ uniform lattices, shown in Figure 9.2a. Both lattices show a statistically significant increase in $\bar{E}$ over the $\bar{\rho} = 0.12$ lattice, particularly when considering the equivalent $\bar{\rho}$ for these lattices (0.134 and 0.122, respectively).

That said, because the lattice design changed slightly between the uniform and hierarchical sets, it is not possible to say with complete certainty that the increase is a result of the stiff inclusions. The magnitude of the increases, however, strongly suggest that the inclusions are a factor, tentatively corroborating Hypothesis 2.2a.

Inclusion location can eliminate a crack tip deformation concentration entirely
The elongation and deformation fields of Bamboo and Nacre lattices seen in Figures 7.19 and 7.20 clearly show the effects of structural hierarchy on lattice deformation. In both lattices, the largest deformations are diverted away from the stiff inclusions, producing very different deformation fields compared to those of the uniform lattices in Figures 7.9 and 7.10.

The Bamboo rotation deformation field, in particular, is a striking example. The sparsely-spaced inclusions on the left side appear to force the largest deformations to congregate in the compliant cells between them. As a result, the crack tip rotation concentration seen in uniform lattices is completely

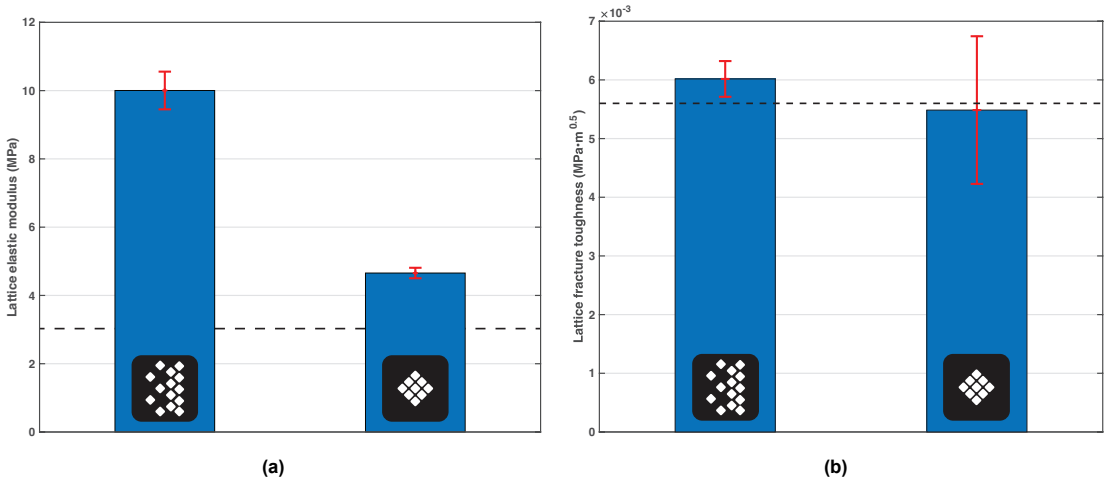

Figure 9.2: *Experimental hierarchical lattice elastic modulus values compared to experimental uniform values. Blue: hierarchical $\bar{E}$; red: standard error of mean; black: experimental $\bar{E}$ for similar uniform relative density lattice*

eliminated, invalidating Hypothesis 2.2b. Hierarchy also appears to consistently force the largest elongations to concentrate in the lower-right corner between the lowest inclusion and the start of the density gradient section, compared to the seemingly random patterns of elongation deformation in uniform lattices in Figure 7.9.

The Nacre rotation deformation field, however, does provide corroborating evidence for Hypothesis 2.2b, with the largest deformations pushed to the perimeter of the central diamond structure in a way that does not occur in low-density uniform lattices. In the elongation deformation fields, the inclusions also seem to prevent large deformations from forming within the central diamond structure, though their manifestation is less consistent than in the rotation deformation fields.

Inclusion location influences toughening mechanisms and fracture path

Similar to the deformation fields, the influence of structural hierarchy is evident in the observed toughening mechanisms and fracture paths of these lattices.

In all Bamboo and Nacre lattices, fracture occurred exclusively in the compliant phase. Cracks consistently deflected around the inclusions in all specimens, providing corroborating evidence for Hypothesis 2.2c. The Bamboo fracture path in Figure 7.18 best exemplifies this, as the crack path was successfully deflected several times around the inclusions, possibly contributing to the ”exit lane-ing” effect. No other identifiable toughening mechanism was observed in the Bamboo lattices.

In addition to crack deflection, other toughening mechanisms were observed in the Nacre lattices. All Nacre lattices experienced microcracking in a similar fashion to $\bar{\rho} = 0.08$ lattices. This makes sense, considering that the compliant regions were, like the $\bar{\rho} = 0.08$ lattices, often quite warped. The beams which fracture prematurely appear to be random. While this finding does not completely invalidate Hypothesis 2.2c, it does highlight the complexity of lattice fracture behavior in relation to structural hierarchy.

The fracture paths presented in Figure 7.18 add to this picture of complexity, particularly in the context of Hypothesis 2.2d. In Bamboo, the interaction between the inclusions and density gradient, which effectively prevented a stress concentration from forming at the existing crack tip, was not considered when designing the topology, thus making it impossible to evaluate Hypothesis 2.2d with the current data set. The fracture paths, however, show that fracture initiated in the same general location, highlighting the consistency that structural hierarchy could bring to lattice structures.

In Nacre, it was expected that fracture would initiate from the existing crack tip and taking a tortuous path through the central diamond structure via the $\bar{\rho} = 0.10$ beams which would remain compliant. Instead, the collective stiffness of this diamond effectively created one large inclusion which a crack would have to navigate around. Again, though this was not the intended effect, the fracture paths demonstrate that closely packing inclusions does not generally provide a path-of-least-resistance for a propagating crack, but that cracks can be deflected around a single large inclusion.

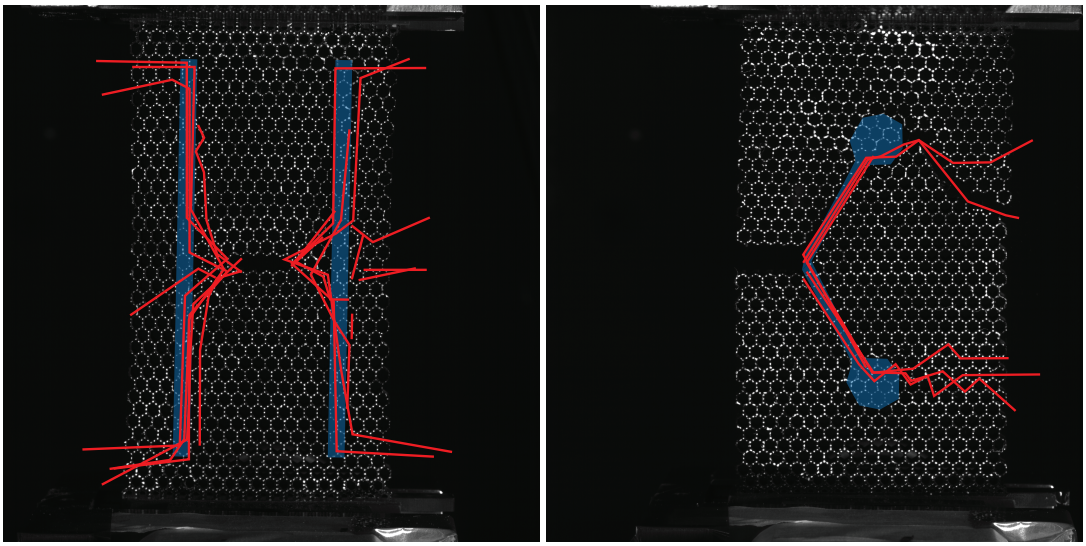

(a) (b)

Figure 9.3: *Composite images of all fracture paths of Glass Sponge (left) and Etching (right) lattices*

9.1.3. Stiff/compliant

Compliant channel promote a consistent fracture pattern, but do not help arrest fracture
All Glass Sponge and Etching lattices, save for G_02 [6], fractured entirely along the compliant channels, an observation most evidenced by overlaying the fracture paths of each lattice set, shown in Figure 9.3, thus confirming the first part of Hypothesis 2.3a.

Fracture was not arrested, however, invalidating the second part of Hypothesis 2.3a. In the Glass Sponge lattices, fracture propagates through the stiff phase towards the free edges of the lattice, often causing large sections of the lattice to break off. This is not an inherently bad outcome, however, as the crack path is diverted briefly by the compliant phase before continuing to propagate in the adjacent brittle phase, similar to the fracture behavior of glass sponges in nature. Therefore, this approach may still work in lattice structures, but testing with larger lattices with additional compliant lines would be needed to confirm this.

The compliant sinks in Etching lattices also did not arrest fracture. Instead, Figure 7.19 shows that large elongation concentrations formed at the edges of the sinks which could be considered analogous to stress concentrations. Consequently, these areas were likely more prone to overstressing and less able to withstand the sudden redistribution of strain energy at fracture.

Inclusion of compliant channels can influence lattice elastic modulus and fracture toughness
To assess the validity of Hypothesis 2.3b, $\bar{E}$ and $\bar{K}_{IC}$ are compared to those of uniform $\bar{\rho} = 0.30$, shown in Figures 9.4a and 9.4b, respectively. In general, the data suggests that introducing hierarchy has a negligible impact on $\bar{E}$, but a significant effect on $\bar{K}_{IC}$, partially supported Hypothesis 2.3b. Glass Sponge has a statistically similar $\bar{E}$ to the $\bar{\rho} = 0.30$ lattice. Etching, by contrast, experiences a slight (4.3%) drop in $\bar{E}$. $\bar{K}_{IC}$ is significantly lower than the uniform $\bar{K}_{IC}$, though the Glass Sponge lattices may have performed slightly better than the Etching lattices.

While the lattice-level evidence suggests that the compliant channels negatively affect fracture toughness, this must be balanced with fracture pattern predictability, a characteristic that is beneficial for damage tolerance. Thus, this finding provides an excellent example of the limitations of using $\bar{K}_{IC}$ as the sole means of determining lattice toughness and damage tolerance.

Inclusion of compliant channels influences deformation concentrations
The influence of the compliant channels is visible in the deformation fields in Figures 7.19 and 7.20. The observations do not necessarily always corroborate Hypothesis 2.2c, however, as there are substantial differences between the Glass Sponge and Etching lattices.

[6] For G_02, fracture initiated in the top-right corner of the lattice. This can be cautiously considered a statistical anomaly in the printing process; no visible defects can be observed where fracture initiated, nor is there any evidence to suggest early fracture in the deformation fields.

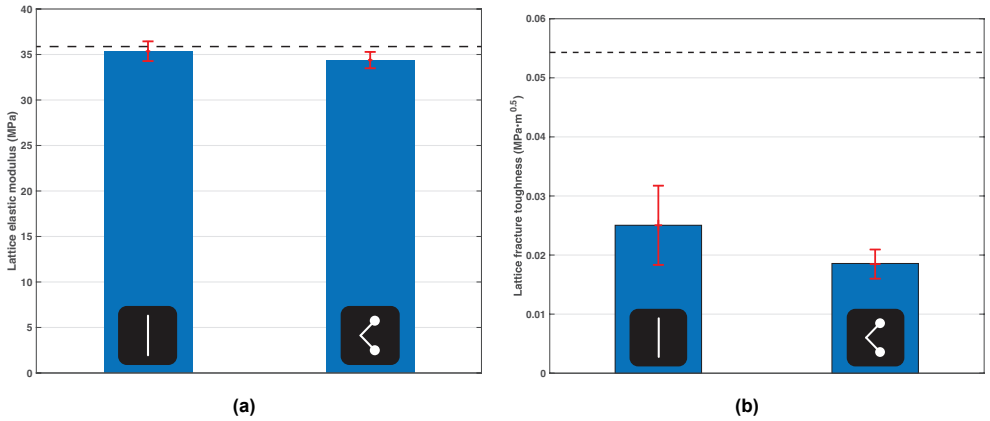

Figure 9.4: *Experimental hierarchical lattice elastic modulus values compared experimental uniform values. Blue: hierarchical $\bar{K}_{IC}$; red: standard error of mean; black: experimental $\bar{K}_{IC}$ for similar uniform relative density lattice*

The rotation deformation fields of Etching lattices show the largest rotations are consistently occurring exclusively within the compliant channels, confirming Hypothesis 2.3c. The elongation deformation concentrations, as discussed above, do not form in the sinks, but appear just to the right of them. This tangentially supports the hypothesis, as the deformation field is influenced by the sinks. Regardless, the presence of structural hierarchy invariably alters the deformation fields compared to a uniform lattice.

The Glass Sponge deformation fields also demonstrate the impact of structural hierarchy, but do not support Hypothesis 2.3c. A double-lobed butterfly shape can be observed in the rotation deformation field in Figure 7.20 which extends into, but not beyond, the weak channel. This contrasts the asymmetric, unwieldy blob seen in the uniform $\bar{\rho} = 0.30$ lattices in Figures 7.9 and 7.10. The largest elongations are generally confined to the area between the crack tip and the weak channels; a small elongation concentration near the lower-left corner lends plausibility to the idea that fracture continued past the weak channel due to overstressed beams after crack initiation. Even with the weak channels present, the highest elongations/rotations still occur at the crack tip; the weak channel deforms very little and is likely supported by the stiff surrounding structure.

9.2. Relating stiffness response to structural hierarchy

Implementing structural hierarchy using relative density has a striking effect on several aspects of lattice tensile response. The effects can be seen per hierarchical configuration (e.g. the high-level grouping of lattice elastic modulus for compliant/stiff vs. stiff/compliant lattices) and in the specific topology (e.g. the remarkable contrast between the deformation fields of the Bamboo and Nacre lattices).

In order to better understand the effects of specific topology in hierarchical lattices, a link should be established between the cell- and lattice-level responses. The unique stiffness curve profiles of each hierarchical lattice, shown in Figure 9.1, provide an interesting basis for exploring this link. Using the same techniques applied in Section 8.3, the stiffness behavior of the hierarchical lattices can be related to individual cell deformations. This section will examine each hierarchical lattice, correlating stiffness with cell deformations and deformation field behavior at various points of interest. The format of each subsection follows that of Section 8.3, consisting of a written summary of the deformation field and cell deformation behaviors with corresponding figures. Videos of the deformation field progression are provided in the form of a link in each subsection.

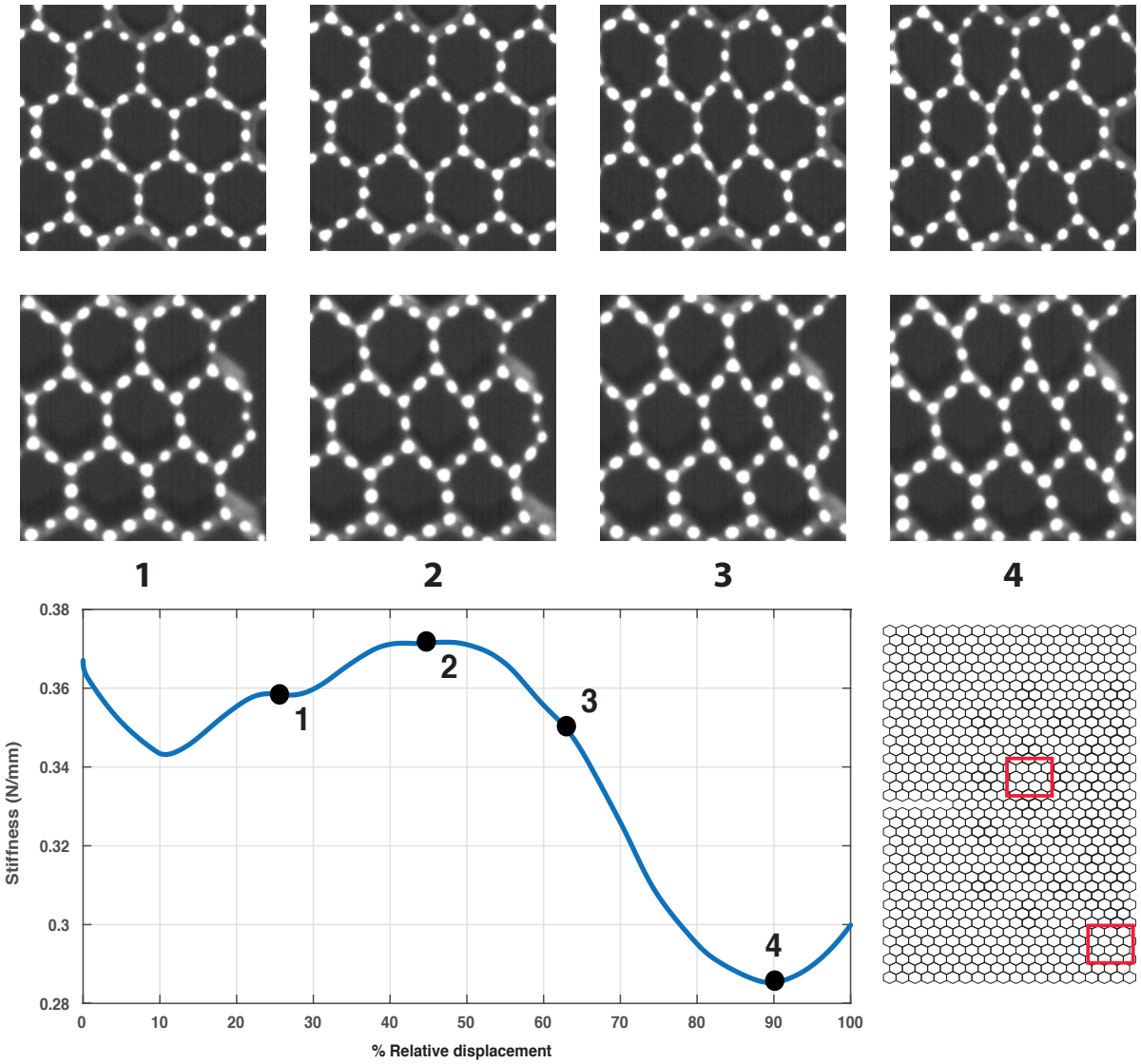

Figure 9.5: *Stiffness curve for a Bamboo lattice with highlighted points of interest and corresponding cell deformation behavior*

9.2.1. Bamboo

The stiffness behavior of Bamboo has similarities to the hybrid stiffness profile, but there are distinguishing elements. The first area of interest is a compliant cell sandwiched between two stiff inclusions, as virtually all large rotations are seen here, rotations which are higher than those seen in any uniform lattice. A second area of interest is also examined, located where fracture often initiated, at the lower-right of the lattice where the stiff inclusions end and the density gradient begins.

1 Stepped stiffening
The predominant cell deformation mechanism is nodal hinging in the compliant phase. The two distinct stiffening sections are associated with s-bending beginning in the cells in between the first and second inclusion columns. The stiff cells translate during this regime, but do not show signs of deformation.

2-3 Plateau and softening
As softening begins, the compliant cells between inclusions are almost entirely in s-bending as the stiff phase begins to take up more loading and hinging. The stiff phase also provides strength to support the continued deformation in the compliant cell walls.

4 Second stiffening
In the final stiffening period, the elongation deformation field shows nearly all large elongations concentrated in the lower-right corner. At the same time, no discernible cell deformation can be seen in this region; likely the cells have deformed to their limits and begin to stretch to failure. This is corroborated by the catalyzing fracture seen in the high-speed images. The cells sandwiched between stiff inclusions continue to rotate up to failure.

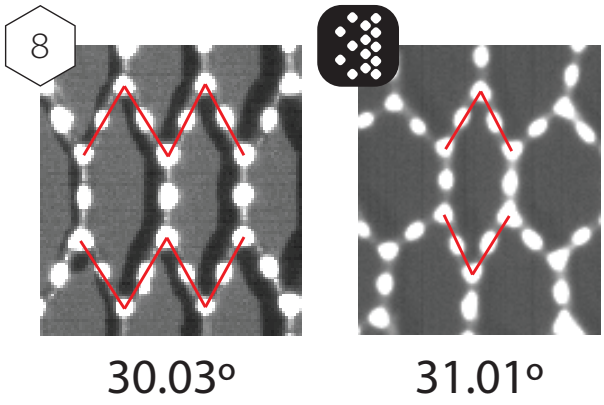

Figure 9.6: *Cells used to calculate average strut rotation for a $\bar{\rho} = 0.08$ (left) and Bamboo (right) lattice with average strut rotation indicated underneath each image.*

In addition to looking at the general cell deformation shape, the rotation angle of the struts bounded by the stiff inclusions can be compared to strut rotations in uniform lattices. This can be done by drawing a line between two nodes using Adobe Illustrator in the lattices of interest. Figure 9.6 shows the results of this process, which suggests that the Bamboo struts are able to rotate further than their uniform counterparts without failing. If true, this raises further questions about why these struts in particular are able to withstand further rotation. One hypothesis is that the inclusions impart some amount of stiffness, even remotely, which supports the compliant cells as they continue to rotate. Further testing would be needed, however, to quantify these effects and understand why this phenomenon occurs.

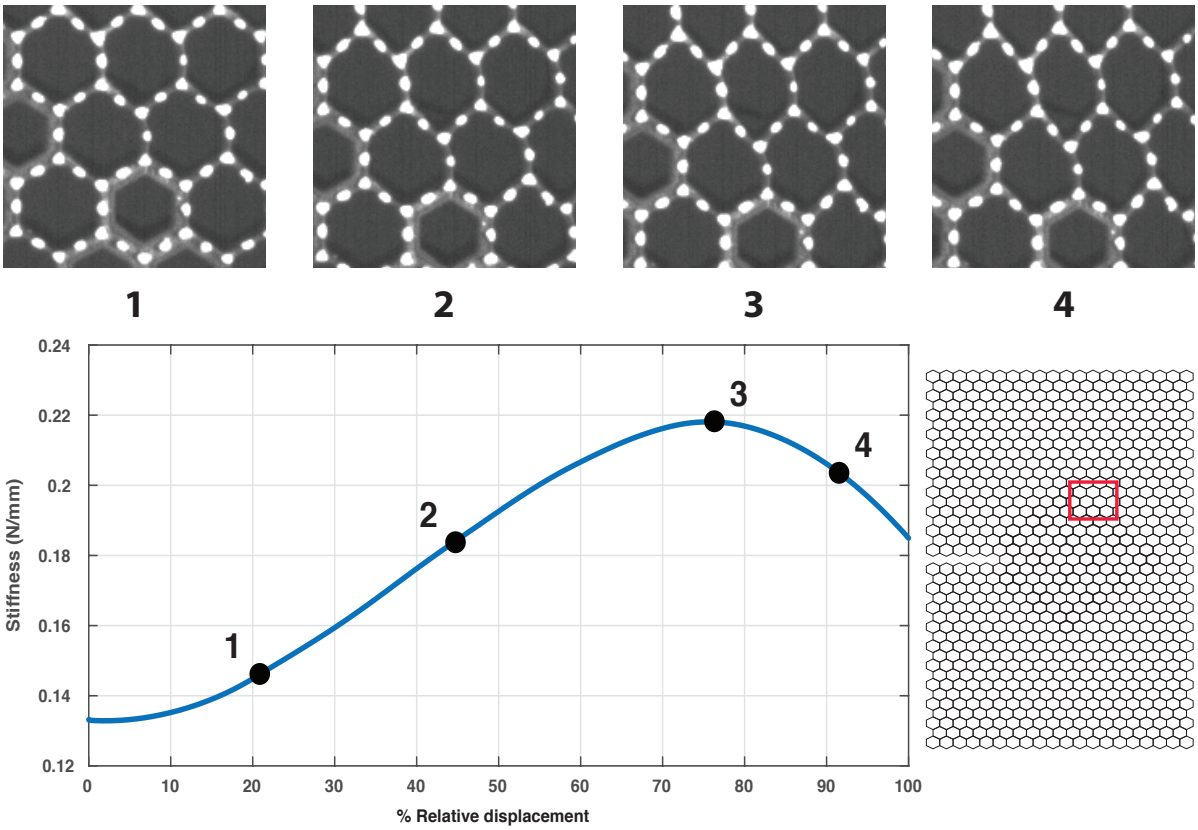

Figure 9.7: *Stiffness curve for a Nacre lattice with highlighted points of interest and corresponding cell deformation behavior*

9.2.2. Nacre

The stiffness curve of Nacre is particularly interesting, shown in Figure 9.7, as it is effectively a mirror image of the hybrid response. Video taken during testing, which can be viewed here, shows excessive deformation beginning almost immediately in the compliant region surrounding the diamond super-structure. Therefore, of interest here is a set of cells at this interface.

1-2 Initial stiffening
Compliant cells begin deforming around the super-structure via nodal hinging. Like the $\bar{\rho} = 0.08$ lattices, there is significant warping in the lattice at the start of testing which does not improve over loading as it appears that the nodes are simply allowing the struts to rotate. As individual nodes reach their maximum hinging capability and transition towards s-bending, the collective stiffness increases.

3 Plateau
Compliant cells are no longer able to deform independently and rely on the strength imparted by the super-structure to prevent fracture. Cells that are not directly supported by the super-structure begin to stretch. At this point, the stiff phase begins to take up more load and dictate stiffness behavior.

4 Softening to fracture
S-bending begins in some compliant beams which are bounded by the stiff inclusions. The stiffness response is similar to that of $\bar{\rho} = 0.30$, suggesting that the stiff phase is dictating stiffness response at this point. Failure occurs, similar to Bamboo, by stretching at a compliant node.

Where the Bamboo lattices showed the possible indirect effects of nodal stiffness, the direct effects are particularly visible in the Nacre lattices. Compliant beams which are fully contained within the diamond super-structure hardly deform, as they seem to be directly supported by the stiffness of the connecting node. This provides context for why fracture did not propagate through the diamond

structure; the compliant beams were merely moving with the stiff structure and could not independently deform. Adding to this, beams which were connected to a stiff inclusion at only one end show a cantilever-like behavior, acting more like a clamped boundary condition rather than pinned spring. When this evidence is considered in conjunction with the fracture patterns and deformation fields, this makes sense; the largest deformations do not appear immediately outside the diamond structure, but are usually offset by one cell. Similarly, fracture also tends to develop one cell length away from the diamond. Together, these phenomena suggest that nodal stiffness is more important to beam deformation shape than the beam stiffness itself.

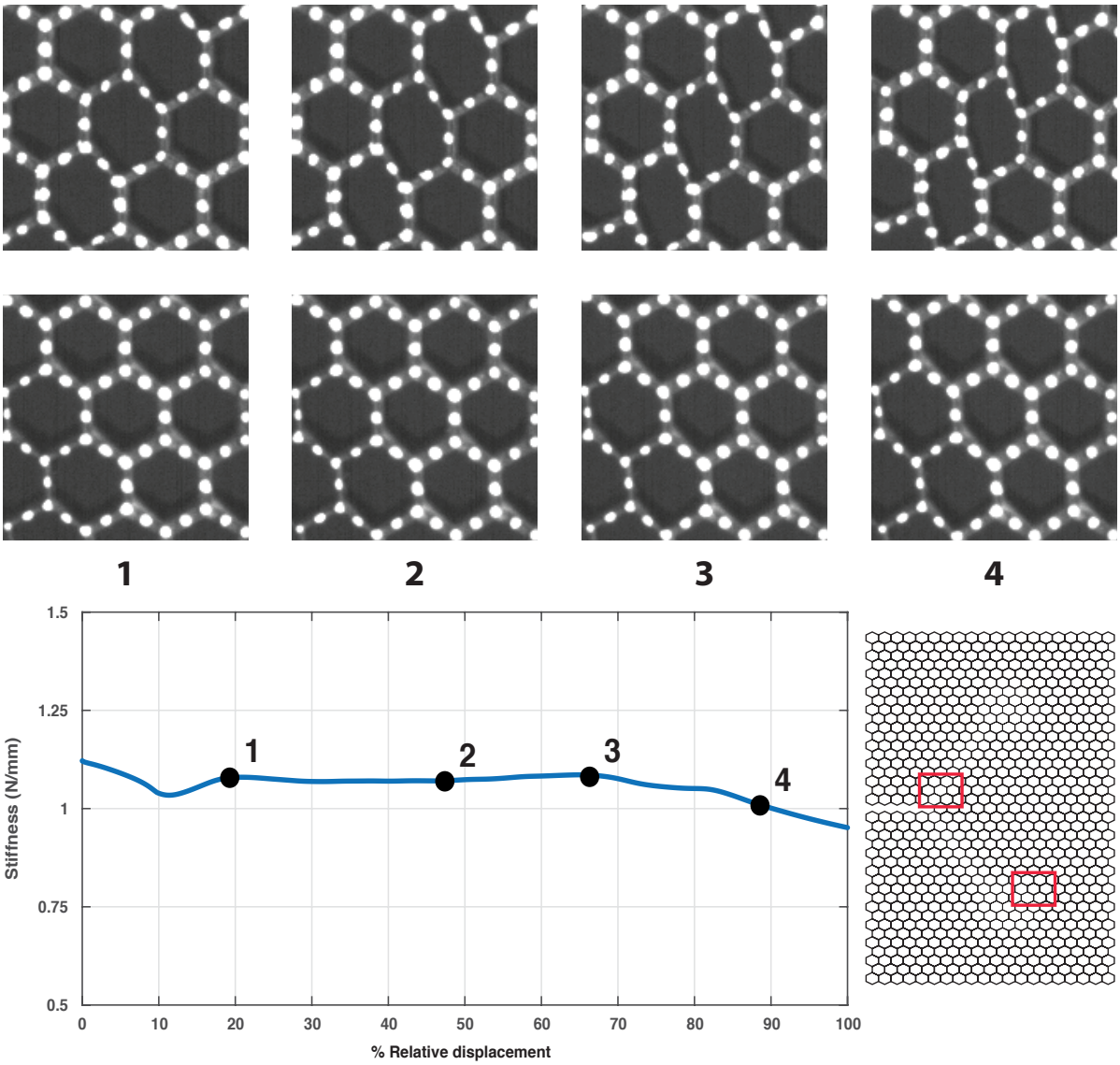

Figure 9.8: *Stiffness curve for an Etching lattice with highlighted points of interest and corresponding cell deformation behavior*

9.2.3. Etching

Despite having almost seemingly identical force-displacement behavior, the stiffness curve profile of the Etching lattices tells a different story, having a much longer LE regime than any other lattice (uniform or hierarchical) and relatively little strain softening. Two areas of interest are taken here: the first is just ahead of the crack tip where the compliant channels are located, and the second is just to the right of the sink regions, chosen for the elongation concentrations that form there during loading.

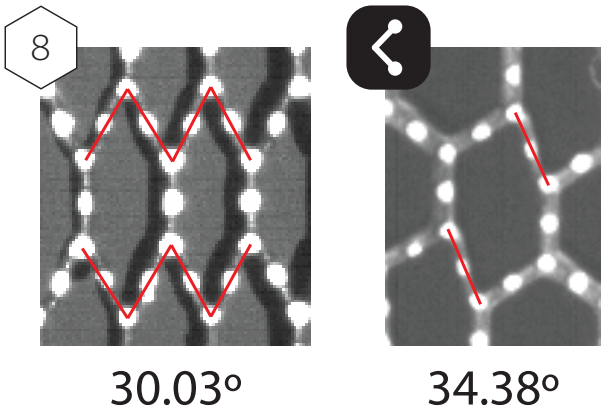

Figure 9.9: *Cells used to calculate average strut rotation for a $\bar{\rho} = 0.08$ (left) and Etching (right) lattice with average strut rotation indicated underneath each image.*

1 Linear-elastic regime
These lattices exhibit behavior that most resembles a linear-elastic regime, a response which is very similar to the elastomeric-type profile, though the overall stiffness is larger compared to the low-density uniform lattices. This suggests that the initial stiffness value is driven by the stiff phase. Cell deformation, however, is dictated by nodal hinging in the compliant struts.

2-3 Brief stiffening
Compliant beams begin to show s-bending, but reach their maximum quickly.

4 Softening
Onset of lattice softening coincides with the formation of large elongation concentrations just to the right of the sink regions. Compliant beams continue to rotate and stretch as loading increases up to fracture, while stiff beams begin to display nodal hinging, and, at fracture, slight s-bending.

Etching lattices provide further evidence that nodal stiffness is a critical component in lattice behavior. Bounded by the $\bar{\rho} = 0.30$ lattice, compliant beams are able to withstand significantly higher rotations compared to even uniform $\bar{\rho} = 0.08$ lattices, evidenced by Figures 9.8 and 9.9. It is possible that, like in Bamboo, they had not reached the limits of deformation, as fracture often did not initiate in the compliant channels, but instead in the sink regions.

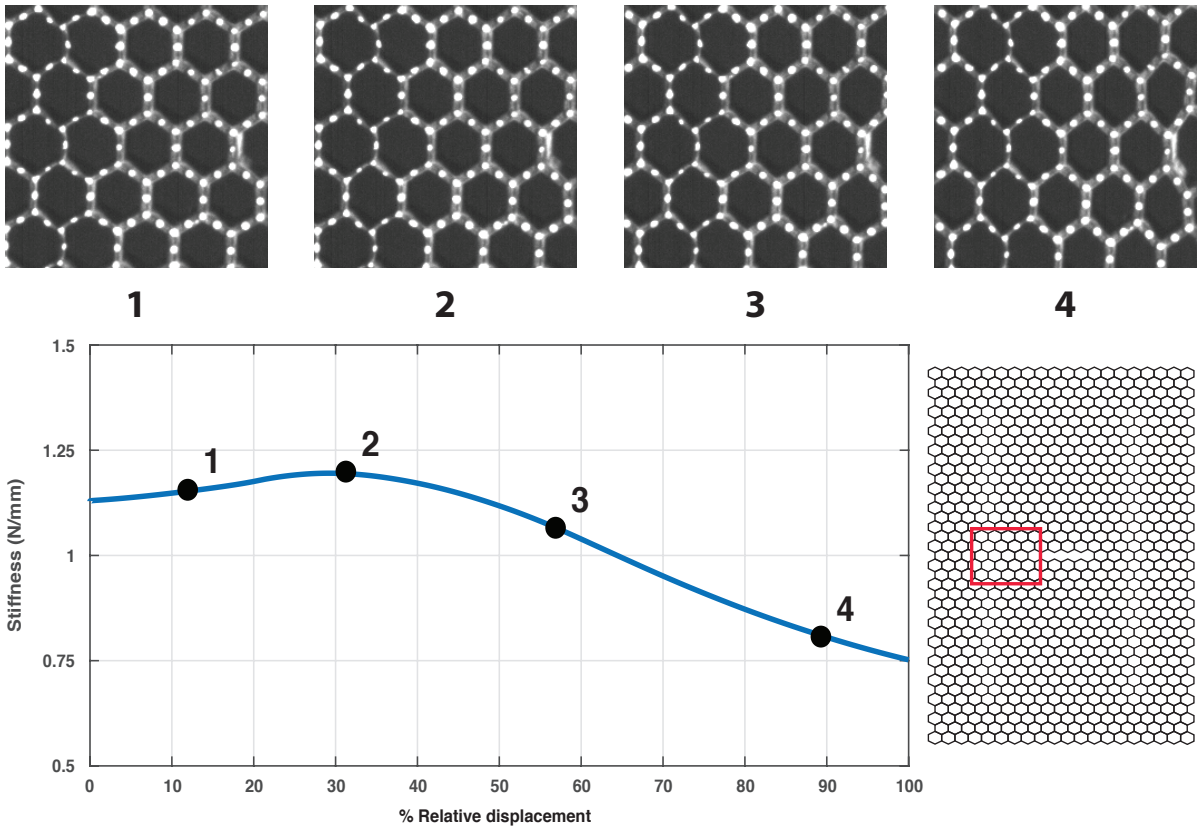

Figure 9.10: *Stiffness curve for a Glass Sponge lattice with highlighted points of interest and corresponding cell deformation behavior*

9.2.4. Glass Sponge

Unlike the other hierarchical configurations, the profile of Glass Sponge lattice stiffness curves are not substantially different from the hybrid profile, leading to the question of why this is.

Disregarding individual cell deformation behavior for a moment, consider the specimen's geometry: the compliant channels are aligned with the loading direction, meaning that the cross-section is more or less consistent throughout the height of the lattice. The compliant channels, supported by the stiff material surrounding them, are not able to easily deform independently or contribute to lattice mechanical response in a meaningful way. Thus, the stiffness response will be largely dictated by the stiff $\bar{\rho} = 0.30$ phase [7].

That said, in order to make a convincing argument on this prediction, the cell-level deformation behavior of the Glass Sponge lattice should still be examined. For this, an area including the left crack tip and its corresponding compliant channel is chosen, shown in Figure 9.10.

1 Initial stiffening
This period is characterized by predominantly vertical elongation which is possible through nodal hinging in the stiff phase cells; the compliant cells do not noticeably deform

2-4 Plateau and softening
Stiff phase transitions from nodal hinging to s-bending. similar to the behavior seen at an equivalent stage in the uniform $\bar{\rho} = 0.30$ lattice. The largest deformations are seen at the crack tip. In the compliant channels, nodal hinging continues to occur with no new s-bending.

The cell deformation behavior does, indeed, show that the compliant channels are not contributing substantially to the overall lattice mechanical response and mainly deform with the surrounding stiff

[7] It is possible that omitting the $\bar{\rho} = 0.10$ phase entirely might produce similar stiffness curve results and fracture behavior. Without a perfect comparison to the tapered, edge-cracked uniform lattices, however, this cannot be confirmed with the current experimental data.

structure. The outcome is not necessarily bad. Instead, these lattices demonstrate that it is possible reduce the mass of a lattice in a way that controls fracture, but does not significantly alter lattice-level response. An interesting observation can be also made on nodal stiffness. Heavily warped struts in other lattices, specifically uniform $\bar{\rho} = 0.08$ and Nacre, did not straighten unwarp during testing. Several warped compliant cells in Glass Sponge lattices, by contrast, did appear to straighten out, providing more evidence of the impact of structural hierarchy on nodal stiffness and its importance in cell deformation behavior.

9.3. Summary

This chapter presented a discussion on the experimental results of the set of hierarchical lattices, focusing initially on the set of the hypotheses which addressed the effects of either adding stiff inclusions to a compliant lattice (compliant/stiff) or creating compliant regions in a stiff lattice (stiff/compliant) on mechanical response. While these hypotheses helped establish that there is a distinction in the responses at this level, differences between each specific topology within these groupings could not be sufficiently explained.

Therefore, as was done for the uniform lattices, the stiffness-displacement response of each hierarchical lattice topology was correlated with cell deformation behaviors. The stiffness response can be described very generally for all hierarchical lattices, with the exception of Glass Sponge:

1. Initial response is dictated by deformations in the compliant phase. This is evidenced by nodal hinging, and later s-bending, in these beams only, and supported by the similarity to the elastomeric-type behavior seen in low-density uniform lattices.
2. A plateau forms as the compliant struts can no longer deform independently and the stiff phase begins to take up more load. In a uniform, low-density lattice, fracture would have likely occurred by now, but the stiff phase provides additional strength that supports the compliant beams.
3. Lattice strain softening occurs as the stiff beams begin to deform via nodal hinging, and later s-bending. At this point, the stiff phase is dictating stiffness response, supported by similar behavior seen in the final phases of the hybrid- and elastoplastic-type stiffness curves.

While lattices follow the same general pattern, the specific topologies create differences in, for instance, when the stiff phase begins to dictate the stiffness response, resulting in unique responses for each lattice and highlighting the importance of how hierarchy is created in a lattice structure.

10

Conclusions and Future Work

10.1. Conclusions

The future of aviation will undoubtedly necessitate the development of new tough, lighter-weight structures. Lattice materials show promise in contributing to this future, but research into tensile behavior is still in its early stages, and this is especially so for lattices under tensile loading. Any future aerospace structure will need to be damage-tolerant to ensure continued safety, as shown in Section 2.1.

But long before then, it is critical to understand how these structures behave and how they respond to changing parameters, such as relative density. As discussed in Chapter 3, relative density is undoubtedly one of the most important parameters defining lattice mechanical response, so it logically follows that mechanical response should be affect by local variations in relative density. The question remains, how this behavior manifests itself. These gaps in understanding lead to the guiding question of this research:

How does mechanical response relate to cell toughening mechanisms that result from structural hierarchy in cellular materials?

The initial research objective was primarily to observe how adding structural hierarchy by means of relative density impacts mechanical response and fracture behavior in a 2D honeycomb structure. The result, however, was a deeper understanding of not only the effects of relative density on fracture behavior, but how cell deformation behavior varies over loading and how this manifests itself in the stress-strain and stiffness-displacement responses. This information was then used to understand how hierarchical lattice stiffness response can be directly linked to the interactions between cells of varying relative density.

The main findings of this thesis can be summarized in three categories for both uniform and hierarchical lattices:

Lattice mechanical response and fracture behavior

- **Uniform**
  A double-lobed butterfly shape is visible in the rotation deformation field at the crack tip. Fracture in these lattices is highly random; microcracking and crack deflection are the primary toughening mechanisms. As relative density increases beyond this point, force-displacement and stiffness-displacement response becomes increasingly more brittle. Fracture is characterized by sudden, violent ruptures which travel straight across the lattice. At all relative densities, lattices showed a unique ability to survive premature strut failure; a temporary loss of strength is not necessarily catastrophic. This phenomenon is most evident in low-density lattices, where microcracking appears to be a mechanism to delay complete fracture, reflecting observations of the damage evolution of natural materials, suggesting that describing lattice toughness solely using $\bar{K}_{IC}$ may not be adequate or appropriate.

- **Hierarchical**
  The impact of hierarchy on lattice stiffness is varied; stiff inclusions in a compliant lattice yielded a statistically significant increase in $\bar{E}$ over low-density uniform lattices, while removing material from a stiff lattice did not significantly impact $\bar{E}$ compared to $\bar{\rho} = 0.30$ lattices. Overall, fracture behavior in all lattices was more consistent than in uniform lattices; compliant channels in stiff lattices were the most effective at consistent crack deflection, while stiff inclusions in a compliant lattice successfully diverted propagating cracks, but had less consistent fracture patterns.

Cell deformation and stiffness response

- **Uniform**
  Three general stiffness curve profiles have been identified: *elastomeric*, *elastoplastic*, and *hybrid*. Contrary to literature, below $\bar{\rho} = 0.20$, lattice mechanical response can be characterized as ”elastomer-like”, despite the lattice being manufactured from a brittle material. Changes in the stiffness response during loading are associated with different cell deformation shapes. All lattices begin by deforming via nodal hinging; in elastomeric-type lattices, this is associated with a long linear-elastic regime, and in elastoplastic- and hybrid-type lattices, this is associated with lattice strain softening. The onset of s-bending is marked by lattice strain hardening in elastomeric- and hybrid-type lattices and by a change in the slope of the stiffness curve in elastoplastic-type lattices. The cell deformation progression contradicts Gibson and Ashby’s prediction for lattices made from a polymer material.

- **Hierarchical**
  The initial stiffness response is governed by the deformations in compliant phase, with cells showing nodal hinging followed by s-bending. As compliant cells reach the limits of s-bending, the stiff phase takes up more load and governs stiffness response up to failure, deforming primarily by nodal hinging up to failure.

Cell deformation and nodal stiffness

- **Uniform**
  In high relative densities ($\bar{\rho} > 0.20$), strong nodes and stiff beams allow little rotation and relatively higher elongation. Low relative density ($\bar{\rho} < 0.20$) nodes impart comparatively little strength, allowing for high rotations with relatively lower elongation.

- **Hierarchical**
  Stiff-phase struts appear to directly and indirectly support compliant-phase struts, resulting in, among others, higher compliant beam rotations, complete redirection of deformation concentrations, delaying onset of failure, or forcing failure by stretching.

10.2. Future work

The study of the in-plane tensile properties of lattice structures is a relatively new field which, primarily due to manufacturing challenges, has been mostly relegated to numerical investigations. But with continued advancements in novel manufacturing techniques come increased opportunities to further understand the mechanical responses of lattice structures and study the impacts of varying different parameters.

10.2.1. Improvements to the methodology

Material effects

The scope of this research is limited to lattices manufactured from a specific, proprietary photopolymer resin, a choice which comes with several unknowns that were discussed in Chapter 6. Two consequences arise from this which could form the basis for future research: the inability to separate the influence of material and geometry in the lattice response and that results cannot be extrapolated and applied to other materials. Additionally, it is impossible to differentiate the response due to the lattice geometry from the response inherent to the material because no constitutive model currently exists for Formlabs resins. A constitutive model would be useful to determine whether the effects of strain-rate sensitivity and viscoelasticity significantly impact tensile lattice response.

Higher-resolution deformation field calculations

The main outcomes of this work regarding the deformation fields are restricted to quantifying strut elongation and rotation behavior and qualitatively identifying a relationship between cell deformation and global lattice response. In reality, cell deformation behavior is more complex and cannot be fully described simply by elongation and rotation.

Thus, a more rigorous study of cell deformation behavior employing five dots per beam, instead of three, could bring clarity on several aspects of this research. At a high level, the full stress state of

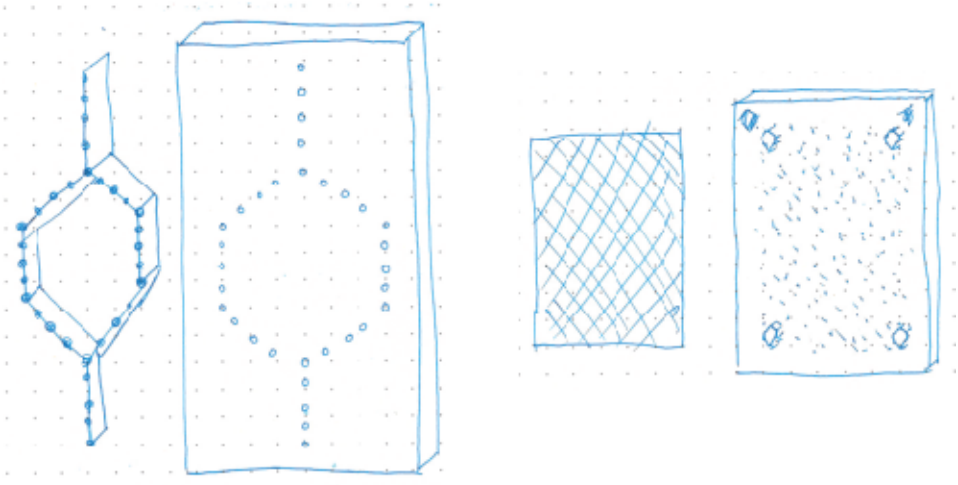

Figure 10.1: *Sketch of proposed dot-painting setup*

entire lattice could be calculated from the deformations at any point during loading, providing a better comparison to, for instance, finite-element models. In terms of this research, the correlation between cell deformation shape and stiffness response could be quantitatively confirmed for uniform lattices, which would feed into a better understanding of the hybrid stiffness responses of hierarchical lattices.

This method would be relatively easy to implement, as it only requires the addition of two raised dots per beam on the lattice surface. If the same materials are used, however, this would inevitably require a more reliable method to paint the raised dots. A possible solution, sketched in Figure 10.1, is to design a complementary plate with raised dots at the same locations as those on the lattice. The entire plate can be spray-painted, and so long as the paint layer thickness is less than the height of the dots, paint should not seep onto the lattice struts. Protruding honeycomb cells in each corner would ensure alignment as the lattice is placed on top of the plate.

For data processing, the Matlab applet created for calculating deformations already has a function for building beam associations using five dots instead of three. In the future, the deformation calculations will also be expanded to be able to handle five-dot beams. These changes are aimed at providing seamless data processing for both dot configurations and will be made available for future research.

10.2.2. Towards a better structural hierarchy

Hybrid hierarchical structures

Each of the hierarchical lattice configurations demonstrated unique strengths and weaknesses. None could be considered optimal in terms of damage tolerance, however. In lattice structures, a damage-tolerant design would likely see small, predictable fractures combined with crack-arresting or -diverting features. Section 9.2 presented evidence that hierarchy does not homogenize the stiffness response, rather that the effects of each phase are distinctly visible. Therefore, a possible avenue to explore is blending various hierarchical topologies within one lattice to force certain responses. Of course, this significantly widens the scope of possible topologies, but it can be narrowed by focusing on a few elements: sacrificial beams which help dissipate strain energy and stiff sections which support compliant cells without creating areas for stress to concentrate.

In order to remain effective, sacrificial elements should fracture predictably. The stiff/compliant lattices showed that a large disparity in relative density produces consistent fracture patterns, but came at the expense of sudden, violent fracturing. A small difference in relative density, on the other hand, may be susceptible to defects, causing fracture to initiate somewhere other than at a sacrificial element. Therefore, it is likely that an ”optimal” difference exists which results in a predictable fracture path without building up large amounts of strain energy in the rest of the lattice.

Adding stiffness to a compliant lattice is a delicate process, evidenced by the Bamboo and Nacre lattices. The sparse inclusions in the Bamboo lattices diverted cracks and completely altered the deformation behavior, but unintentionally caused cells trapped in the corners to stretch to failure. The Nacre lattices, on the other hand, had fewer inclusions than Bamboo, but their dense packing resulted

in a stiffness concentration which created large deformations in the compliant phase. That said, both lattices demonstrate how stiff inclusions could be tailored to support compliant beams and deflect crack growth. Further research would be required to fully understand the relationship between the nodal stiffness that arises from differences in relative density and strut deformation behavior. Other inclusion shapes could also be explored, such as a single line ”floating” in the lattice. The Glass Sponge lattice response suggests that the compliant regions parallel to the load direction do not substantially alter lattice properties, such as lattice elastic modulus. Therefore, it is possible that the inverse is also true; a higher-density line in a low-density lattice is not stiff enough to create large stress concentrations, but is still able to help deflect, or possibly arrest, crack growth.

Structural hierarchy with nodal topology

A further expansion of the structural hierarchy concept is to combine relative density with variations in nodal topology. Van Helvoort found that the sharp internal corners of regular hexagonal unit cells create stress concentrations at the nodes which reduce strut deflection rigidity, and that applying bioinspired fillets to the nodes can increase the strut deflection rigidity of a lattice [45]. This knowledge could be implemented in a relative density-hierarchical structure as a way to further tailor fracture behavior.

Take sacrificial elements, for instance; applying fillets to the stiff phase would increase the structural rigidity of the phase without substantial gain in mass. This could push the ”optimal” difference between phase relative densities closer together that still ensures a consistent fracture pattern, creating an even lighter-weight structure. Another possibility is to use the weakness of unfilleted nodes as a way to force fracture to occur at a particular location, while crack-arresting features further across the lattice have filleted nodes to absorb more fracture energy.

Introducing nodal topology as a variable would, undoubtedly, add significant complexity. Before attempting to design lattices varying both relative density and nodal topology, a more thorough investigation would need to be conducted into the effects of relative density interfaces on nodal stiffness. This could then be combined with variations in nodal topology to gain a better understanding of whether one parameter has a greater impact on nodal stiffness.

Bibliography

[1] Formlabs, “Materials Data Sheet: Photopolymer Resin for Form 1+ and Form 2,” 2019.

[2] M. Ashby, “No Title,” 2002.

[3] S. Amada and S. Untao, “Fracture properties of bamboo,” *Composites Part B:Engineering*, vol. 32, pp. 451–459, 1 2001.

[4] “Photo Gallery | Peak Bamboo,” 2018.

[5] A. Woesz, J. C. Weaver, M. Kazanci, Y. Dauphin, J. Aizenberg, D. E. Morse, and P. Fratzl, “Micromechanical properties of biological silica in skeletons of deep-sea sponges,” *Journal of Materials Research*, vol. 21, pp. 2068–2078, 8 2006.

[6] O. Kolednik, J. Predan, F. D. Fischer, and P. Fratzl, “Bioinspired design criteria for damage-resistant materials with periodically varying microstructure,” *Advanced Functional Materials*, vol. 21, pp. 3634–3641, 10 2011.

[7] L. Gibson and M. F. Ashby, *Cellular Solids: Structure and Properties*. 1987.

[8] V. S. Deshpande, M. F. Ashby, and N. A. Fleck, “Foam topology: Bending versus stretching dominated architectures,” *Acta Materialia*, vol. 49, no. 6, pp. 1035–1040, 2001.

[9] I. Schmidt and N. A. Fleck, “Ductile fracture of two-dimensional cellular structures,” *International Journal of Fracture*, vol. 111, pp. 327–342, 2001.

[10] G. Mayer, “Mechanical energy dissipation in natural ceramic composites,” *Journal of the Mechanical Behavior of Biomedical Materials*, vol. 76, no. June, pp. 21–29, 2017.

[11] H. C. Tankasala, V. S. Deshpande, and N. A. Fleck, “2013 Koiter Medal Paper: Crack-Tip Fields and Toughness of Two-Dimensional Elastoplastic Lattices,” *Journal of Applied Mechanics*, vol. 82, p. 091004, 9 2015.

[12] C. B. Bucknall, “Quantitative approaches to particle cavitation, shear yielding, and crazing in rubber-toughened polymers,” *Journal of Polymer Science Part B: Polymer Physics*, vol. 45, pp. 1399–1409, 6 2007.

[13] MechaniCalc, “Beam Stress & Deflection,” 2020.

[14] Federal Aviation Administration, “Advisory Circular 23-13A, Fatigue, Fail-Safe, and Damage Tolerance Evaluation of Metallic Structure for Normal, Utility, Acrobatic, and Commuter Category Airplanes,” 2005.

[15] U. D. o. Transportation, “Damage Tolerance Assessment Handbook vol. I,” *U.S. Department of Transportation*, p. 168, 1993.

[16] U. G. Wegst, H. Bai, E. Saiz, A. P. Tomsia, and R. O. Ritchie, “Bioinspired structural materials,” *Nature Materials*, vol. 14, no. 1, pp. 23–36, 2015.

[17] R. O. Ritchie, “The conflicts between strength and toughness,” *Nature Materials*, vol. 10, no. 11, pp. 817–822, 2011.

[18] M. D. Hayes, D. B. Edwards, and A. R. Shah, *Fractography Basics*. 2015.

[19] R. Z. Wang, Z. Suo, A. G. Evans, N. Yao, and I. A. Aksay, “Deformation mechanisms in nacre,” *Journal of Materials Research*, vol. 16, no. 9, pp. 2485–2493, 2001.

[20] F. Barthelat, H. Tang, P. D. Zavattieri, C. M. Li, and H. D. Espinosa, “On the mechanics of mother-of-pearl: A key feature in the material hierarchical structure,” *Journal of the Mechanics and Physics of Solids*, vol. 55, pp. 306–337, 2 2007.

[21] M. Meyers, J. McKittrick, and P. Chen, “Structural Biological Materials: Critical Mechanics-Materials Connections,” *Science*, vol. 335, pp. 199–204, 1 2012.

[22] F. Heinemann, “Electron microscopy image of a fractured surface of nacre,” 2017.

[23] Kebes, “Schematic of the microscopic structure of nacre layers,” 2005.

[24] S. V. Rupani, S. S. Jani, and G. D. Acharya, “Design, Modelling and Manufacturing aspects of Honeycomb Sandwich Structures: A Review,” *International Journal of Scientific Development and Research*, vol. 2, no. 4, pp. 526–532, 2017.

[25] L. J. Gibson, “by Lorna Jane Gibson A dissertation submitted to the University of Cambridge for the Degree of Dbctor of Philosophy Churchill College Augus t 1981,” 1981.

[26] PATEL MR and FINNIE I, “MECHANICAL BEHAVIOR OF RIGID PLASTIC FOAMS,” No. pt 1, pp. 597–615, 1970.

[27] F. K. Abd El-Sayed, R. Jones, and I. W. Burgess, “A theoretical approach to the deformation of honeycomb based composite materials,” *Composites*, vol. 10, pp. 209–214, 10 1979.

[28] W. E. Warren and A. M. Kraynik, “Foam mechanics: the linear elastic response of two-dimensional spatiallly periodic cellular materials,” *Mechanics of Materials*, vol. 6, pp. 27–37, 3 1987.

[29] J. Huang and L. Gibson, “Fracture toughness of brittle honeycombs,” *Acta Metallurgica et Materialia*, vol. 39, pp. 1617–1626, 7 1991.

[30] J. S. Huang and M. S. Chiang, “Effects of microstructure, specimen and loading geometries on KIC of brittle honeycombs,” *Engineering Fracture Mechanics*, vol. 54, no. 6, pp. 813–821, 1996.

[31] I. Quintana-Alonso and N. A. Fleck, “Fracture of Brittle Lattice Materials: A Review,” tech. rep.

[32] H. Gu, M. Pavier, and A. Shterenlikht, “Experimental study of modulus, strength and toughness of 2D triangular lattices,” *International Journal of Solids and Structures*, vol. 152-153, pp. 207–216, 11 2018.

[33] M. Ryvkin, M. B. Fuchs, F. Lipperman, and L. Kucherov, “Fracture analysis of materials with periodic microstructure by the representative cell method,” tech. rep., 2004.

[34] Y. Wu and L. Yang, “Modeling of crack propagation in 2D brittle finite lattice structures assisted by additive manufacturing,” *Solid Freeform Fabrication Symposium*, no. August, pp. 2112–2126, 2017.

[35] N. Fleck, O. Olurin, C. Chen, and M. Ashby, “The effect of hole size upon the strength of metallic and polymeric foams,” *Journal of the Mechanics and Physics of Solids*, vol. 49, pp. 2015–2030, 9 2001.

[36] A. Cherkaev and M. Ryvkin, “Damage propagation in 2d beam lattices: 2. Design of an isotropic fault-tolerant lattice,” *Arch Appl Mech*, vol. 89, pp. 503–519, 2019.

[37] F. Libonati, G. X. Gu, Z. Qin, L. Vergani, and M. J. Buehler, “Bone-Inspired Materials by Design: Toughness Amplification Observed Using 3D Printing and Testing,” *Advanced Engineering Materials*, vol. 18, pp. 1354–1363, 8 2016.

[38] L. S. Dimas, G. H. Bratzel, I. Eylon, and M. J. Buehler, “Tough Composites Inspired by Mineralized Natural Materials: Computation, 3D printing, and Testing,” *Advanced Functional Materials*, vol. 23, pp. 4629–4638, 9 2013.

[39] F. Lipperman, Ryvkin, Michael, and M. B. Fuchs, “Design of Crack-Resistant Two-Dimensional Periodic Cellular Materials,” *journal of mechanics of materials and structures*, vol. 4, no. 3, pp. 441–457, 2009.

[40] Formlabs, “Density engineering resin - Feature Requestions & Ideas - Formlabs Community Forum,” 2019.

[41] K. Ertman, “katharina-ertman/latticeDeformations: Matlab applet for one-click dot-tracking, deformation calculations, and deformation plotting for lattice structures.,” 2020.

[42] J. C. Crocker, E. R. Weeks, D. Blair, and E. Dufresne, “Particle tracking using IDL.”

[43] M. G. Laka and A. A. Dzenis, “Effect of hydrostatic pressure on the tensile strength of polymer materials,” *Polymer Mechanics*, vol. 3, no. 6, pp. 685–687, 1967.

[44] Formlabs, “Black Photoreactive Resin for Formlabs 3D printers Safety Data Sheet,” 2016.

[45] D. T. J. V. Helvoort and A. C. D. Rans, “The effect of nodal topology on cellular solid mechanics A preliminary diagnostic experimental investigation,” no. December 2018, 2018.

A

Print quality informal study

During manufacture of a set of $\bar{\rho} = 0.20$-0.40 lattices, an informal study was conducted to assess the impact of various printing parameters on print quality and eventual testing performance. The parameters documented were time, room temperature, and relative humidity at print start, print end, and start of post-printing activities, part mass and deviation from ideal mass, number of days between printing and testing, and whether lattices had cells filled with resin after washing and curing.

Results

Two pages of results can be found at the end of this appendix. The first contains the log used to note down the parameters listed above, including any additional notes, observations, or deviations from procedure. The second gathers the average mass for each relative density set and the average deviation from the ideal mass, as well as the average time to test per set. Figure A.1 on the subsequent page shows all force-displacement curves for $\bar{\rho} = 0.20$, 0.30, and 0.40 specimens which were produced during this informal study. The subsequent page contain two spreadsheets.

Discussion

Whether a lattice was deemed ”good” or ”bad” was determined based on the quality of the final lattice, i.e. whether cells were filled with resin after washing and curing, cleanliness of the part surface, and the sharpness of small features.

The suitability of this categorization was then assessed using the force-displacement curves shown in Figure A.1. At $\bar{\rho} = 0.20$, the force-displacement behavior seems to group by ”good” and ”bad” parts; maximum force is generally higher for ”bad” parts and show less consistency than the ”good” parts. A possible explanation is that the lack of precision created slightly curved internal vertices which lower the stress concentration at the node and delay fracture. As relative density increases, the ”bad” $\bar{\rho} = 0.30$ and 0.40 lattices become noticeably more tacky to the touch, possibly not having cured properly during the UV curing cycle. This likely meant that these lattices were more compliant than expected, which is corroborated by the relatively higher number of load drops in the force-displacement curves compared to ”good” lattices.

Other parameters related to printing, such as relative humidity and temperature, time between print finish and the start of post-printing activities, do not seem to affect whether a lattice will be considered ”good” or ”bad”. In the case of the latter, Specimens 30_01, 02, 03, and 04 all hung from the build platform over a weekend, but 01 and 02 were deemed ”good” while 03 and 04 were deemed ”bad”. Similarly, the average time between printing and testing was the same for both sets, so it is unlikely that this had a significant impact.

From this informal study, a general conclusion can be drawn that the quality of a finished part is the most likely indicator of whether a lattice is considered ”good” and ”representative” for testing. Variation can still occur due to the nature of these lattices and the manufacturing process, but a visual inspection is more likely-than-not to be sufficient for assessing part quality.

RD	Part #	Printer	Start date	Start time	End date	End time	Post date	Post time	Time difference	Filled cells?	Mass (g)	Mass deviation	Test day	Time to test	Notes
20	1	SZ	01.10.2019	14:05	01.10.2019	23:50	02.10.2019	08:32	08:42	No	26.5	1.902	17.10.2019	15	Initial cure only 60 minutes; extra 60 minutes on 03.10
	2	SZ	01.10.2019	14:05	01.10.2019	23:50	02.10.2019	08:32	08:42	No	26.2	1.602	17.10.2019	15	Initial cure only 60 minutes; extra 60 minutes on 03.10
	3	FF	02.10.2019	18:38	03.10.2019	04:48	03.10.2019	08:27	03:39	No	24.9	0.302	17.10.2019	14	Cured flat due to part falling on top of it during wash
	4	FF	02.10.2019	18:38	03.10.2019	04:48	03.10.2019	08:27	03:39	No	25.2	0.602	17.10.2019	14	
	5	FF	07.10.2019	18:22	08.10.2019	04:48	08.10.2019	08:47	03:59	No	24.6	0.002	17.10.2019	9	
	6	FF	07.10.2019	18:22	08.10.2019	04:48	08.10.2019	08:47	03:59	No	24.8	0.202	17.10.2019	9	
	7	FF	07.10.2019	18:22	08.10.2019	04:48	08.10.2019	08:47	03:59	No	24.7	0.102	17.10.2019	9	
	8	SZ	09.10.2019	11:05	09.10.2019	17:44	09.10.2019	17:52	00:08	Yes	32.2	7.602	17.10.2019	8	Replaced SZ tank
	9	SZ	09.10.2019	17:58	10.10.2019	05:45	10.10.2019	08:46	03:01	Yes	31.3	6.702	25.10.2019	14	
	14	SZ	10.10.2019	16:17	11.10.2019	02:36	10.10.2019	15:53	13:17	Yes	32.5	7.902	25.10.2019	14	
	15	SZ	10.10.2019	16:17	11.10.2019	02:36	10.10.2019	15:53	13:17	Yes	31.6	7.002	25.10.2019	14	
25	1	FF	01.10.2019	14:05	02.10.2019	00:02	02.10.2019	08:32	08:30	No	28.7	0.983	25.10.2019	23	
	2	FF	01.10.2019	14:05	02.10.2019	00:02	02.10.2019	08:32	08:30	No	27.7	-0.017	25.10.2019	23	
	3	FF	03.10.2019	08:44	03.10.2019	19:18	03.10.2019	20:06	00:48	No	26	-1.717	25.10.2019	22	
	4	FF	03.10.2019	08:44	03.10.2019	19:18	03.10.2019	20:06	00:48	No	26.3	-1.417	25.10.2019	22	
	5	SZ	07.10.2019	18:32	08.10.2019	05:12	08.10.2019	09:01	03:49	Yes	36.5	8.783	25.10.2019	17	
	6	SZ	07.10.2019	18:32	08.10.2019	05:12	08.10.2019	09:01	03:49	Yes	37.4	9.683	25.10.2019	17	
	7	SZ	07.10.2019	18:32	08.10.2019	05:12	08.10.2019	09:01	03:49	Yes	39.4	11.683	25.10.2019	17	
30	1	SZ	03.10.2019	20:45	04.10.2019	05:42	07.10.2019	08:49	3:07 +48	No	30.5	-0.237	17.10.2019	10	Extra 60 minute cure on 07.10
	2	SZ	03.10.2019	20:45	04.10.2019	05:42	07.10.2019	08:49	3:07 +48	No	30.9	0.163	25.10.2019	18	Extra 60 minute cure on 07.10
	3	FF	03.10.2019	20:45	04.10.2019	05:35	07.10.2019	08:49	3:14 +48	Yes	31	0.263	25.10.2019	18	Extra 60 minute cure on 07.10
	4	FF	03.10.2019	20:45	04.10.2019	05:35	07.10.2019	08:49	3:14 +48	Yes	38.6	7.863	25.10.2019	18	Extra 60 minute cure on 07.10
	7	SZ	08.10.2019	17:51	09.10.2019	06:55	09.10.2019	08:49	01:54	Yes	37.4	6.663	25.10.2019	16	Filtered resin
	8	FF	08.10.2019	17:51	10.10.2019	17:17	10.10.2019	17:52	00:35	No	30.2	-0.537	17.10.2019	7	
35	1	FF	02.10.2019	08:58	02.10.2019	18:34	02.10.2019	18:36	00:02	No	33.5	-0.306	25.10.2019	23	
	2	FF	02.10.2019	08:58	02.10.2019	18:34	02.10.2019	18:36	00:02	No	33	-0.806	25.10.2019	23	
	3	SZ	03.10.2019	08:48	03.10.2019	19:14	03.10.2019	20:06	00:52	Yes, top only	39.4	5.594	25.10.2019	23	
	4	SZ	03.10.2019	08:48	03.10.2019	19:14	03.10.2019	20:06	00:52	Yes, top only	38.6	4.794	25.10.2019	23	
40	3	FF	07.10.2019	09:28	07.10.2019	16:11	07.10.2019	18:01	01:50	No	35.9	-1.008	25.10.2019	18	
	4	SZ	07.10.2019	09:40	07.10.2019	16:17	07.10.2019	18:01	01:44	Yes	46.1	9.192	25.10.2019	18	
	5	FF	08.10.2019	09:03	08.10.2019	16:59	08.10.2019	17:40	00:41	No	36.1	-0.808	25.10.2019	17	
	6	FF	08.10.2019	18:06	09.10.2019	08:17	09.10.2019	11:05	02:48	No	36.4	-0.508	25.10.2019	16	Replaced FF tank
	7	FF	08.10.2019	18:06	09.10.2019	08:17	09.10.2019	11:05	02:48	No	36.2	-0.708	25.10.2019	16	Replaced FF tank
	8	FF	08.10.2019	18:06	09.10.2019	08:17	09.10.2019	11:05	02:48	No	36.6	-0.308	25.10.2019	16	Replaced FF tank
	9	FF	10.10.2019	16:17	10.10.2019	15:46	10.10.2019	15:53	00:07	Yes	54.9	17.992	25.10.2019	15	
	10	SZ	10.10.2019	09:05	10.10.2019	15:49	10.10.2019	15:53	00:04	No	35.3	-1.608	25.10.2019	15	

RD	Nominal mass	Avg. mass	Avg. deviation	% difference	Avg. time to test
20	24.598	25.271	0.673	2.738	12
25	27.717	27.175	-0.542	-1.955	23
30	30.737	30.533	-0.037	-0.663	12
35	33.806	33.250	-0.664	-1.645	23
40	36.908	36.083	-0.825	-2.234	16
20	24.598	31.900	7.302	29.685	13
25	27.717	37.767	10.050	36.258	17
30	30.737	35.667	4.930	16.038	17
35	33.806	39.000	5.194	15.364	23
40	36.908	50.500	13.592	36.827	17

Set	Avg. time to test
Good	17
Bad	17

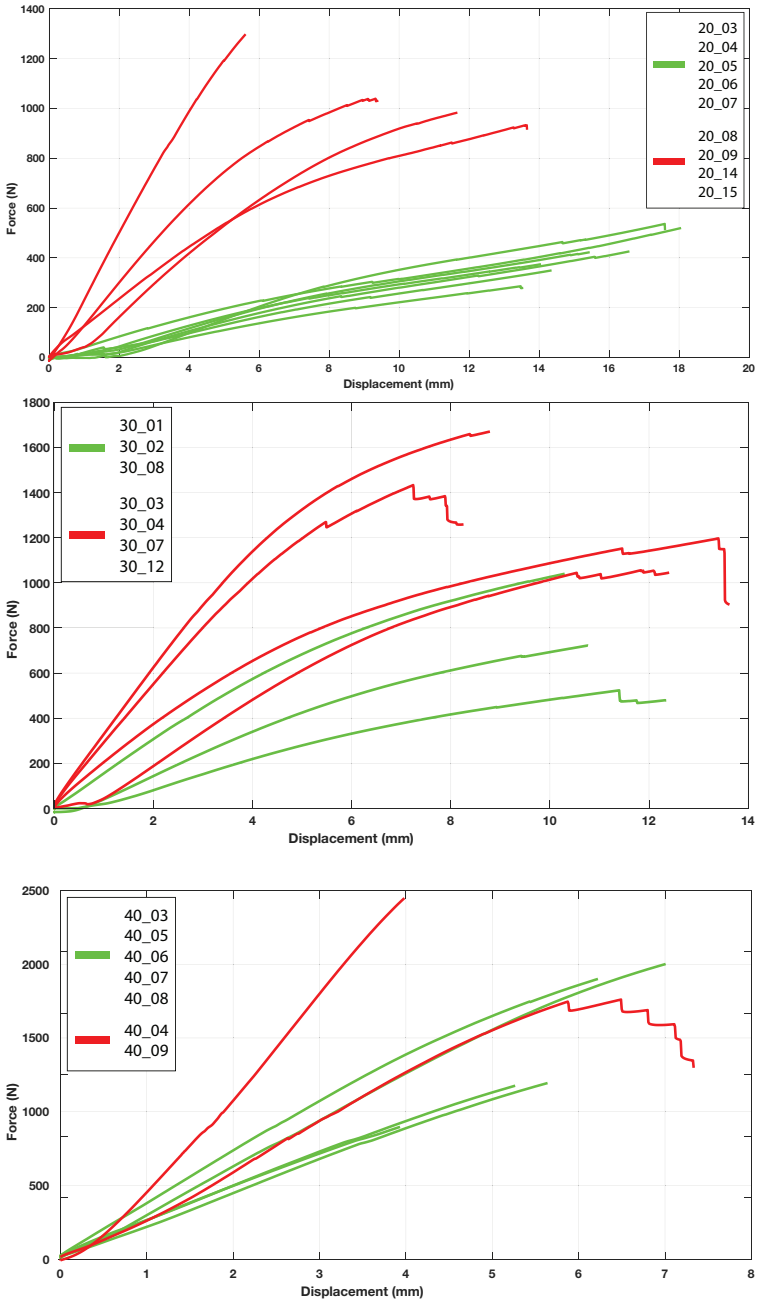

Figure A.1: *Raw force-displacement curves for specimens that were considered for this informal study. From top to bottom:* $\bar{\rho} = 0.20, 0.30,$ *and* 0.40

B

Spline curve fitting

A limitation of the methodology was the use of three dots per beam to track lattice deformation behavior, allowing only elongation and rotation deformations to be confidently measured. Some cell deformations, namely s-bending, necessitate five dots per beam to fully capture the deformation behavior. Regardless of the deformation shape, using five dots per beam would allow internal shear forces and bending moments to be calculated in each strut, ultimately providing the stress state in the lattice at any given point.

This appendix provides information on a proposed methodology for quantifying internal shear forces and bending moments using testing images of lattices with three dots per beam. Preliminary results are also presented for lattices with a uniform relative density. Finally, a short discussion is presented highlighting the limitations of this method.

Methodology

In the course of analyzing the data, a rudimentary workaround was devised which could provide some preliminary insights. For a small number of cells, a spline curve can be drawn on each strut with five points of interest using a program such as Adobe Illustrator, shown in Figure B.1. The coordinates of these spline curves were then imported to MATLAB and a polynomial fit using the *fit* function was applied. The resulting equation is the displacement function, which can then be used to estimate the internal shear force and bending moment functions:

$$M(x) = -EI\frac{d^2w(x)}{dx^2} \tag{B.1}$$

$$V(x) = -\frac{d}{dx}\left(EI\frac{d^2w(x)}{dx^2}\right) \tag{B.2}$$

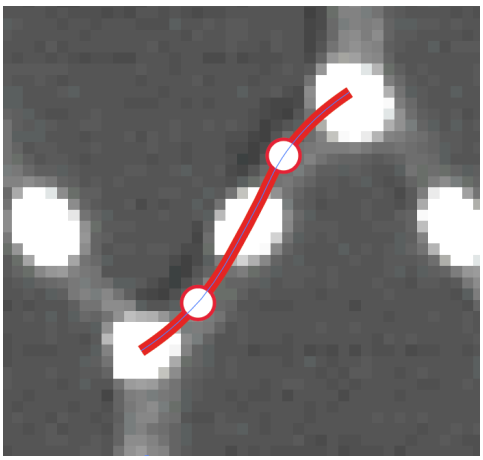

Figure B.1: *Sample spline curve drawn to follow the curvature of a strut. The coordinates of five points on the red line were then imported to Matlab for curve fitting.*

Limitations

A flaw in this analysis could not be resolved before the submission of this thesis is that the deflection and internal shear/moment functions are calculated based on a spline curve measured in pixels. Because placement of the Optomotive Velociraptor was not held constant over testing, this means that the number of pixels per millimeter of lattice likely varies slightly between specimens and, as a result, the numerical values obtained per lattice cannot be directly compared. With a bit more time this problem could be solved manually, and if this method were to attempted in the future, care should be taken to ensure that a constant px/mm conversion value could be used. That said, there is still value in doing this analysis, particularly regarding the profile of the internal shear/moment distribution over the beams.

Results and discussion

This method was applied to two cells in a representative lattices of each uniform relative density set, shown in Figure B.4. The cells were chosen such that it is reasonable to expect that the cells are least affected by the crack tip and free edges, and, therefore, these results should not be taken as representative for the entire lattice or even the relative density set and are presented purely as an initial study. Figure B.3 shows the generated moment diagrams for the selected struts in $\bar{\rho} = 0.12$, $\bar{\rho} = 0.20$, and $\bar{\rho} = 0.40$ lattices.

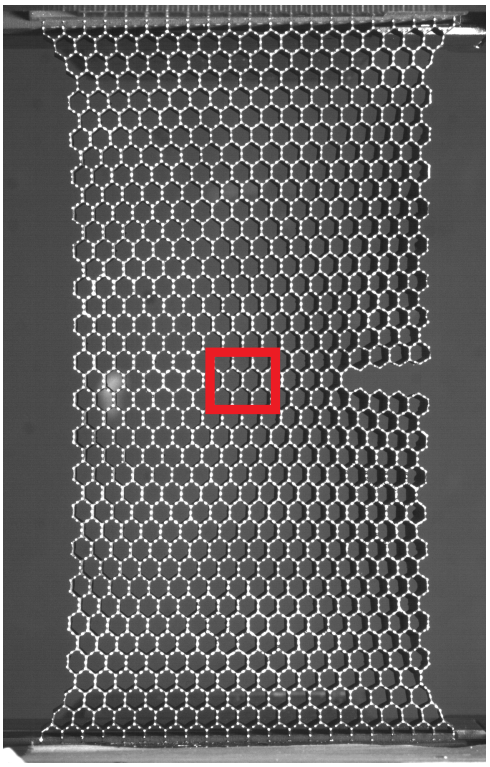

Figure B.2: *Visualization of the cells selected for spline curve fitting in a representative lattice of each uniform relative density.*

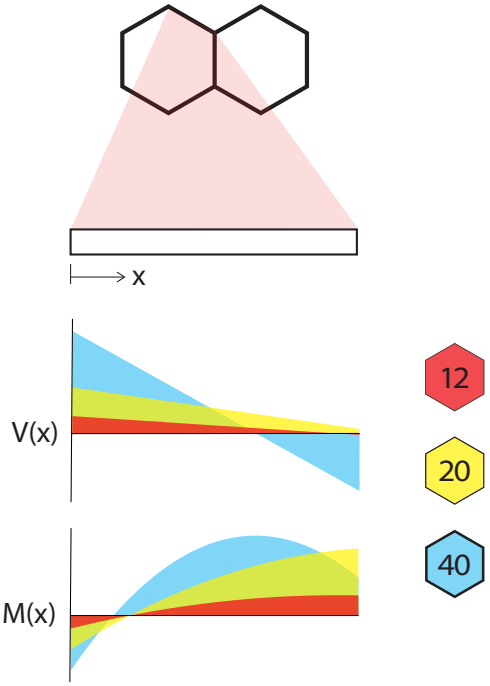

Figure B.3: *Shear force and bending moment diagrams for a selected strut in a $\bar{\rho} = 0.12$ (red), $\bar{\rho} = 0.20$ (yellow), and $\bar{\rho} = 0.40$ (blue) lattice.*

While the magnitudes of the shear and moment diagrams cannot be taken as accurate, the general shape can still be evaluated. Most notable is the asymmetry in the diagrams which is consistent across the three relative densities illustrated. Of course, the shape of the deflection curve is going to be highly dependent on the accuracy of the spline drawing, but the fact that there is consistency across three different lattices suggests that this is likely not exclusively due to human factors. The struts were all at the same relative position and orientation in the lattice, suggesting that maybe there is an inherent imbalance in the way that loads are introduced into individual beams. It may also be related to the fact that one end of the beam is aligned with the crack tip, and therefore, experiences a different load distribution compared to surrounding beams. While this is merely speculation based on a very small sample size, this does highlight the need for further research that could quantify this behavior for an entire lattice, not just a handful of cells.

The method was also applied to selected cells in an Bamboo and Etching lattice, shown in Figure B.4, and the shapes of the shear/moment diagrams can be assessed, shown in Figure B.5. These lattices were chosen because of the higher rotations seen in the compliant beams compared to the uniform lattices.

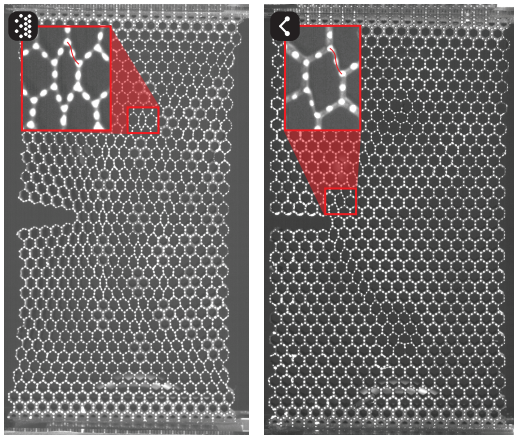

Figure B.4: *Location of the selected struts in the Bamboo and Etching lattices.*

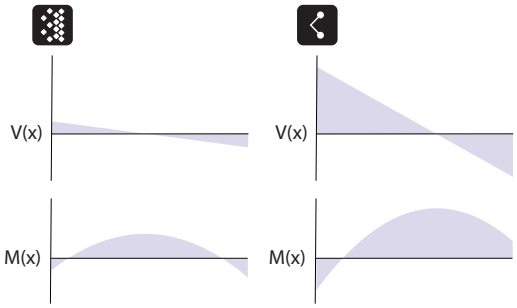

Figure B.5: *Internal shear and bending moment diagrams for a selected strut in the Bamboo and Etching lattices.*

Interestingly, the Bamboo lattice beam diagrams show a symmetry not seen in the uniform lattices, which could be a result of the strut's location or potentially an indication of more evenly-distributed loading in hierarchical structures compared to uniform lattices. The profiles also bear striking resemblance to those of a beam with fixed-fixed end conditions under a distributed load, shown in Figure B.6. A possible explanation is that the strut has reached its maximum nodal rotation angle, but because it is supported by the stiff inclusions above and below and continues to be pulled downwards and turn inwards. This would result in the fixed-fixed like condition and any additional loads applied to the strut would behave like a distributed load.

The Etching beam, therefore, should also exhibit this behavior, but instead has a similar profile to the uniform lattices. The reason is not particularly clear, though and again shows that a big limitation in this method is that it is very dependent on the accuracy of the spline fitting.

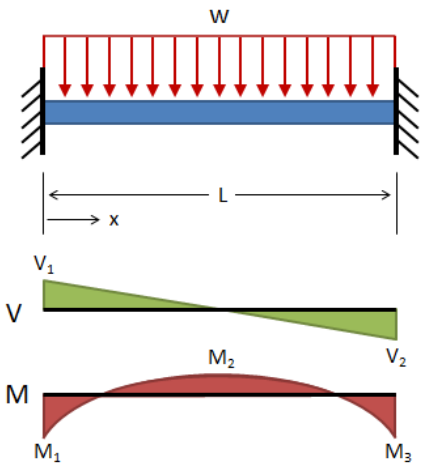

Figure B.6: *Internal shear and bending moment diagrams for fixed-fixed beam with a distributed load [13]*

C

Supplemental data

This appendix contains a selection of additional results for convenience. The following page provides the full set of force-displacement and stiffness-displacement curves for both uniform relative density and hierarchical lattices. Subsequent pages contain the force-displacement curve, final elongation and rotation deformation fields, and the fracture paths for select additional specimens of each (uniform and hierarchical) set.

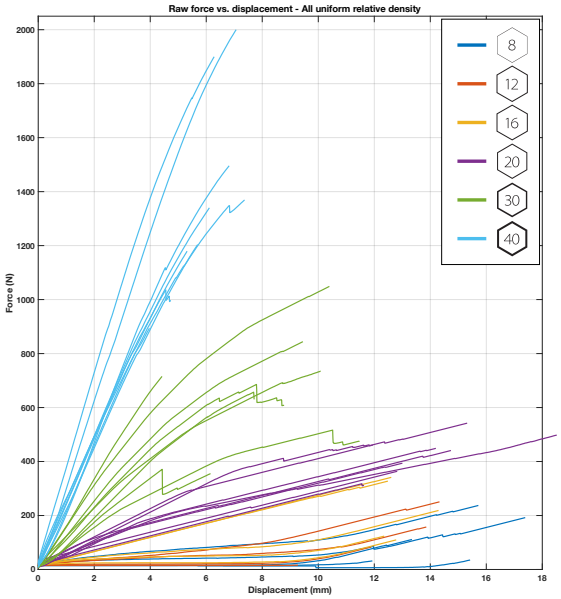
Raw force vs. displacement - All uniform relative density
Force (N)
Displacement (mm)
8
12
16
20
30
40

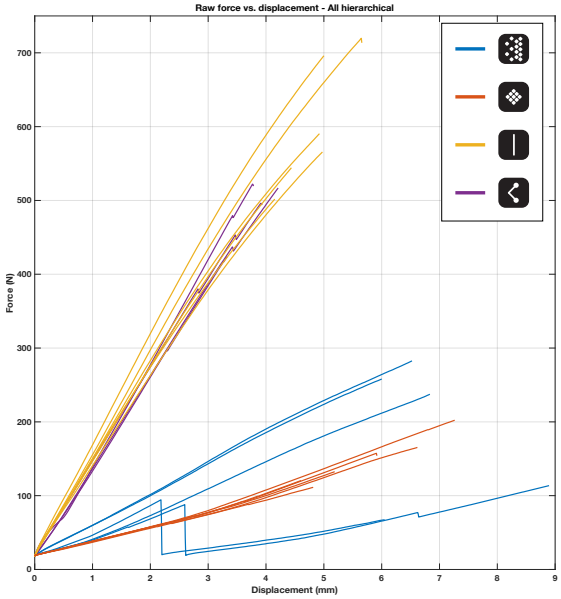
Raw force vs. displacement - All hierarchical
Force (N)
Displacement (mm)

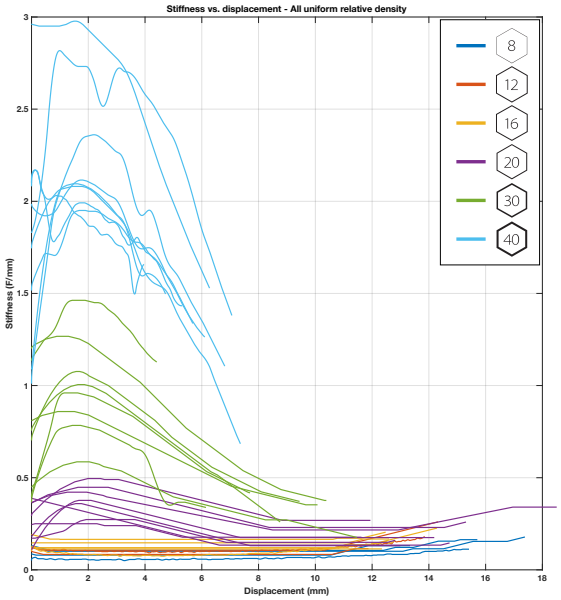
Stiffness vs. displacement - All uniform relative density
Stiffness (F/mm)
Displacement (mm)
8
12
16
20
30
40

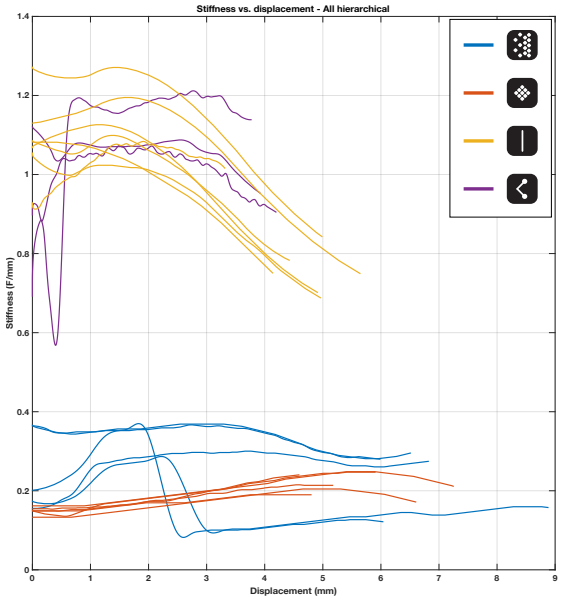
Stiffness vs. displacement - All hierarchical
Stiffness (F/mm)
Displacement (mm)

08_07

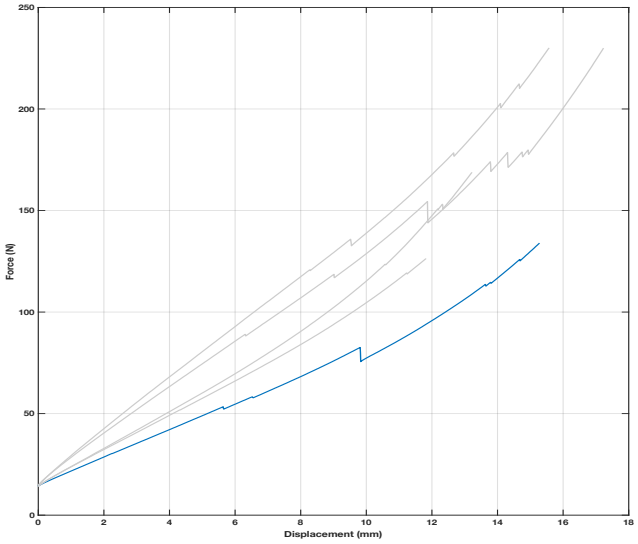
Force (N)
Displacement (mm)
0
50
100
150
200
250
0
2
4
6
8
10
12
14
16
18

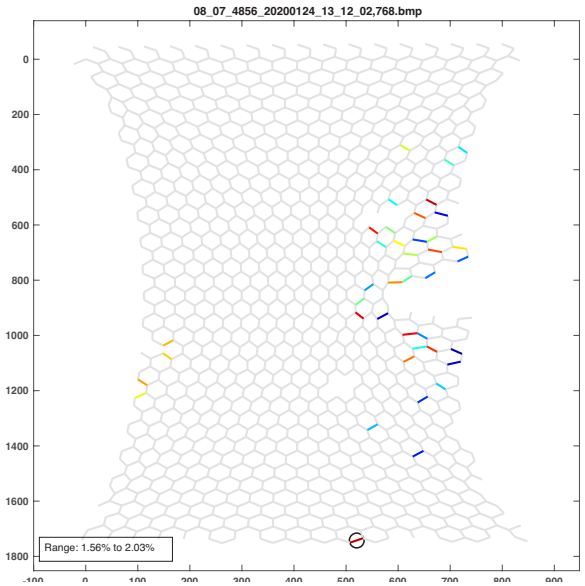
08_07_4856_20200124_13_12_02,768.bmp
Range: 1.56% to 2.03%

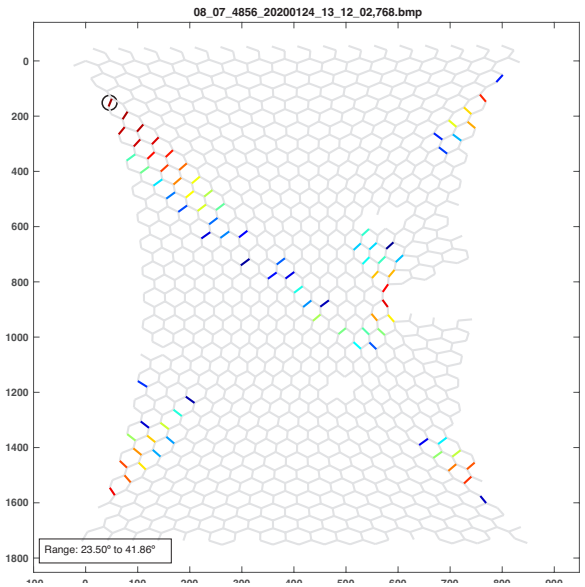
08_07_4856_20200124_13_12_02,768.bmp
Range: 23.50° to 41.86°

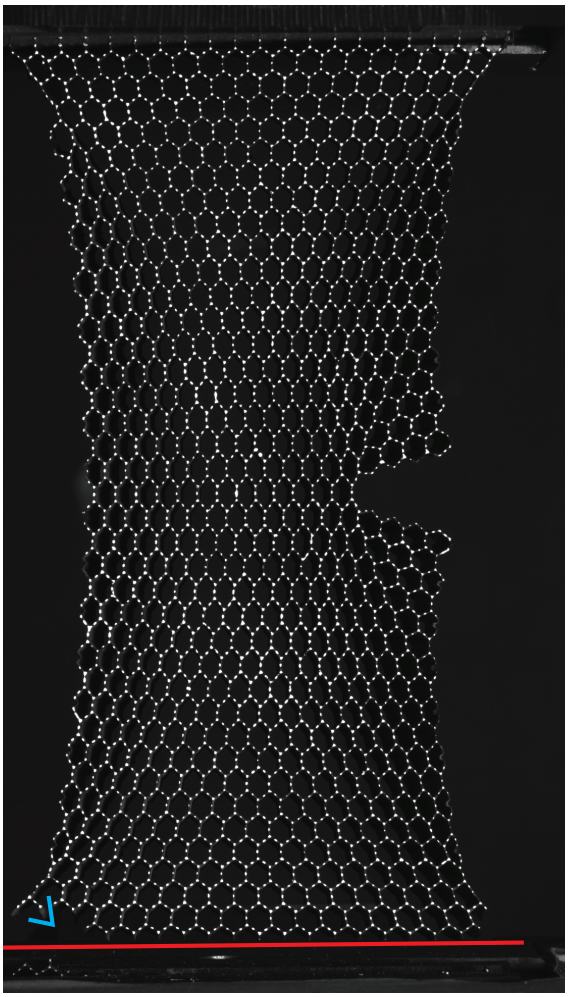

12_01

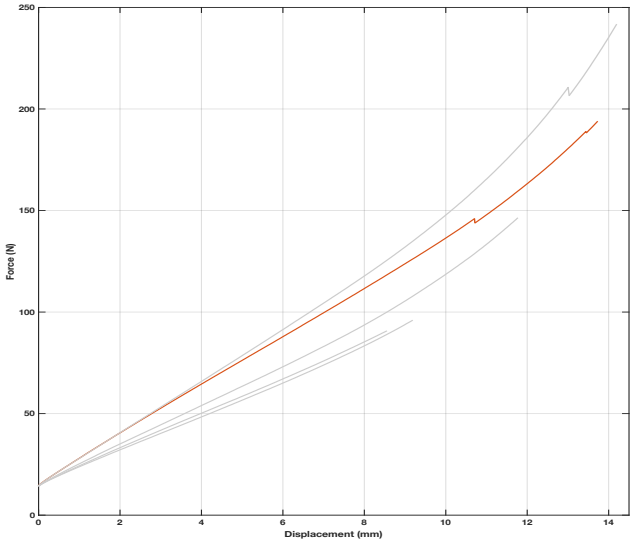
Force (N)
Displacement (mm)

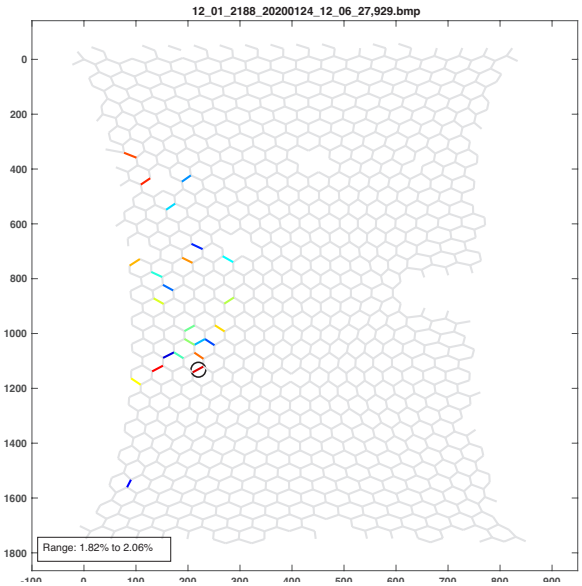
12_01_2188_20200124_12_06_27,929.bmp
Range: 1.82% to 2.06%

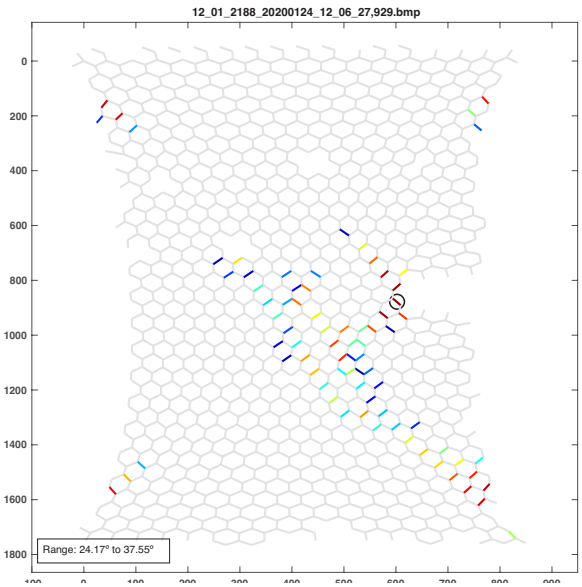
12_01_2188_20200124_12_06_27,929.bmp
Range: 24.17° to 37.55°

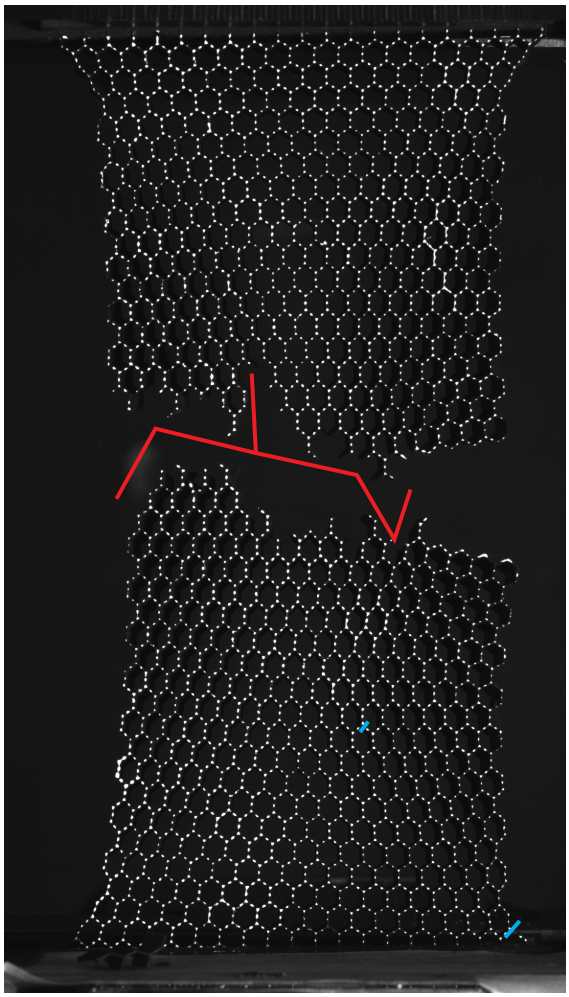

16_02

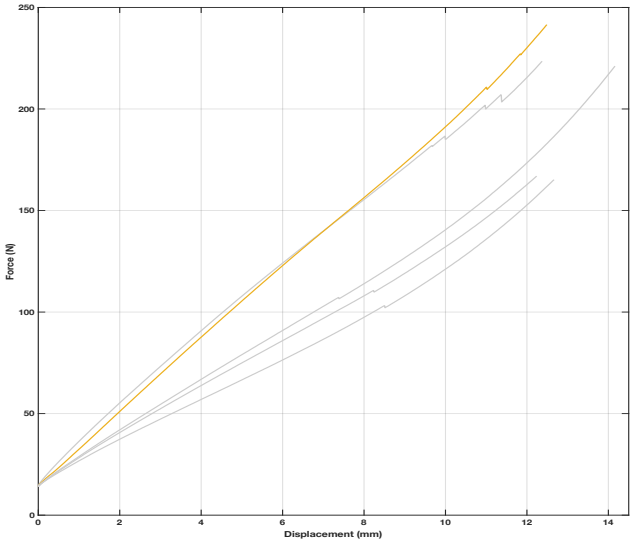
Force (N)
Displacement (mm)
0
50
100
150
200
250
0
2
4
6
8
10
12
14

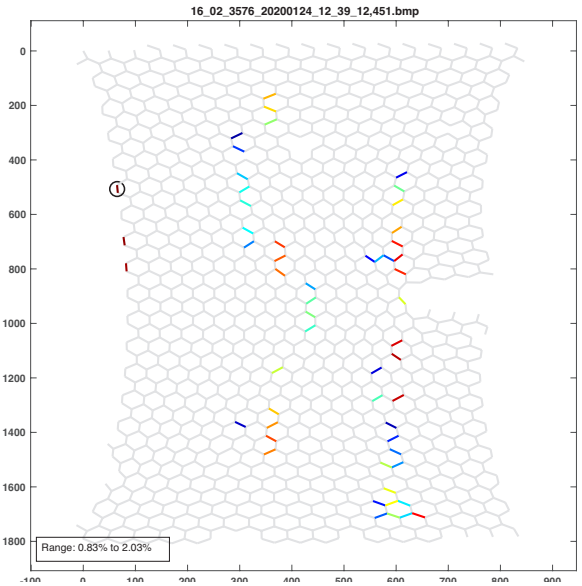
16_02_3576_20200124_12_39_12,451.bmp
Range: 0.83% to 2.03%

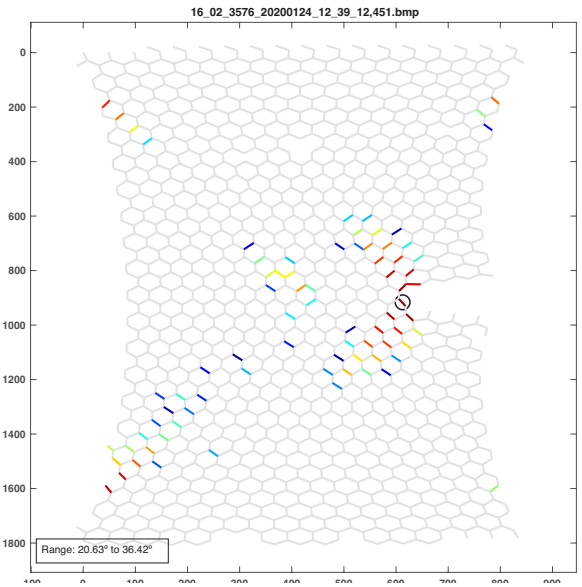
16_02_3576_20200124_12_39_12,451.bmp
Range: 20.63° to 36.42°

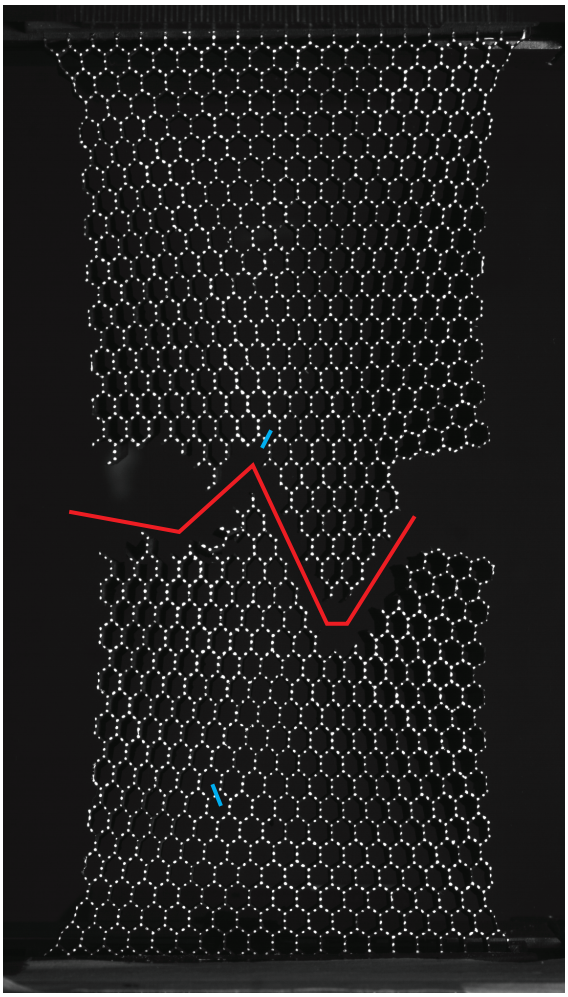

20_21

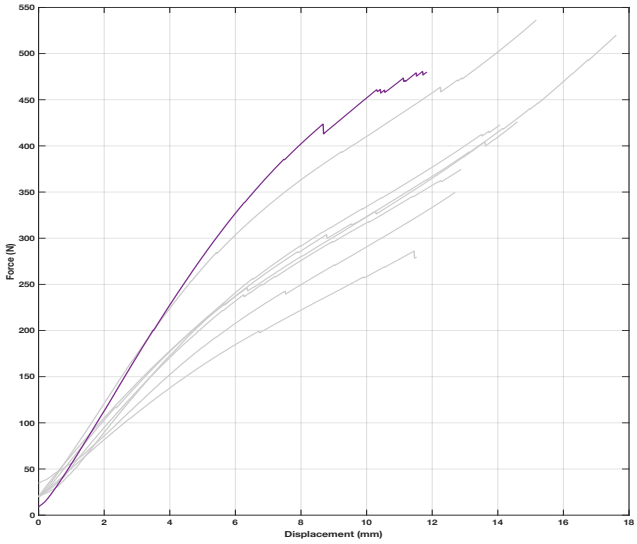
Force (N)
Displacement (mm)

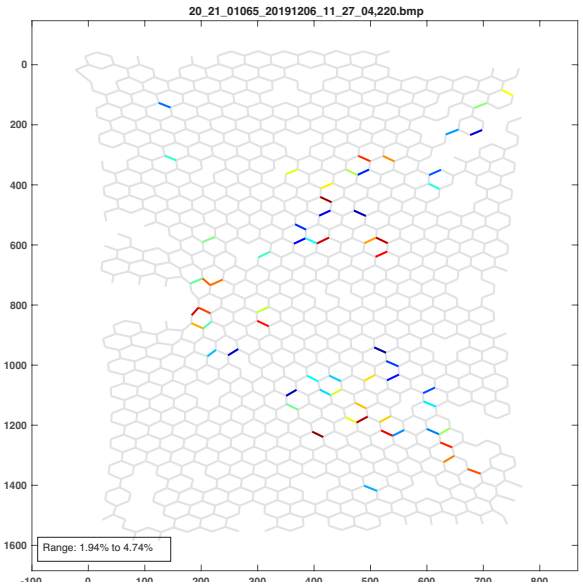
20_21_01065_20191206_11_27_04,220.bmp
Range: 1.94% to 4.74%

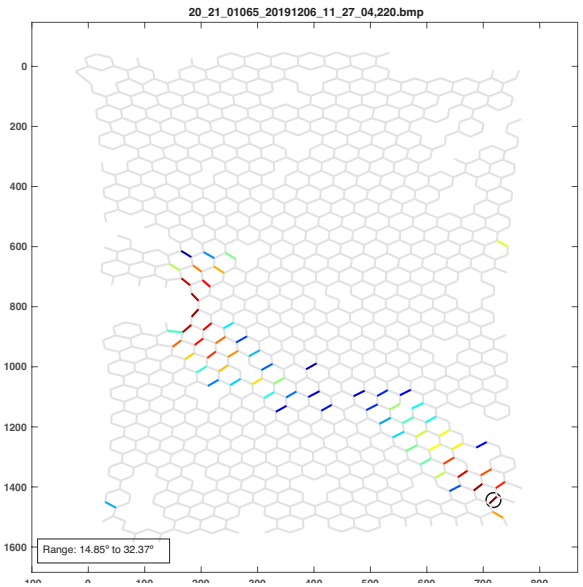
20_21_01065_20191206_11_27_04,220.bmp
Range: 14.85° to 32.37°

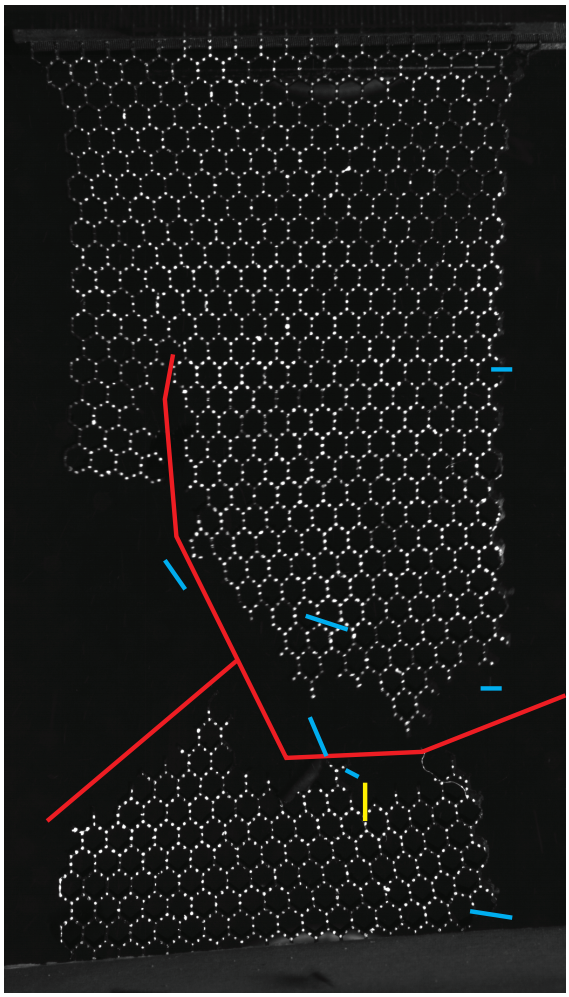

30_21

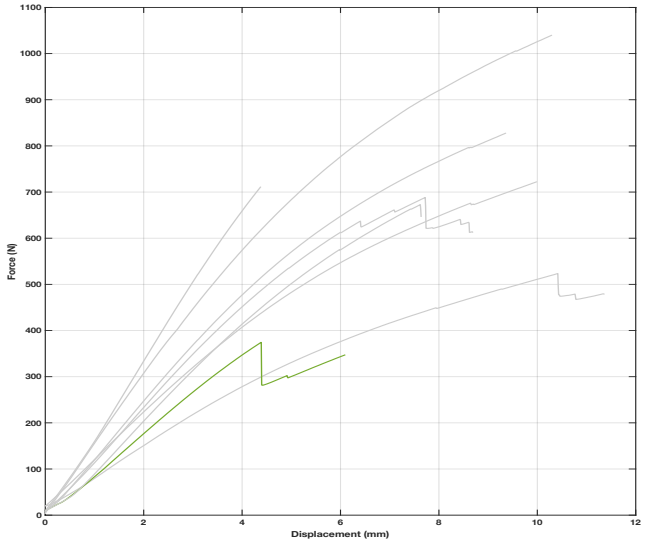
Force (N)
Displacement (mm)

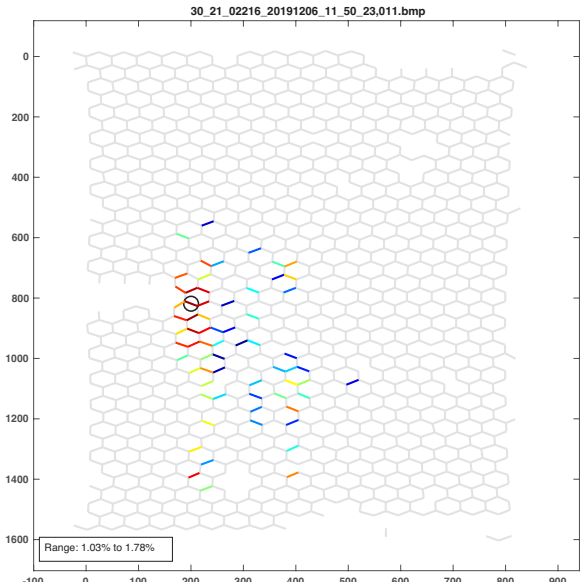
30_21_02216_20191206_11_50_23,011.bmp
Range: 1.03% to 1.78%

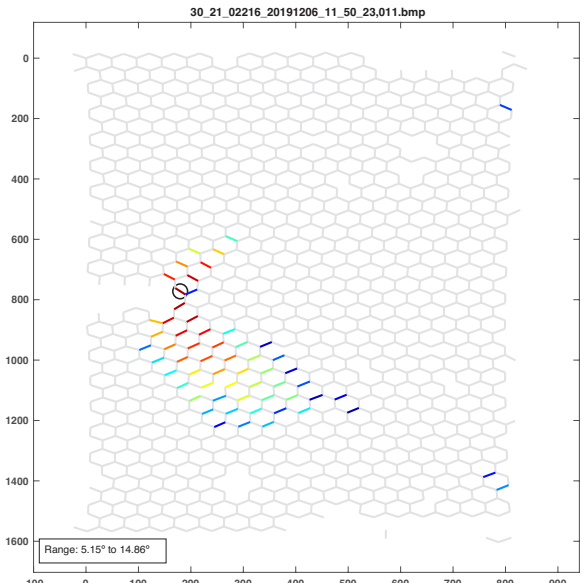
30_21_02216_20191206_11_50_23,011.bmp
Range: 5.15° to 14.86°

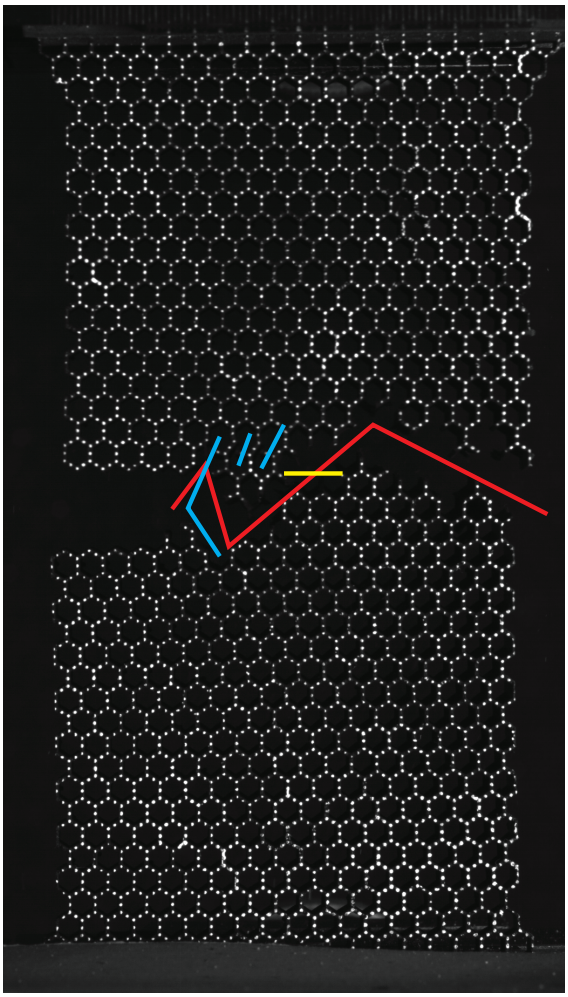

40_21

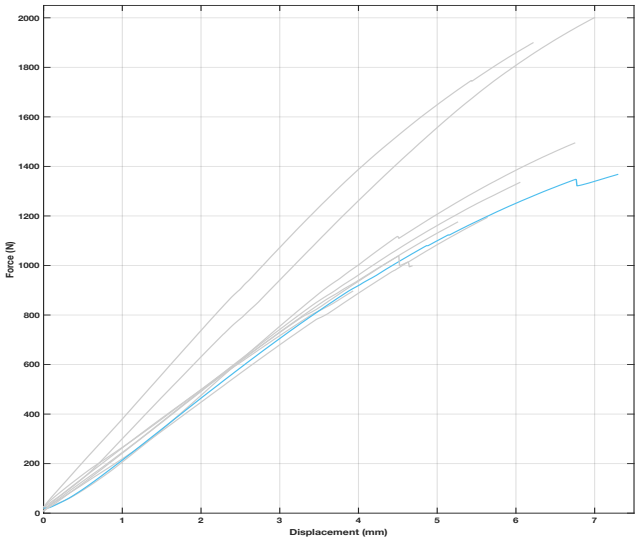
Force (N)
Displacement (mm)

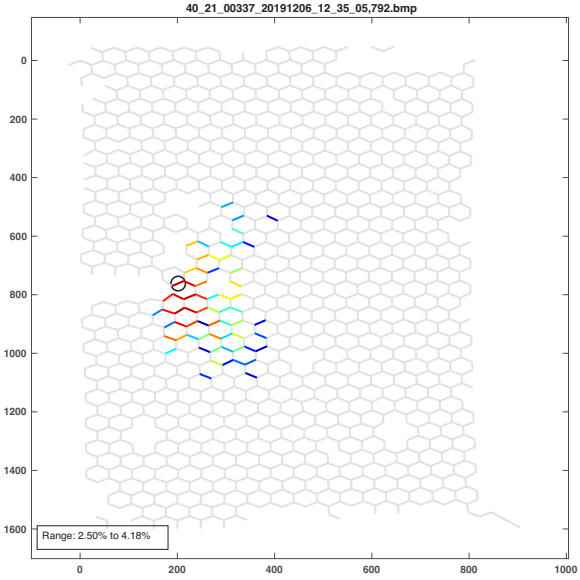
40_21_00337_20191206_12_35_05,792.bmp
Range: 2.50% to 4.18%

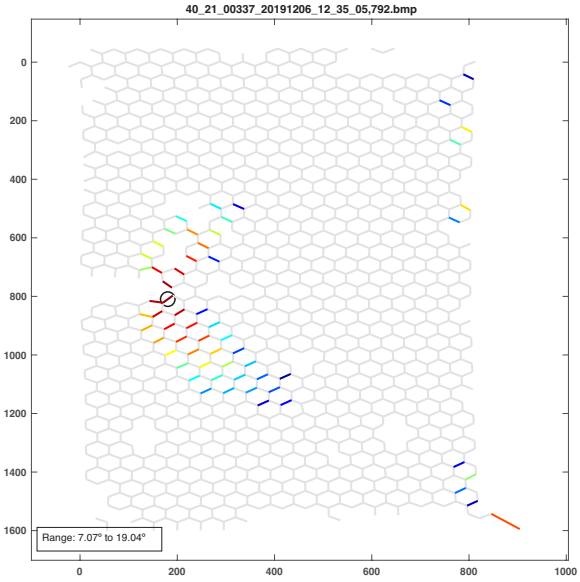
40_21_00337_20191206_12_35_05,792.bmp
Range: 7.07° to 19.04°

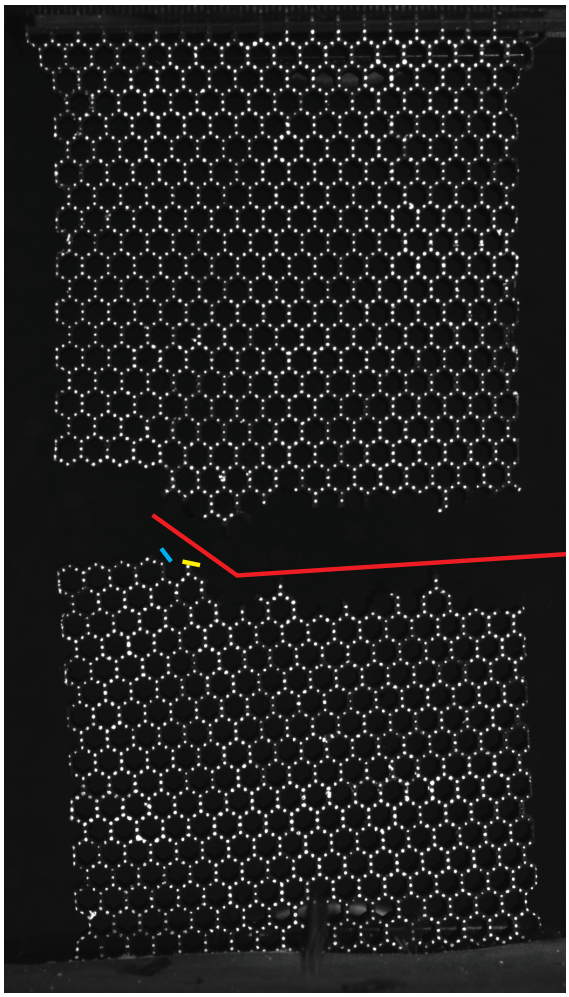

B_01

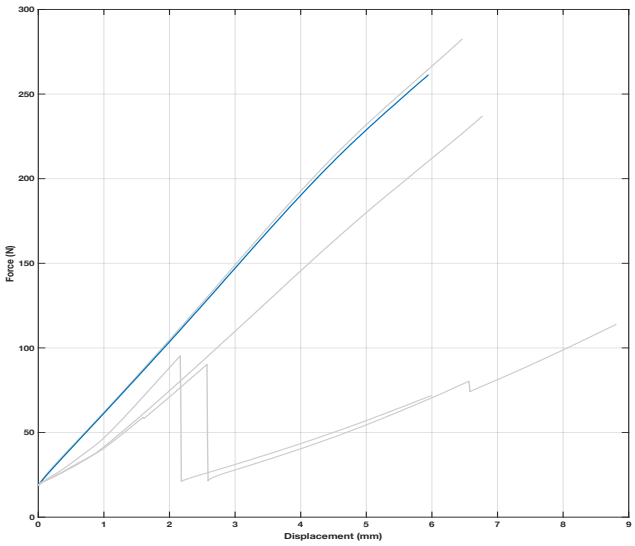
Force (N)
Displacement (mm)

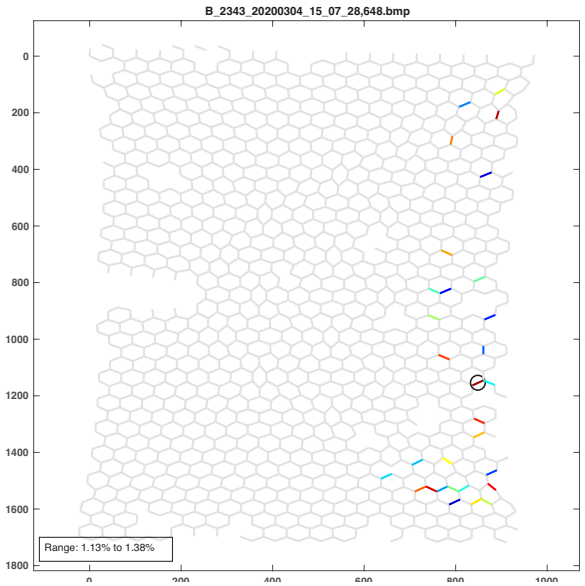
B_2343_20200304_15_07_28,648.bmp
Range: 1.13% to 1.38%

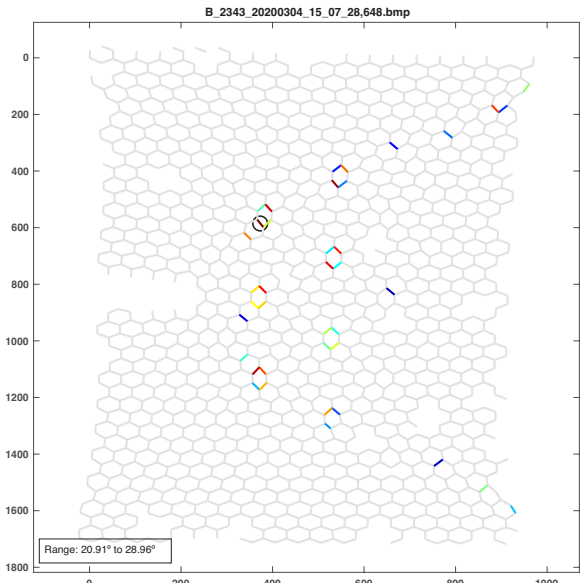
B_2343_20200304_15_07_28,648.bmp
Range: 20.91° to 28.96°

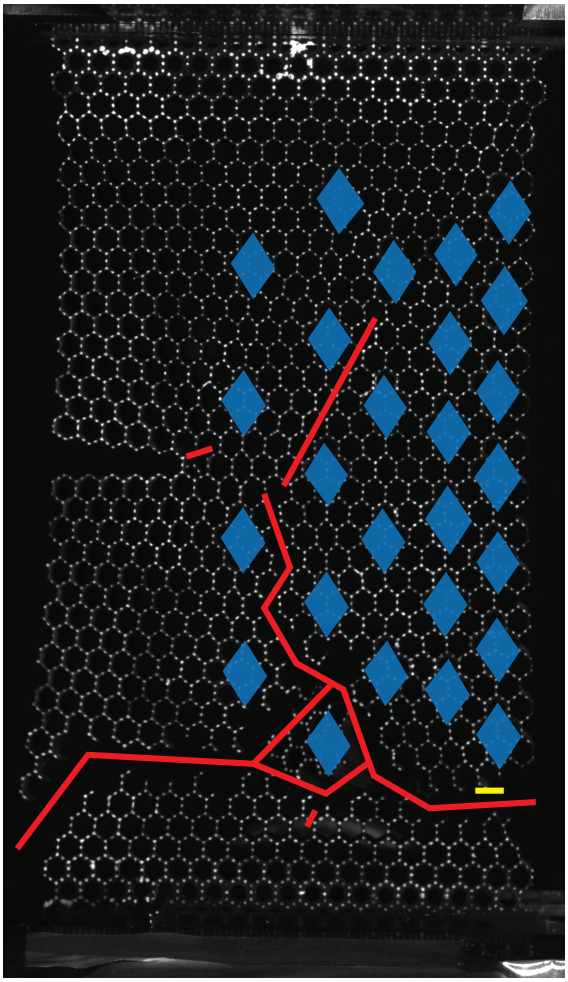

N_04

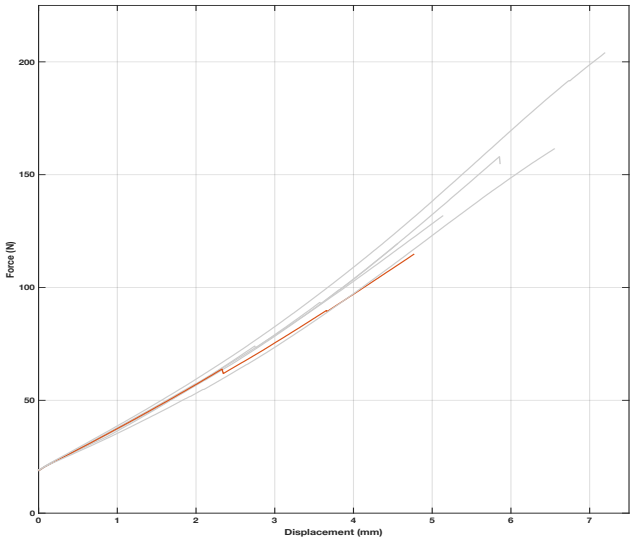
Force (N)
Displacement (mm)

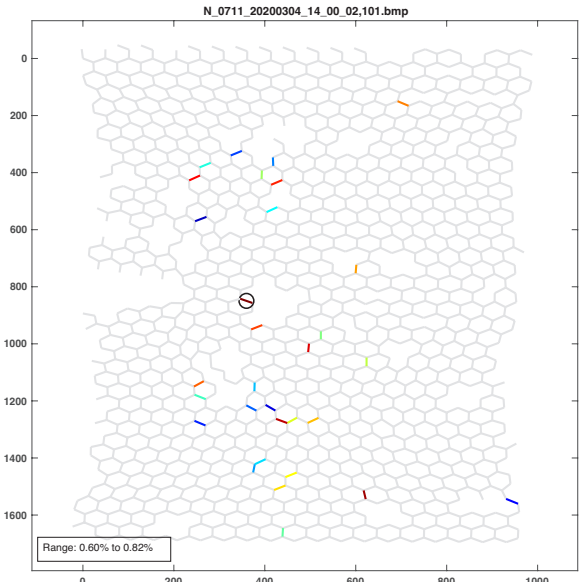
N_0711_20200304_14_00_02,101.bmp
Range: 0.60% to 0.82%

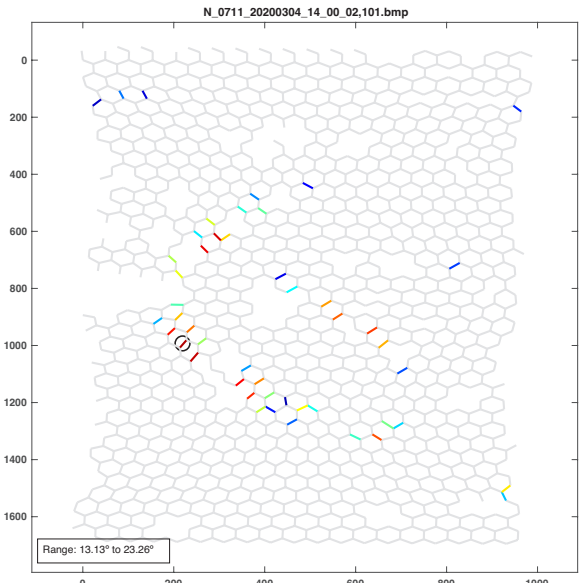
N_0711_20200304_14_00_02,101.bmp
Range: 13.13° to 23.26°

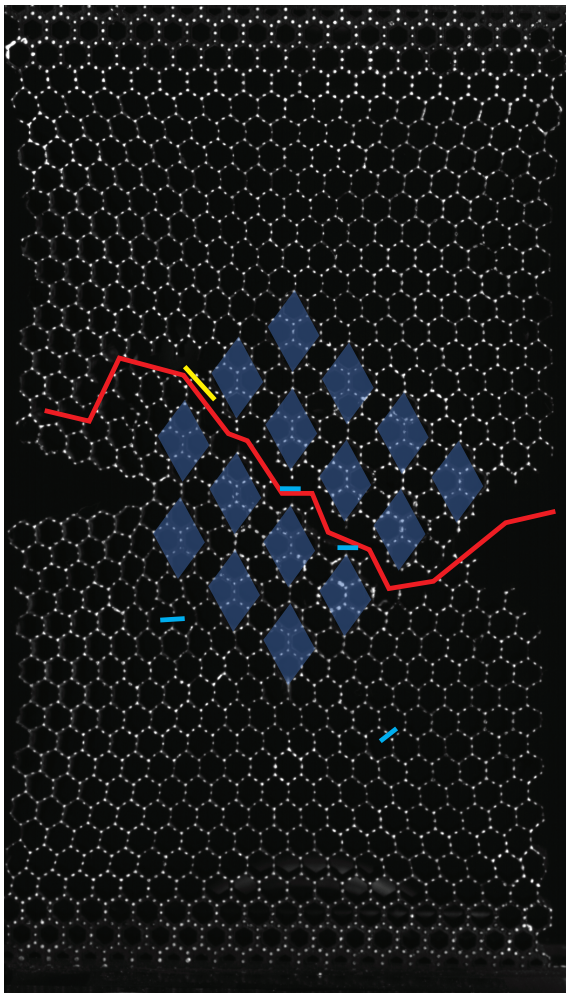

G_05

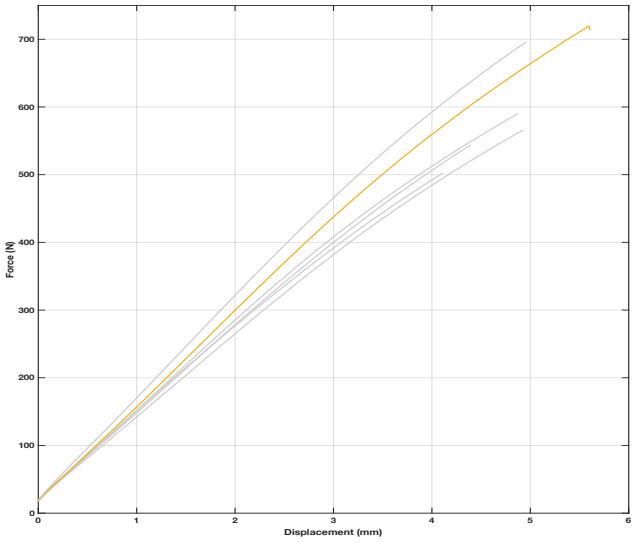
Force (N)
Displacement (mm)
0
100
200
300
400
500
600
700
0
1
2
3
4
5
6

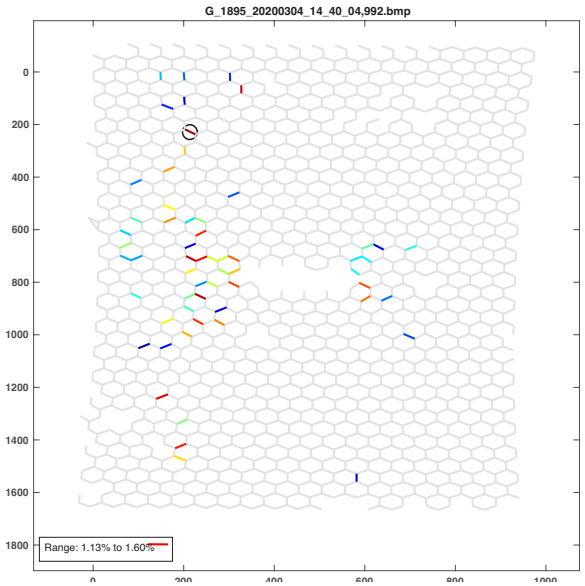
G_1895_20200304_14_40_04,992.bmp
Range: 1.13% to 1.60%

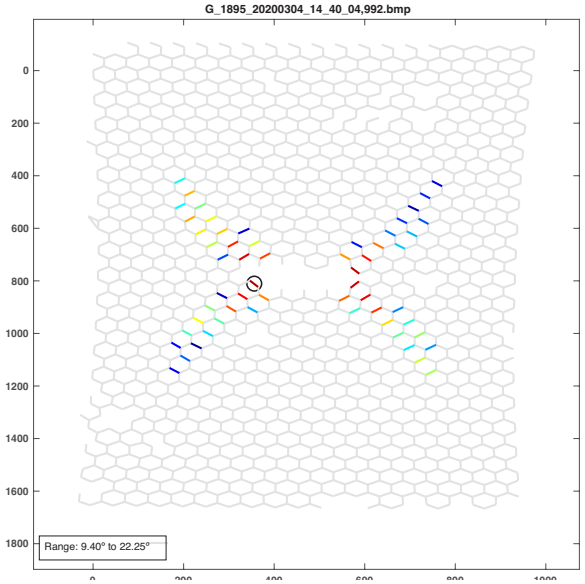
G_1895_20200304_14_40_04,992.bmp
Range: 9.40° to 22.25°

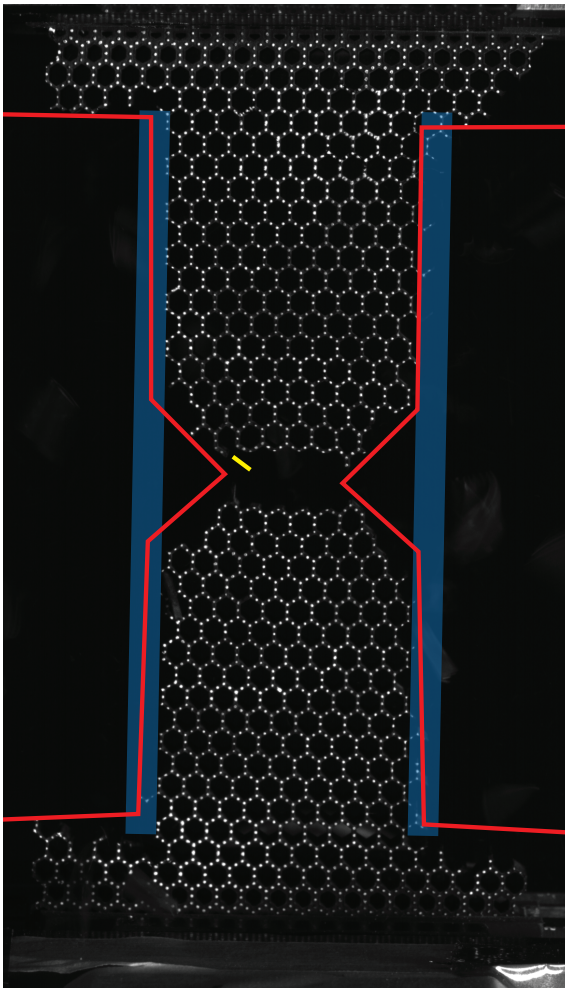

E_03

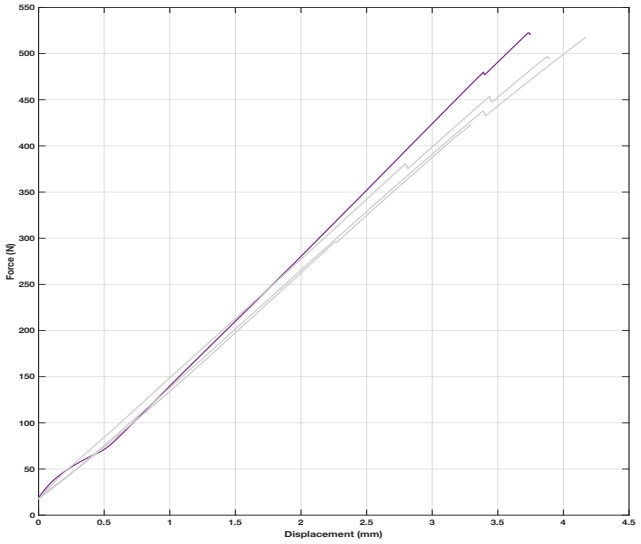
Force (N)
Displacement (mm)

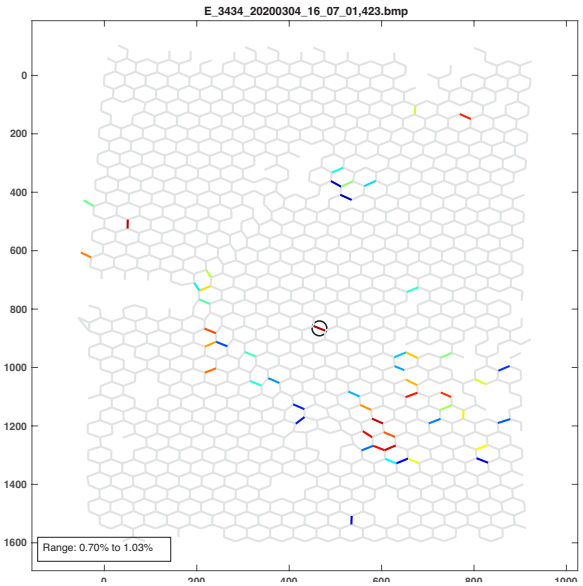
E_3434_20200304_16_07_01,423.bmp
Range: 0.70% to 1.03%

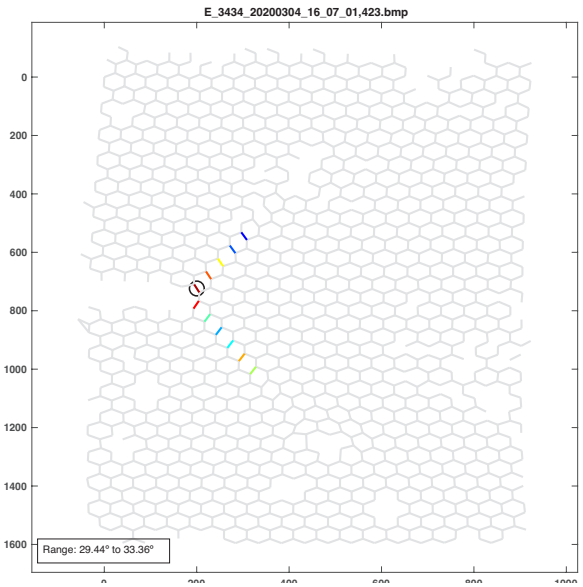
E_3434_20200304_16_07_01,423.bmp
Range: 29.44° to 33.36°